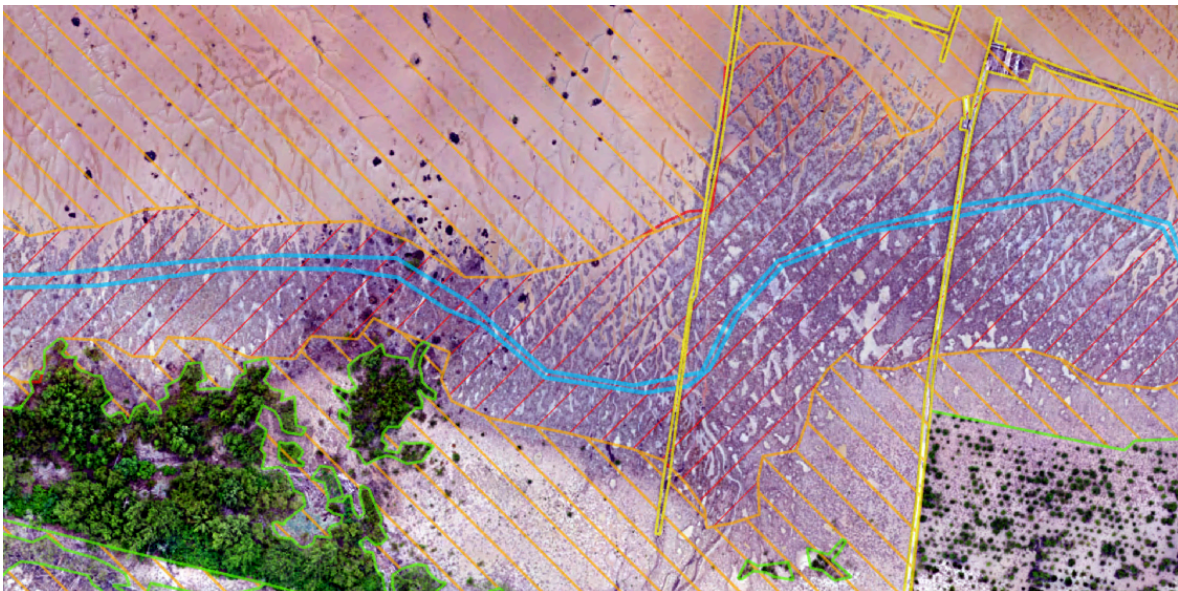

SPATIAL VARIATION AT THE SURINAME COAST:

Deriving alongshore and cross-shore patterns in tidal channel geometry, elevation and vegetation from UAV imagery



Tessa Deggeller (5655374)
Utrecht University

Supervised by:
Dr. Wiebe Nijland
Job de Vries



Utrecht University

February 2021

Abstract

Globally, 40% of the population lives in coastal areas, many often using satellite data. However, little efforts have been undertaken to study detailed observations of channel morphology on the Amazon coast, and its interplay with erosion and accretion is therefore not well understood.

Unmanned aerial vehicles (UAV's) combined with photogrammetric procedures have proven to be a valuable method for observing small-scale (changes in) coastal morphology, as it provides high resolution imagery and elevation data. However, research into the application of this technique in observing coastal elevation is scarce. This thesis focusses specifically on the application of UAV-photogrammetry in analysis of changes and spatial patterns in coastal erosion and accretion, and channel geometry. This research comprises a case study on coastal change and spatial variations in morphological features at Weg naar Zee, a coastal area in Paramaribo, Suriname, through the use of UAV imagery. The objectives were as follows. The potential of using UAV imagery for the assessment of coastal morphology is examined (1). Then, spatial patterns (2) and temporal changes (3) in channel geometry, vegetation cover and elevation were analysed.

Orthophotos and DEM's were created from the UAV imagery for two locations that were 2 km apart, and for one of these locations a second dataset was made for 8 months later in time. Morphological units were mapped manually based on the orthophoto and DEM. For each site, channels width, depth, W:D ratio, area and channel bed elevation and slope were derived from transects with the DEM elevation data. These geometries were compared for alongshore and cross-shore patterns and differences. Lastly, elevation differences between the 8-month period were derived from the DEM's.

Significant differences were visible despite the small spatial scale and short time period. The site closest to the river is bounded by dikes on the coastal side and a cross-shore levee. It showed signs of erosion, namely an immature parallel channel pattern, low elevations and a small range of elevations on the mudflat, lower width-to-depth ratios, less vegetation and dying vegetation, and an average high-water line that reached all the way to the dike. The site further west of the river is more stable, with growing mangrove vegetation and a large buffer zone between the mainland dike and the average high-water line. The channel network pattern was meandering dendritic. At this site, mangroves are planted to regenerate the vegetation, and permeable dams are constructed in the intertidal area as sediment trapping units. After the 8-month period, the elevation of the intertidal mudflat had increased with ± 0.5 meters.

This research has sketched a wide variety of spatial variations in morphology and coastal behaviour that can occur on a small scale in cross-shore and alongshore direction. As this local variation is critical in understanding how and where to implement erosion mitigation strategies, it is necessary to upscale this research with longer time-series and larger along shore coverage to determine which processes are at the base of this variation. Furthermore, UAV imagery has proven to be successful in determining both medium-scale and small-scale morphologies and elevations. It provides a diversity of datatypes, and it has the potential to facilitate direct erosion and accretion, and automated morphology classification.

Table of Contents

Abstract.....	1
List of figures.....	3
1. Introduction.....	4
Remote Sensing	5
Objectives and Research Questions.....	5
2. Previous work and regional setting.....	7
2.1 Climate in Suriname and the Amazon Coast	7
2.2 Coastal morphology	8
2.2.1 Mudbanks	8
2.2.2 Cheniers.....	10
2.2.3 River mouths.....	10
2.3 Intertidal area.....	12
2.4 Mangroves.....	15
2.5 Coastal change in Suriname	16
3. Materials and methods.....	17
3.1 Research area description	17
3.2 Data Collection	19
3.3 Data Processing	20
3.4 Orthophoto classification.....	21
3.5 Channel Geometry	21
3.6 Elevation differences	22
4. Results.....	23
4.1 Imagery and map output.....	23
4.1.1 Output quality.....	23
4.1.2 Differences in orthophotos and classified maps.....	26
4.1.3 Differences in DEMs	32
4.2 Channel Geometry	35
4.2.1 Channel elevation	35
4.2.2 Width, depth and area (along the channel and per latitude).....	37
4.2.3 Slope, elevation	38
4.3 Elevation differences in West-2019-2020	43
5. Discussion.....	45
5.1 Spatial differences	45
5.2 Temporal differences	47
5.3 Channel geometry.....	48
5.4 Potential of UAV research for coastal regions	49
6. Conclusion	50
References.....	51
Appendix A - Location of ground control points.....	54
Appendix B - ArcGIS model for transects	56
Appendix C - Orthophoto's.....	57
Appendix D - DEM's	60
Appendix E - Location of channels on DEM.....	63
Appendix F - Channel geometry West-2020.....	65

List of figures

Figure 1. Major ocean currents in the Atlantic	7
Figure 2. Wave climate at the Suriname coast	8
Figure 3. Turbidity along the Amazon delta	9
Figure 4. Mudbank migration and dynamics	10
Figure 5. Morphodynamics and sediment transfer at the Braamspunt chenier	11
Figure 6. Satellite image of the Surinam coast	11
Figure 7. Connection between profile shape of a tidal flat and the independent forcings	12
Figure 8. A classification for salt marsh creek networks	14
Figure 9. Width-to-depth ratio	14
Figure 10. Black mangrove	15
Figure 11. Map of the Suriname coast and coastal erosion and accretion	16
Figure 12. Location of the study sites	17
Figure 13. Shoreline changes between 2009 and 2015	18
Figure 14. A: Newly planted mangroves and two parallel lines of upright poles	18
Figure 15. Wooden jetties with examples of Ground Control Points	19
Figure 16. Examples of transects and the identified channel boundaries in RStudio.	22
Figure 17. Camera locations and image overlap	24
Figure 18. Camera processing data and error estimates	25
Figure 19. Typical channel network patterns	27
Figure 20. Orthophoto and classified map for East-2019	28
Figure 21. Orthophoto and classified map for West-2019	29
Figure 22. Orthophoto and classified map for West-2020	30
Figure 23. Close-ups of differences between West-2019 and West-2020	31
Figure 25. DEM for East-2019	33
Figure 25. DEM for West-2019	33
Figure 26. DEM for West-2020	34
Figure 27. Location of the channels	35
Figure 28. Channel bed elevation	36
Figure 29. Elevation of the channel-polyline	36
Figure 30. Channel elevation	37
Figure 31. Channel width	38
Figure 32. Channel depth	39
Figure 33. Channel width-to-depth ratio	40
Figure 34. Channel area	41
Figure 35. Channel bed slope	42
Figure 36. Relative change in sediment elevation between 2019 and 2020	43
Figure 37. Elevation change between West-2019 and West-2020	44

1. Introduction

Globally, around 40% of the population lives in coastal areas within 100 kilometres of the sea (United Nations, 2017) and most of the world's metropolises are located in the coastal zone. These zones are attractive to humans because of their rich resources and their logistical accessibility (Neumann et al., 2015). Coasts are very dynamic areas, and their stability can therefore not always be relied on. Coastlines can move landward or seaward due to erosion and deposition, depending on local hydrodynamics and sediment dynamics. These dynamics vary spatially and temporally and are subject to human influence.

Coastal erosion mainly takes place through sediment transport by currents, waves and tides. Large-scale currents transport sediment parallel to the coast through along-shore drift, caused by global ocean currents resulting from the Coriolis effect and thermohaline circulation. Waves impact sediment transport as well. As they begin to break when reaching shallow waters, they disturb the sediment below, bringing material into suspension in the water column. This process erodes the shoreline. When the breakers crash onto the shore, they send a surge of water up the beach. This upward surge, or swash, carries sediment up the beach, and continues until the motion is halted by friction. Gravity then draws the water and sediment back down the beach as backwash (Marshak, 2015). Depending on the seaward and landward sediment fluxes, waves cause erosion as well as deposition. Tides also work both ways: in ideal situations, tidal-current velocities vary sinusoidally over an ebb and flood period, with equal durations and speeds in opposite directions. In such cases, there is no net sediment transport. However, reality often deviates from the ideal, resulting in a time-velocity asymmetry that causes an inequality in amount of seaward and landward sediment transport (Dalrymple & Choi, 1978). Apart from these direct effects of tides on sediment transport, tides also facilitate intertidal ecosystems, indirectly altering the sediment balance. For example, vegetation protects the coast against erosion by reducing currents, whereas microphytobenthos and bacteria stabilize sediments through the formation of biofilms (Yallop et al., 1994).

The three driving forces discussed above can have opposite effects on net sediment transport. For example, this depends on sediment characteristics and hydrodynamics such as flow velocities. Coastal characteristics (e.g., topography, sediment composition, ecosystems) and the hydrodynamics resulting from currents, waves and tides, are interrelated through feedback effects. Coastal characteristics alter hydrodynamics, and are in turn also altered by hydrodynamics. One way in which this feedback plays a role is with the formation of tidal channels. Channels form as a result of erosion by converging tidal flows. They are a primary control on coastal environments (Hughes, 2011). As larger channels can carry more water, they have increased flow velocities and can thus enhance both landward and seaward sediment transport. The characteristics of this drainage network therefore provide important information on the potential development of the coast.

The dynamics that result in accretion and erosion are complex, and the balance is not a stable one: positive feedbacks can accelerate the rate of change for both accretion and erosion. Especially the feedback cycles enhancing erosion can be a threat to the environment. Too much pressure on the system disrupts the balance, and can move the shoreline hundreds of meters landward, taking up forests, agricultural lands, houses and infrastructure.

One of the regions where temporal and spatial variation of coastal behaviour is large, is the Guiana coast in South America. It is characterized by the supply of mud from the Amazon river: around 20% of the sediment flows west, along the Guianas coast. Part of this mud is transported in large mudbanks of a few 10s of km in length, which migrate westward with a speed of around 2 km/yr (Toorman et al., 2018). Along these coasts, mangrove forests colonize the shorelines, especially on intertidal areas and just above mean high water level. Mangrove forests can stabilize the sediment as they slow down the movement of tidal currents and waves, thus causing sediments to settle and build up beneath the mangrove roots. However, strong energetic environments, waves and currents can uproot and wash

away these trees (Toorman et al., 2018). Mudbanks and mangroves act as natural soft coastal defence structures and protect the coast against erosion.

Suriname is one of the countries on this coast and it is listed as one of the seven most endangered countries by sea level rise worldwide (Wetlands International, 2016). The erosion rate at the Suriname coast has increased in recent years – for some areas along the coast, analysis of satellite images has shown a coastal retreat of hundreds of meters in the last 30 years (Cete. et al., 2018) – and sea level rise is expected to increase due to climate change (IPCC, 2014).

As many factors play a role and a retreating shoreline has a lot of consequences for humans and nature, it is important to monitor, understand, and, if possible, improve these dynamics as well as our influence on it. The interactions between mud, hydrodynamic forcing and mangroves have continually been a topic of research (Anthony et al., 2010). To be able to understand causes of erosion and its local variation on the muddy Guiana coast, it is important to map patterns in beach topography and vegetation. However, little efforts have been undertaken to study detailed observations of channel morphology on the Guiana coast, and its interplay with erosion and accretion is therefore not well understood.

Remote Sensing

Remote sensing is a much-used technique in coastal research. It improved our ability to map and monitor the dynamic nature of coastal areas. Remote sensing is fast and efficient when compared to conventional field work, which is costly, time-consuming, and sometimes impossible due to the poor accessibility of coastal (mangrove) areas (Cao et al., 2018). The type of remote sensing platform (ground-bases, airborne or satellite) and sensor depend on the scale and the goal of the research (Navarro et al., 2020). The high temporal frequency achieved through repeated coverage of satellite imagery has led to a consistent, global, long-term database, which can be used to detect coastal changes (Doughty & Cavanaugh, 2019). For example, satellite remote sensing has been used to detect changes in the location of the shoreline (Alesheikh et al., 2007; Besset et al., 2019; de Vries et al., 2021) and coastal vegetation cover (Adam et al., 2010; De Jong et al., 2021). However, most satellite and airborne sensors have limited spatial resolution and are thus not suitable for detailed, small-scale analyses. A commonly used alternative providing higher resolutions is airborne LiDAR (light detection and ranging), which can provide detailed information on topography (Proisy et al., 2009). It can measure surface elevation with a high accuracy, even under dense vegetation canopies (Yin & Wang, 2019), and it is therefore very suitable to detect spatial variability of microtopography in the intertidal zone (Zhu et al., 2019). Yet the disadvantage of LiDAR is that it is expensive, not widely available, and data management and processing is often difficult (Navarro et al., 2020).

Unmanned aerial vehicles (UAVs) combined with photogrammetric procedures have the ability to increase spatial resolution compared to satellite data, while still covering large area. They provide a more cost-effective method than other airborne systems such as LiDAR, while they still have a high accuracy and resolution for imagery and elevations (Navarro et al., 2020). Furthermore, it facilitates a flexible timing of data collection. This is especially important in coastal areas, as the (in)visibility of intertidal surfaces depends on the status of the tidal cycle.

Objectives and Research Questions

UAV imagery has proven to be a valuable method for observing small-scale (changes in) coastal morphology. However, research into the application of this technique in observing coastal elevation is scarce. Hence, this thesis focusses specifically on the application of UAV-photogrammetry in analysis of changes and spatial patterns in coastal erosion and accretion, and channel geometry.

This thesis comprises a case study on coastal change and spatial variations in morphological features at two sites at Weg naar Zee, a coastal area in Paramaribo, Suriname, through the use of UAV imagery. The objective of this master thesis is threefold. The potential of using UAV imagery for the assessment of coastal morphology is examined (1). Then, spatial patterns (2) and temporal changes (3) in channel

geometry, vegetation cover and elevation are analysed. The following research questions and corresponding sub-questions are formulated:

1. What is the value of UAV imagery in coastal research?
 - What morphological units can be detected from UAV imagery?
 - Can channel geometry be derived from UAV based DEM's?
 - Is UAV suitable for monitoring coastal elevation?
2. What are spatial patterns in coastal morphology?
 - How does tidal channel geometry differ with alongshore and cross-shore location?
 - How does vegetation cover differ with alongshore and cross-shore location?
 - What are spatial patterns in mudflat elevation?
3. What are temporal patterns in coastal morphology?
 - How does tidal channel geometry change within 8 months time?
 - How does vegetation cover change within 8 months time?
 - How does mudflat elevation evolve over 8 months time?

This thesis is structured as follows. Chapter 2 describes the regional setting and explains how coastal processes interact. Chapter 3 describes the study site, the dataset and the data analysis. Chapter 4 lists the results of the imagery analysis and its accuracy. Chapter 5 provides a discussion of the results, including both the observed patterns in the data, and possibilities and challenges in using UAV imagery for coastal observation. Conclusions, including answers to the research questions, can be found in Chapter 6.

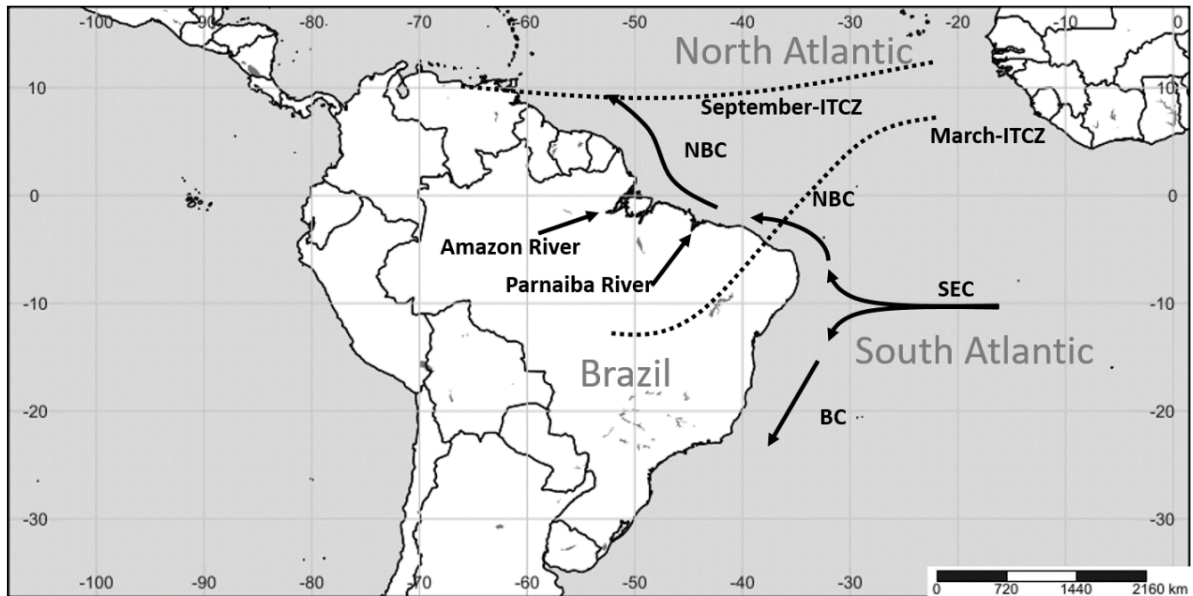


Figure 1. Schematic map showing the major ocean currents in the Atlantic. The Southern Equatorial Current (SEC) flows west, splitting into the Brazilian Current (BC) and the North Brazilian Current (NBC) (Roberts, 2017).

2. Previous work and regional setting

In the coastal system of the Guianas, hydrodynamics, mud banks, cheniers and mangroves all interact with each other. They have a great impact on the evolution of the coast, and thus on erosion/accretion and on channel geometry. Migrating mud banks cause periods of coastal protection and thereby accretion, alternated with interbank phases with increased erosion due to wave action. Cheniers are sand bodies in front of the coast which have a similar effect on the coastline dynamics. Mangroves also have a wave-breaking effect, enhancing sedimentation. In this chapter, these systems are briefly discussed, and their interrelation is explained. To begin with, the (hydro)climate is described in section 1. Then, the coastal morphology (a.o. mudbanks and cheniers) is explained (section 2) as well as mangrove vegetation (section 3). Section 4 elaborates on processes and morphology in the intertidal area, and lastly, section 5 gives an overview of recent coastline changes.

2.1 Climate in Suriname and the Amazon Coast

The Amazon coast is the 1500 km long coast of South America, stretching from the mouth of the Amazon river in Brazil, going west along French Guiana, Surinam, Guyana, to the mouth of the Orinoco river in Venezuela. In Surinam, the climate is tropical with daytime temperatures between 27°C and 34°C and night-time temperatures between 21°C and 24°C year-round (klimaatinfo.nl, n.d.). Precipitation varies from 2 to 3 meters per year and falls predominantly from December to July (Anthony et al., 2014). The seasonal alteration is attributed to the change in location of the intertropical convergence zone (ITCZ) from north to south (Chevalier et al., 2004).

The main oceanic forcing mechanism is the South Equatorial current, which flows west from the Southern Atlantic Ocean to Brazil and then splits into the North Brazil Current (NBC) or Guiana current, flowing along the Guiana coast, and the Brazil Current going southward from Brazil (Figure 1). Because of the NBC, the Guiana coast is continuously under influence of a north-westward current, flowing over the outer shelf (Chevalier et al., 2004).

Suriname has semi-diurnal tide, with two daily low and high tides of different amplitudes per lunar day (Bourret et al., 2008). The spring tidal range at the Suriname coast is low-mesotidal. Maximum spring tidal range is 3 m and the mean tidal range is 1.8 m (Deppe, 1999). The coastline is wave dominated

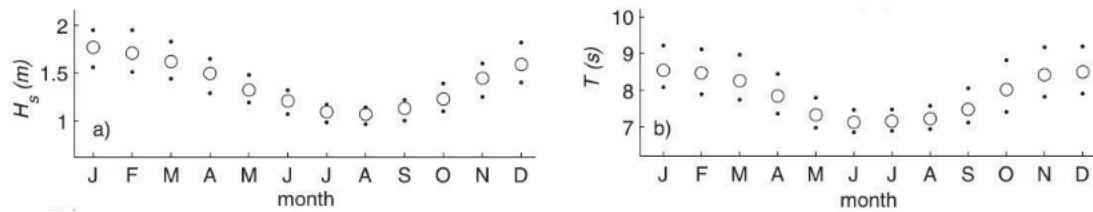


Figure 2. Wave climate at the Suriname coast from a 44-year record of ERA-40 (European ReAnalysis). Left shows significant wave height H_s , and right shows significant wave period T_s . Dots represent the first and third inter-quartiles, circles are the median values (Anthony, 2016)

and it is marked by a strong seasonal pattern in wave energy (Anthony et al., 2019). The coastline is influenced by North-Eastern trade winds, which are strongest between January and May. The waves from the North and Central Atlantic Ocean are generated by these trade winds, and therefore have a directional range of east to northeast (Gratiot et al., 2007). Waves typically have offshore heights of 1-2 m, and periods of 6-10 s (Figure 2). The longer waves, with periods above 8 s, are mostly associated with periods of large swell waves, created in autumn and winter by North Atlantic storms, and in summer and autumn by Central Atlantic cyclones. These waves come from a north to north-northwest direction (Anthony et al., 2019). The wave height varies on time scales ranging from multiple years, depending on El Niño Southern Oscillations (ENSO), to multiple decades, caused by changes in large-scale atmosphere-ocean interactions in the North Atlantic (Walcker et al., 2015).

2.2 Coastal morphology

The Guiana Coast is characterized by the large amount of mud traversing this coast from east to west. This mud is supplied by the Amazon river, which has a water discharge of $209000 \text{ m}^3/\text{s}$ (equalling $6591 \text{ km}^3/\text{yr}$) (Seyler et al., 1998) and a yearly suspended sediment discharge of $754 \times 10^6 \text{ tons} \pm 9\%$ (Anthony et al., 2010). Of this sediment 20% is transported west due to longshore currents, partly as suspended matter ($150 \times 10^6 \text{ tons}/\text{yr}$), but and partly the form of mud banks ($100 \times 10^6 \text{ tons}/\text{yr}$) (Toorman et al., 2018). Figure 3 shows the turbidity along the Guiana coastline of South America, caused by the suspended sediment.

Of the sediment transported by the river and transported along the coast, 90% is silt and clay particles (Wright & Nittrouer, 1995). Because clay particles are cohesive, they aggregate and form flocs. When they sink and settle on the bottom, they form a soil “skeleton” in which the flocs leave open voids: these pores are filled with water (Toorman et al., 2018). Fresh mud deposits have large pores, so can be compared to a card house structure: the volume of solids is low while the volume of water is high. When new mud deposits on top, the pressure of the weight from above increases and the network deforms, causing the card house structure to slowly collapse. The mud has a low permeability, so the compacting mud contains little oxygen below 5-10 cm depths, which is the reason a.o. mangrove trees have shallow root systems (Toorman et al., 2018).

2.2.1 Mudbanks

Near the mouth of the Amazon river, around 15-20% of the muddy discharge forms highly turbid suspensions ($>1\text{g}/\text{L}$). This causes mud banks to form that traverse from east to west, causing a multi-year cycle of erosion and accretion. There can be around 15 mudbanks simultaneously migrating along the Amazon coast, each with a length of 10-60 km. They migrate westward with speeds of $2\text{km}/\text{yr}$, and they can contain the multiple times the equivalent mass of the yearly sediment discharge of the Amazon river (Anthony et al., 2010, 2019; Toorman et al., 2018). They are traversing over a mud wedges that are deposited by earlier mud banks, at water depths of $<5 \text{ m}$ (Mead A. Allison et al., 2000) or $<5 \text{ to } 20 \text{ m}$ (Anthony et al., 2010). The cycle of mudbanks is generated by sediment transport through longshore currents and wave hydrodynamics. Westward migration happens by erosion on the east side (trailing edge) of the bank, and deposition of fluid mud on the leading side (Figure 4).

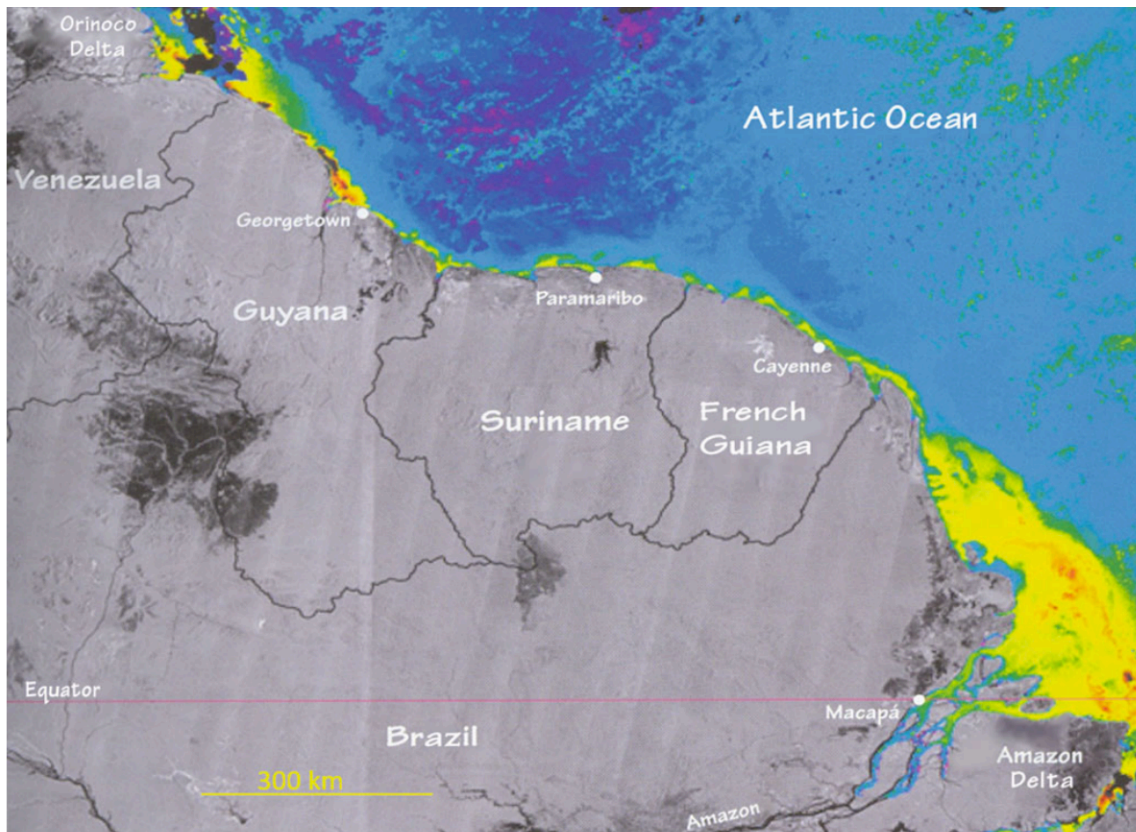


Figure 3. Turbidity along the Amazon delta and the north-eastern coastline of South America derived from NOAA satellite images (Toorman et al., 2018).

There are different theories about mudbank morphology and migration. In the classical model, the mudbank is attached to the shore and migrates by erosion on the trailing edge and deposition at the leading edge. According to (M. A. Allison & Lee, 2004) Allison and Lee (2004), mud banks are disconnected from the coast. During high tide, fluid muds flow shoreward over the mud bank, and fill the upper intertidal area between the bank and the coast (Toorman et al., 2018). This fluid mud originates from the eroding trailing edge as well as from the transported suspended sediment load. When the silt particle concentration exceeds the point of hindered settling, the particles will not sink from the water column anymore, but instead it forms very soft stable fluid mud. Due to friction between sediment particles (visco-plastic deformation), fluid mud absorbs the wave energy, strongly attenuating the passing waves. This enhances sediment deposition (Toorman et al., 2018). After time, the fluid mud becomes more compact and consolidates. This is when mangroves get the chance to grow. Their roots, in turn, give rigidity to the soil and increase compaction by extracting water, and increase the surface roughness, damping energy from waves and currents. Due to ongoing consolidation, the mud at the “oldest” area at the east side of the bank will mature into young clay, which is more susceptible to erosion (Toorman et al., 2018). On the east side of the bank, waves are not attenuated anymore and sediment is therefore washed away. Mangrove trees are uprooted and will pile up, locally slowing down the erosion. However, the erosion still pursues and the mudbank migrates further westward. There will then be an interbank phase, in which the coast will be unprotected and therefore vulnerable for erosion. However, as there are multiple mudbanks along this shore, there will later come a new mudbank at that location (Toorman et al., 2018). This cycle takes around 30-35 years at any location along the Guiana coast (Augustinus, 2004; De Jong et al., 2021).

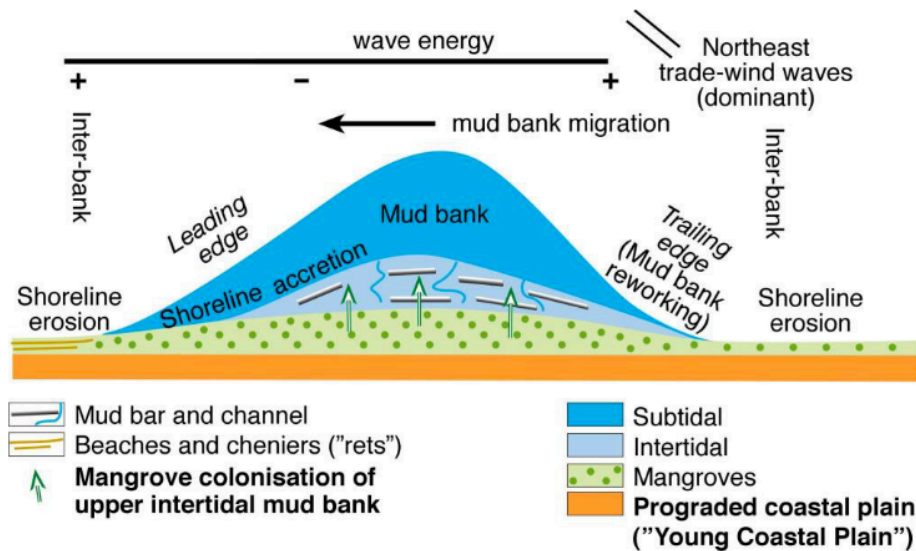


Figure 4. Mudbank migration and dynamics (Anthony, 2016).

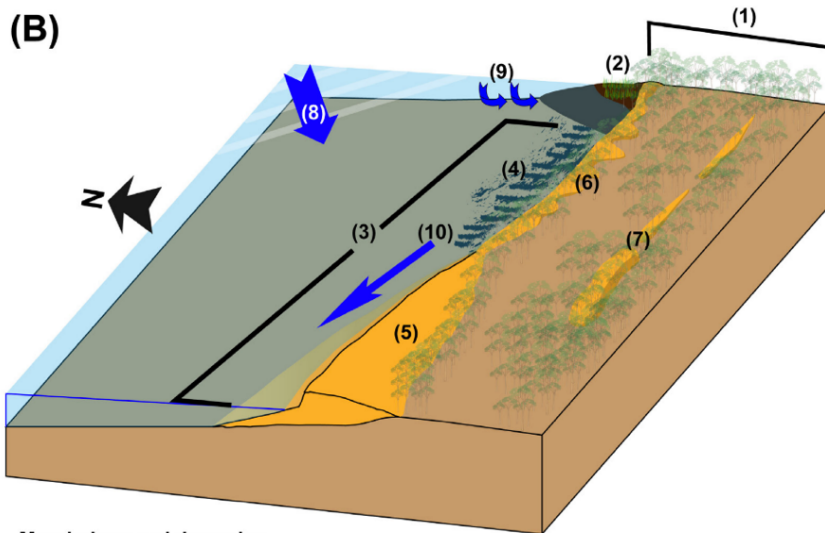
2.2.2 Cheniers

A chenier is a body of coarse grained sediment, deposited on top of a muddy substrate (Anthony et al., 2019). As more than 80% of the coastal deposits in Suriname is muddy, the availability of sand is scarce. Chenier formation depends on a specific balance between sediment availability and wave action which reworks the sand, and thus cheniers are not very common. They develop solely under circumstances where cohesive sediments are available in large volumes, with enough sand and shelly deposits or gravel that can be reworked by waves and segregated from the mud. This therefore happens mainly in inter-bank areas, where there is relatively high wave energy (Figure 5). The sand making up these cheniers is mostly supplied by the small rivers between the Amazon and the Orinoco rivers. Furthermore, marine carbonate debris from skeletal remains of organisms as well as older cheniers can also be reworked onshore by the waves, forming new cheniers.

The formation of these sand bodies helps dissipating the high energy waves in the interbank phases. It therefore acts as a natural coastal defence structure. However, cheniers are actively mined in the Guianas, which can enhance coastal erosion. For example, Anthony et al. (2019) found that the chenier at Braamspunt Beach (Figure 6) was strongly modified by commercial sand mining as well as natural erosion. They hypothesize that large-scale sand removal at Braamspunt could lead to damaging feedback effects, causing the eastern cape of the Suriname river to erode by several kilometres during inter-bank phases (Anthony et al., 2019).

2.2.3 River mouths

Along the Guiana coast, smaller river mouths tend to have a westward deflection on the coast, due to mud bank migration (Anthony, 2016). Commonly, a mud cape is formed on the east side of the river mouths, which is colonized by mangroves. These mud capes, together with their associated sandy cheniers, provide shelter to neighbouring coastal areas on their west-side, from ocean waves coming from the north-east (Anthony, 2016). For example, this is the case for the two rivers in Suriname shown in Figure 6. Both the Coppename river and the Suriname river deflect westward and have a sandy east cape. However, the rivers themselves have opposed effects: areas with increased erosion are associated with close proximity to the river mouths, suggesting that the fluvial jet outflow may prevent durable attachment of mud to the shore (Anthony, 2016).



Morphology and dynamics

- | | |
|--|---|
| (1) Muddy prograding Guianas coastal plain with old mangroves and cheniers | (4) Eroding muddy foreshore |
| (2) Mud-bank leading edge with young mangroves | (5) Chenier type 1 |
| (3) Inter-bank trailing edge | (6) Chenier type 2 |
| | (7) Inland cheniers |
| | (8) Deepwater wave approach (mainly NE) |
| | (9) Refracted waves |
| | (10) Longshore transport |

Figure 5. A conceptual model of the morphodynamics and sediment transfer at the Braamspunt chenier. (Anthony et al., 2019)

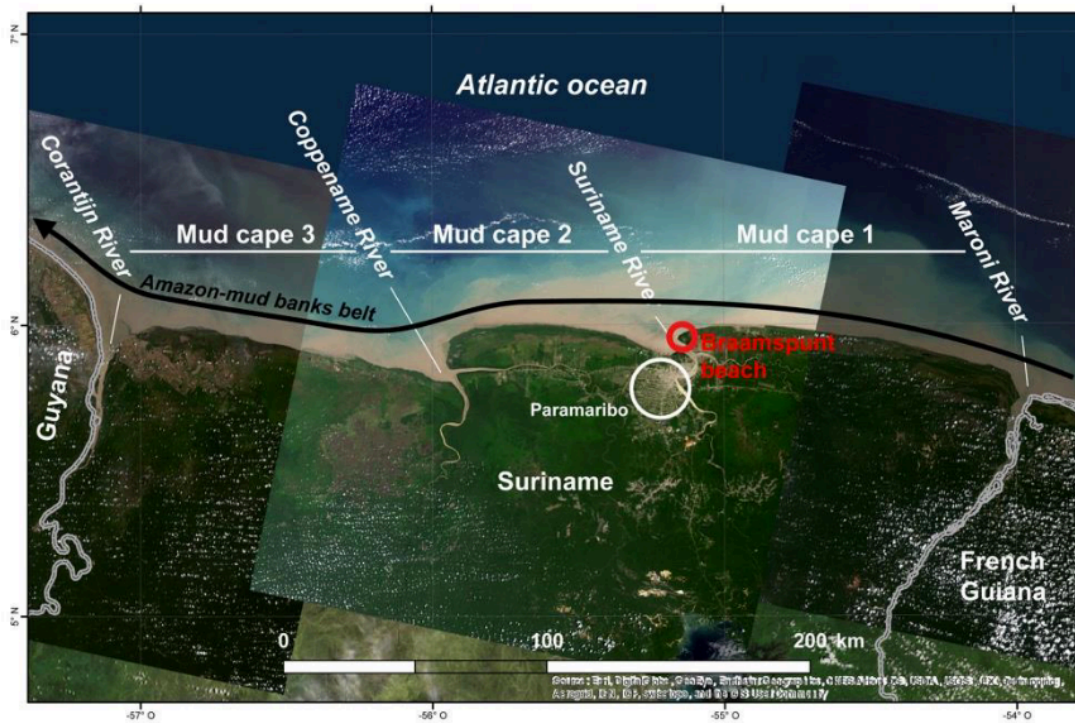


Figure 6. Satellite image of the Surinam coast, including the mud capes (orange hue) between the four main rivers (Anthony, 2016)

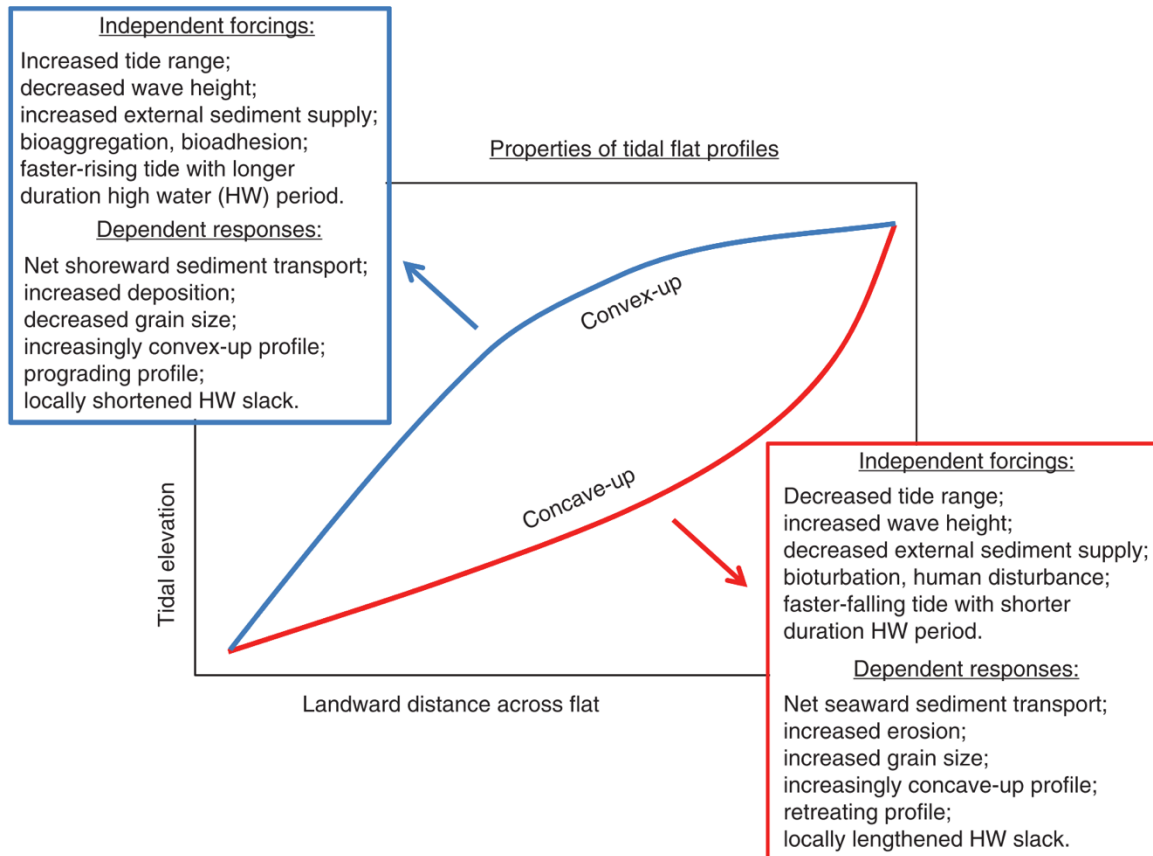


Figure 7. Conceptual diagram explaining the connection between profile shape of a tidal flat and the independent forcings, resulting in a concave-up or convex-up profile (Friedrichs, 2012).

2.3 Intertidal area

The intertidal area at a coast has an elevation that is between the level of lowest and highest astronomical tide, and is therefore periodically inundated by the sea. The size of the intertidal area thus depends on the slope of the shoreface, and on the local tidal amplitude. Characteristics like bed slope, profile shape and grain size are a direct function of sediment supply and wave and tidal forcing. In turn, the wave- and tide-induced dynamics across tidal flats are systematically a function of the tidal flat morphology itself. However, as waves, tides, and sediment supply effects all occur together, it can be difficult to separate these influences on morphology (Friedrichs, 2012).

Coasts are under influence of tides, waves, and sometimes rivers, and these individual forces can be more or less dominant compared to the others. The relative dominance of these processes defines to a large extent the morphological evolution of coast. Dominance by waves commonly is associated with net erosion, a larger average grain size, and seaward sediment transport. These coasts usually have a concave-up profile (Figure 7). Instead, dominance by tides results in net deposition, a smaller grain size, and landward sediment transport, and thus a prograding coast. Tide-dominant coasts are often convex-up. The Suriname coast is wave dominated (Anthony et al., 2019), yet due to the exceptionally large supply of mud from the Amazon river, grain sizes in intertidal areas are locally very fine.

Regions which are subject to regular inundation by tides self-organize into shallow zones which are repetitively flooded, and channels which drain these areas during ebb (Hughes, 2011). On intertidal areas, three major morphological components can therefore be distinguished, namely: vegetated platforms (marshes or mangroves), unvegetated tidal flats, and the channels propagating the tidal wave and connecting the other two zones. channels are formed through which the tidal wave propagates. These channels are defined by bidirectional flow. The nature of the network of channels impacts the local hydrodynamic conditions such as tidal flow velocity, and therefore also the period and depth of

inundation (Hughes, 2011). Ultimately, the channel characteristics and hydrodynamic conditions determine the long-term evolution of the region.

Tidal channel networks can be classified based on their planform. Multiple classifications have been developed (Eisma, 1998; Hibma et al., 2004; Van Veen et al., 2005). Pye and French (1993, via Hughes, 2011) defined a classification model for channels on marsh systems, differentiating on the level of channel complexity, and the occurrence of either single channels or developed networks (Hughes, 2011). Figure 8 shows the types of salt marsh creek networks in this classification, including linear, dendritic and meandering channel planforms. An individual channel can be anything from completely straight to meandering. A channel can be quantified on this scale using the sinuosity ratio, which is the length along the channel compared to the downstream distance in a straight line. A channel is considered meandering if it is above 1.5. Generally, larger channels have a lower sinuosity, as do easily eroded, non-cohesive and unvegetated sediments (Hughes, 2011).

Dendritic networks are most often observed on tidal flats. The channels in a dendritic network are described by their order. First-order channels are emerging on the tidal flat, where they are fed by sheet flow. Two or more first order channels join to form a larger second-order channel, and this continues until the highest order that is present in the system is reached (Hughes, 2011). According to Hughes et al. (2011), third-or higher order channels are rare in tidal areas. Systems with parallel channels rather than dendritic networks are uncommon. They are formed mostly in areas with a large tidal range and erodible sediment. Parallel channels are a poorly developed, or immature, drainage pattern; they occur in regions that are regularly impacted by storms which “reset” the channel morphology (Hughes, 2011). This way, the channels do not get enough time to develop more complex planforms.

Channel geometry is a result of – amongst others – tidal flows and sediment characteristics. Channel width is decreasing towards the head of a channel (Hughes, 2011). In Fagherazzi & Furbish (2001), it is explained that the width and depth of a channel are related to the hydraulic geometry and bankfull discharge. They state that:

$$w \propto Q^b$$

$$d \propto Q^f$$

In which Q is the bankfull discharge, w is the channel width and b is the depth. b and f are hydraulic geometry exponents, which are found to be around 0.77 and 0.33 respectively. This shows that the channel width varies more rapidly along the channel than the depth, as an increasing discharge in downstream direction has a larger effect on the width than on the depth of the channel (Fagherazzi & Furbish, 2001). Because of this difference in adjustment, the width-to-depth ratio, defined as:

$$\beta = \frac{w}{d},$$

will therefore increase in seaward direction.

Marani et al. (2002) compared tidal channel in different systems, based on their width-to-depth ratio, and found that largely two populations can be identified: salt marsh creeks usually have smaller ratios ($5 < \beta < 8$) than tidal flat channels ($8 < \beta < 50$) (Figure 9, Hughes, 2011). In tidal flat systems, sediments are usually coarser and less cohesive. This makes them more easily eroded, causing wider, shallower channels. Furthermore, vegetation will slow down the flow once it overtops the channel bank, which leads to increased deposition near the channel edges, locally enhancing accretion. This leads to larger channel depths (Hughes, 2011).

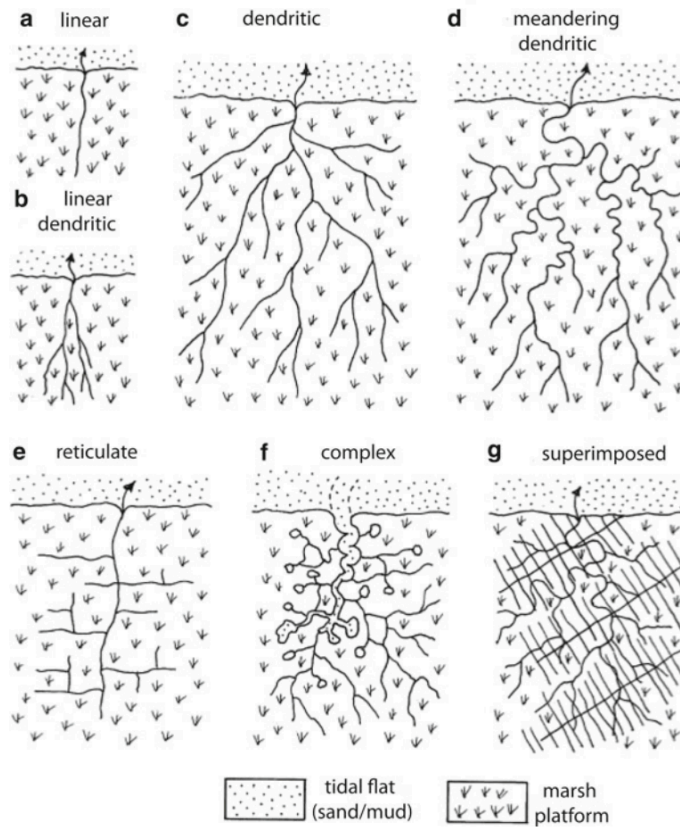


Figure 8. A classification for salt marsh creek networks (by Pye and French, 1993, via Hughes, 2011)

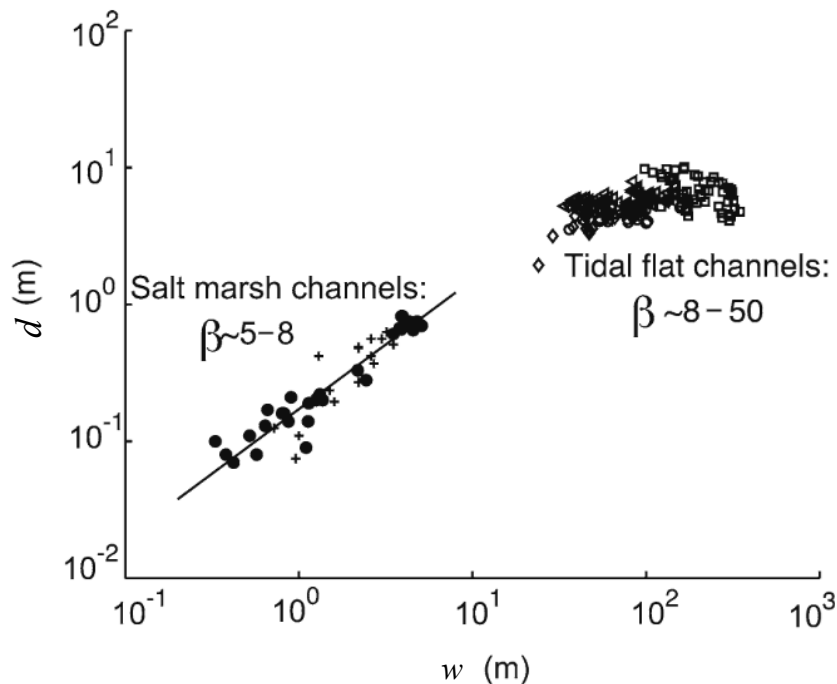


Figure 9. Width-to-depth ratio defined as $\beta=w/d$, measured from tidal channels in the lagoon of Venice. Two populations are distinguished: channels on vegetated marshes have lower width-to-depth ratio's than the channels on tidal flats (altered from Hughes et al, 2011).

2.4 Mangroves

A large part of the Guiana coast is vegetated by mangroves. Mangroves are trees or shrubs that grow in the upper intertidal zone, on tropical, low-energy shorelines. It is not one single species, but comprises a large range of plants which are adapted to survive in anaerobic, muddy soils in saline environments that are otherwise inhospitable (Toorman et al., 2018). Their capacity to tolerate salt concentrations in soils (up to three times that of seawater) is associated with efficient use of water during photosynthesis, and particularly effective hydraulic systems (Lovelock et al., 2015). The trees have above-ground root systems, which include pneumatophores, prop roots and buttresses. These provide stability and promote gas exchange. As mud banks on the Guiana coast provide intertidal area, this is where mangroves can grow. Due to the migration of mudbanks, the mangrove vegetation also moves westward along the coast. Mangroves die when soil is erodes on the east side of the bank, and new pioneer mangroves quickly colonize the freshly deposited soil on the west side of the mudbank. Therefore, a certain location along the coast can be periodically vegetated and bare.

Unlike other coasts, the Atlantic coast of the Guianas has only a few mangrove species. The black mangrove (*Avicennia germinans*) dominates the coastal fringe (Figure 10), and red mangroves (mostly *Rhizophora mangle*) grow along the banks of tidal rivers and creeks, rather than at the coast itself.

Mangroves function both as a unique ecosystem as well as a natural soft coastal defence structure (Toorman et al., 2018). Mangroves create highly productive habitats, supporting both marine and terrestrial biodiversity such as fish and crustaceans (Woodroffe et al., 2014). The most important effect of mangroves for coastal protection is that the mangrove roots reduce the energy of the seawater. Waves are dampened and tidal currents and alongshore currents are slowed down. In this way, sediment particles which are suspended in the water column, will sink and be deposited. The soil is therefore elevated, and the land behind the mangroves is (partly) protected from erosion.



Figure 10. Black mangrove (*Avicennia germinans*), with its pneumatophore root system. (Toorman et al., 2018).

2.5 Coastal change in Suriname

Coastal change happens fast in Suriname. On a large scale, it demonstrates an alteration of periods with shoreline propagation and retreat. Between 1947 and 1966, mainly net erosion took place. From 1966 to 2007, the coast showed more and more net accretion (Berrenstein, 2010). This is thought to be attributed to a change in north-east trade wind directions (Augustinus, 2004). Amongst others, De Jong et al. (2021) and Anthony et al. (2016) analysed spatial patterns in erosion and accretion along the Suriname Coast. They found that on locations where mud banks are present, the coastline tends to propagate. The Suriname coast can be divided into three parts of approximately equal length, all bounded by rivers on both ends (Figure 11a). Each section has one or two mud capes in front of the coast (Anthony, 2016). Figure 11b shows the observed erosion and accretion along the Surinam coast since 1947, based on aerial photographs and satellite imagery (De Jong et al., 2021).

Coastal vegetation is also changing. Between 1950 and 2000, approximately one third of mangroves were lost worldwide (Alongi, 2002). This is also happening in Suriname, where a lot of forests have been uprooted by erosion or removed by people making the coast is less protected against the sea. Since erosion is a growing issue and more research is done on the function of mangroves, there is a growing number of (pilot) projects aiming to restore mangrove forests by planting young trees (Toorman et al., 2018).

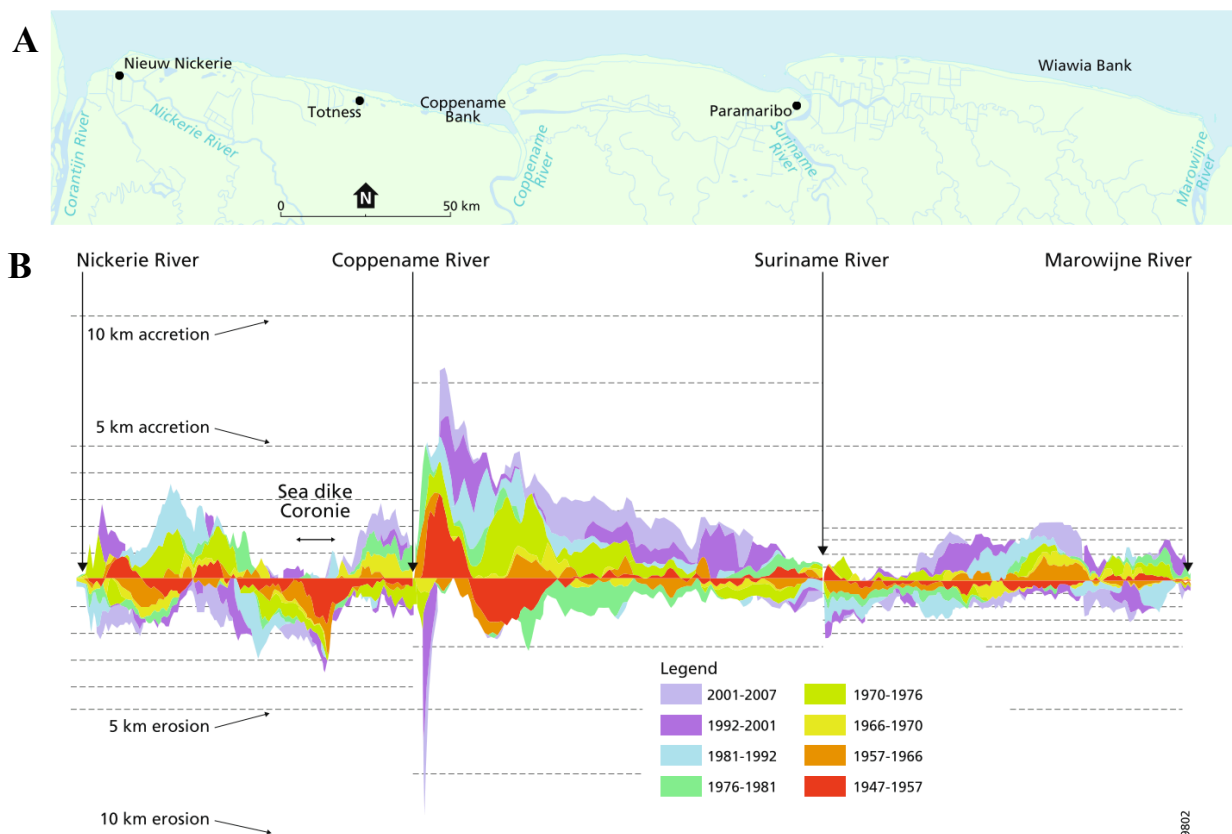


Figure 11. Map of the Suriname coast and its three sections (A), and the corresponding overview of coastal erosion and accretion along the Suriname coast, between 1947 and 2007 (B) (Wong et al., 2017, via Jong et al., 2021)



Figure 12. Location of the study sites, at the coast near the Suriname river mouth, north of Paramaribo, Suriname.

3. Materials and methods

In this chapter, the research area will first be described, followed by the dataset. Then the data processing workflow is explained, and lastly the data analysis is described.

3.1 Research area description

The two study areas are located at Weg naar Zee (WnZ), one of the coastal districts of Paramaribo, Suriname. Weg naar Zee lies ± 5 km west of the Suriname river mouth (Figure 12), and approximately 900 km west of the mouth of the Amazon river. The district has ca. 14000 inhabitants, with a population density of 390 people per km². The main income in the area comes from agriculture. Other major land uses are cattle farming and urbanization (Cete. et al., 2018).

It is located in the vicinity of the sandy beach of Braamspunt cape on the east side of the Suriname river. Currently, a mudbank is present west of WnZ, and it is thus on the trailing edge of the bank. shows the location of the mudbank and the shoreline in 2015. Based on the average speed of 2 km/yr, this mudbank will now be situated ca. 11 km westward. Compared to the rest of the coastal section between the Copename and Suriname rivers, WnZ is an erosion hotspot (Figure 11). Its coastline has been retreating persistently, yet the rate is decreasing in the last years (Anthony, 2016).

The first site, location East, is located directly west of the mouth of the Surinam River (Figure 12). It is a mudflat bounded by a cross-shore dewatering channel on the east side and the dike of the mainland on the southern side. On the northern side and western side of the research area, the mudflat continues. Little vegetation is present, apart from the vegetated dikes. This site has had little human interference. Coastline retreat has approximated to 500 meters since 2003 (Google Earth, 2021).

The second site, location West, is situated 2.2 km west of location East (Figure 12). This part of the mudflat is bounded by the same mainland dike on the southern side, and by another paved levee on the

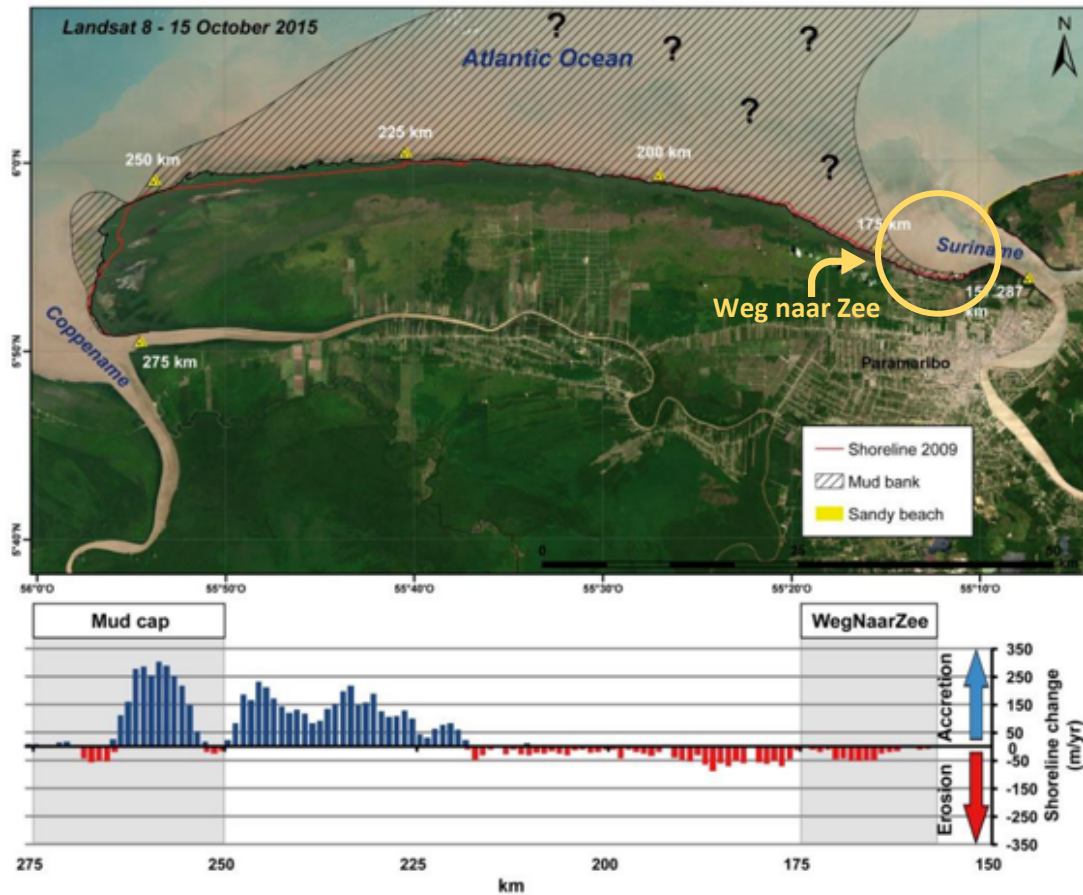


Figure 13. Shoreline changes between 2009 and 2015, between the Coppename river and the Suriname river. The western section shows muddy accretion, whereas the eastern section shows (inter-bank) erosion. (Anthony, 2016)

west side. On the northern side and eastern side, the mudflat continues. There are some vegetated patches here, mainly on the landward side, which is partly natural, and partly planted by the local community as a pilot project in 2015 and from 2017 onwards as part of a mangrove rehabilitation plan, see Figure 14 (Toorman et al., 2018). Furthermore, permeable dams have been constructed as a large block pattern, consisting of 2 parallel lines of poles placed upright in the soil. These are also as part of the pilot project, and are meant to function as sediment trapping units. These dams consist of 3 m long wallaba wooden poles, which are driven into the soil to a depth of 2 m. They are spaced with an interval of 75 cm, in two parallel lines which are 50 cm apart (Toorman et al., 2018). Also, this site has two cross shore wooden jetties, which are built on poles (Figure 15a). Location West has had a coastline retreat of around 500 meters since 2003 (Google Earth, 2021).



Figure 14. A: Newly planted mangroves in West-2019, and two parallel lines of upright poles. B: sprouted mangroves, ready to be planted on the mudflat.

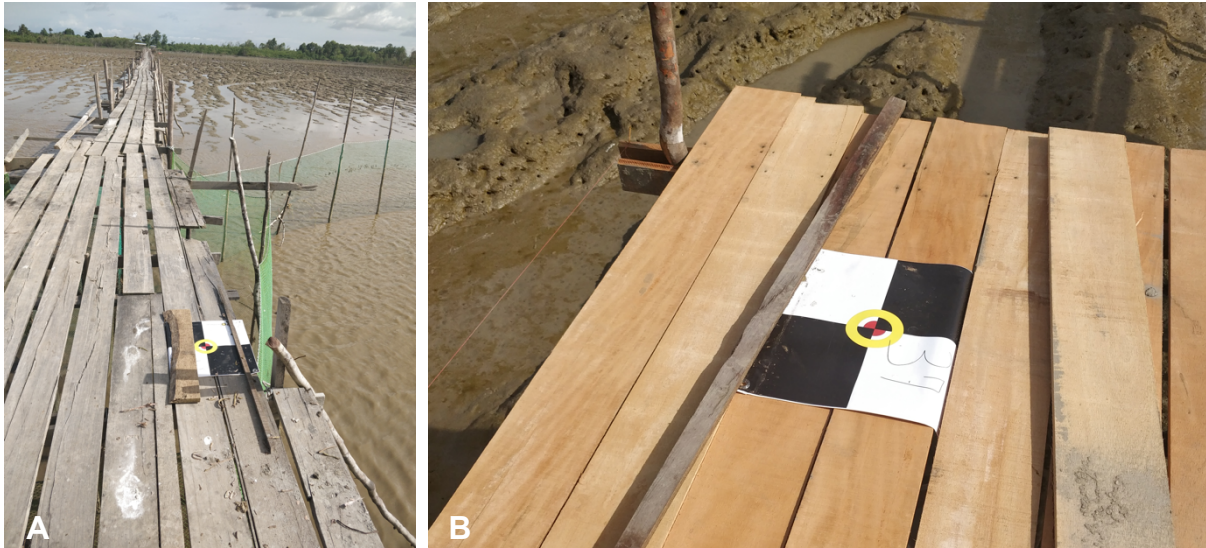


Figure 15. Wooden jetties in the western study site, with examples of Ground Control Points (GCPs).

3.2 Data Collection

The main data for this study is UAV imagery with a resolution of 2,5 cm. The imagery covers the two intertidal locations of ± 500 m x 1000 m that are 2.2 km apart: location East and location West (Figure 12). This data is available for two different moments in time: June 2019 and February 2020. Thus, four surveys were carried out: West-2019, West-2020, East-2019, and East-2020. However, due to camera issues, East-2020 turned out to be unusable. Therefore, three datasets were available in the end.

Ground control points (GCPs) were placed on the ground, prior to flying the UAV. For the location of the GCP's, refer to Appendix A. These GCP's were black and white chequered canvases (Figure 15), of which the centre point coordinates were taken using an RTK GPS, with an accuracy of ± 5 cm. Per UAV survey, several (13, 24 and 28) GCPs were placed, and spread as much as possible along the accessible edges of the study area. No GCPs could be placed on the mud at the northern seaside of the area, as this area was inaccessible. Total numbers of GCP for each survey are different due to practical issues with accessibility. Around two thirds of these GCP's are reserved for correcting the location of the images in the following processing phase, and the others are meant for validation of the results.

Imagery was acquired using the DJI Mavic Pro 2, a consumer-grade quadcopter with an RGB camera, piloted by certified pilot Job de Vries. The DJI Mavic Pro 2 weighs 907 grams, and has a 20MP camera which creates photographs of 3648 x 5472 pixels, using a focal length of 10.26 mm. The maximum flight time is 31 minutes. Due to this battery limitation, multiple separate flights had to be taken for every survey. All flights occurred during low tide, and for each separate survey, all flights took place within a window of maximum 4 hours. The GPS coordinates of the camera location are measured in WGS-84 coordinate system, with an estimated accuracy of ± 10 meters. These coordinates were only used as an initial indication of the photograph location, and later corrected based on the GCP's with the highest accuracies.

The flight plans were created using Litchi waypoint mission planner, which pre-programs the flight route and image capture. Photos were taken from an elevation of 50-75 meters compared to take-off location. For all surveys, this take-off location was on the edge of the tidal flat, within 1.5 meters above the tidal flat elevation. The images have a front overlap of 75%, and a side overlap of 60%. Two photographs were taken at each pre-programmed location: one straight down with a pitch of 90 degrees, and one tilted forward with a pitch of 75 degrees. On all flight days, the weather was alternatively cloudy and sunny. During the image acquisition in 2019, there was little wind, so the UAV could fly at 50 meters elevation. On the fly date in 2020, there were stronger winds, and therefore the flight route was adjusted to an elevation of 75 meters to ensure sufficient image overlap.

3.3 Data Processing

Agisoft Photoscan Professional version 1.4.2 (<http://www.agisoft.ru>) software was used to generate orthorectified images and DEMs from the UAV images. The processing can be divided into three phases.

- First, Agisoft aligns the photos by making use of a Structure-from-Motion (SfM) algorithm which identifies matching features in multiple images. These features are tracked from image to image and are used to produce estimates of the camera positions, camera orientations and coordinates of the features. Outputs of this alignment step are (1) a 3D sparse point cloud of the study area, (2) relative camera positions at the moment of image acquisition, and (3) estimated internal calibration parameters including focal length, principal point location, three radial and two tangential distortion coefficients (Casella et al., 2016). Next, approximately two thirds of the GCP's – which were selected to ensure an optimal spatial distribution of both these correction-GCPs and the remaining validation-GCPs – were manually located in the photographs with an accuracy of ± 3 pixels. The sparse point cloud was filtered with gradual selection tools based on four different selection methods: reprojection error, reconstruction uncertainty and projection accuracy, while alternatively optimizing a selection of camera parameters ($f, cx, cy, k1, k2, k3, p1, p2$), and all parameters selected in the final two rounds. Each selection method was used at least twice, and it was aimed that all methods together would remove 40-60% of the points, depending on the estimated precision of the point cloud. This removal of points aimed to decrease the error which is introduced by false point detections.
- The second phase in Agisoft is the creation of a dense point cloud. The outputs of the first step are used to create a 3D point cloud with more detail. The dense cloud then serves as the main input of the digital elevation model (DEM), by creating a raster with elevation values of the dense point cloud.
- In the third step, a mesh is created from the sparse point cloud, which results in a 3D surface geometry. On this mesh, the UAV photographs are projected. This gives a 3D orthophoto of the entire study area.

This method was suitable for West-2019 and East-2019. Yet, for West-2020 and East-2020 these steps were insufficient, as it turned out the camera of the DJI Mavic Pro 2 had a malfunction in its focus, causing considerable motion blur in the photographs. This aspect in combination with long flight lines, obstructed the processing of accurate results. For East-2020, this problem was insoluble within the available time period, and was therefore chosen to be left out of this research. However for West-2020, the method was somewhat adjusted to create a reasonable Orthophoto and DEM: during the initial alignment, most of the internal camera calibration parameters were kept fixed, rather than letting Agisoft estimate them. Specifically, $f, cx, cy, b1$ and $b2$ were kept fixed, while $k1-4, p1$ and $p2$ were freely estimated by Agisoft. After the alignment, the sparse point cloud was filtered with the same methods, and all parameters except $b1$ and $b2$ were optimized. Furthermore, four extra control points were added in the northern area (point 1, 2, 3 and 4 in Appendix A), as initial attempts for image processing showed issues with doming in that area, partly due to a lack of GCP's on the northern side of the study site. They were assigned an elevation of 25 cm with an accuracy of 20 cm, and a horizontal accuracy of 50 cm. The second and third processing phases were unchanged. The creation of the dense cloud introduced some new inaccurate zones, however this could not be solved.

The Agisoft output that was used for further spatial analysis were the DEM's and the orthophotos of the study areas, which were loaded as georeferenced TIFF files into ArcGIS Pro, for geospatial analysis. This encompasses the maps for East-2019, West-2019, and West-2020, and excludes East-2020 as those maps could not be finalised.

The accuracy of the maps (orthophotos and DEM's) was determined using the coordinates of the remaining 9 GCP's as a reference. The coordinates of those GCPs were plotted in ArcGIS, and compared to the location of the GCP in the orthophoto to determine the horizontal error. For the vertical error, the GCP y-coordinate was compared to the DEM-elevation at its location.

3.4 Orthophoto classification

For the data analysis, classified maps were made based on the orthomosaics. This was done manually in ArcGIS, on a zoom level of 1:250. The following classes and elements were visually identified:

- Vegetation
 - o Visibly green
 - o No green visible
- Human structures (e.g. dams and jetties)
- Mean high water line (interpreted from change in colour of the mud and channel pattern)
- Bare mud
 - o Low relief (no channels)
 - o Medium relief (few channels)
 - o High relief (continuous channels and pits pattern)

These classified maps, together with the DEMs and orthomosaics, were then used to visually assess potential patterns in vegetation, sediment, relief, and objects in the study areas. The classified maps were compared both spatially (East-2019 and West-2019) and temporally (West-2019 and West-2020).

3.5 Channel Geometry

Furthermore, the DEMs and orthophotos were used to locate and analyse channel geometries, through ArcGIS and R software. First, 10 to 12 large channels were chosen in both West-2019 and East-2019, and a polyline was drawn along the centre of the channel using a zoom level of 1:150. Transects were then created in ArcGIS perpendicular to the channel with intervals of 40 meters and a length of 5 meters. Points were created on these transects and on the original channels, with a distance interval of 0.025 m, to which the corresponding surface elevation data of the DEM was allocated. These steps were all executed from a model which can be found in Appendix B. The elevation and coordinates of the points were exported to R for further computation of the channel geometries.

In RStudio, the elevation along the channel was visualised into profiles. This was used to analyse absolute values of the elevation in different study areas and different locations within each area, as well as to analyse elevation differences within one channel. In this way, channels with severe doming could be identified, and a general overview of the channels could be formed. Next, the points of each separate transect were displayed in a graph by their elevation against the distance along the transect (Figure 16). From this graph, the location of the two channel edges was visually chosen and the associated points were selected. This point was set at the break point of the bank, recognised as a clear discontinuity in the profile. However, it was not possible to create a systematic numerical definition to choose this point, as there was too much variation between the profiles. For every transect profile in R, it was checked on the DEM if the channel was actually visible, to prevent false geometries to be included. If no channel was visible on the DEM, or if it was impossible to define the channel boundaries in the profile, that transect was excluded from the geometry dataset. After allocating the channel banks, the calculated width between the chosen channel edges was returned. Also, using the channel edge with the lowest elevation, the width between this point and the opposite bank of equal height was calculated, and the depth and area below these points were computed. To calculate the channel bed slope, the elevation of each point was compared to the elevation of the transect on its seaward side. The difference was regarded as the slope at that location.

It was then evaluated what relations could be distinguished between the channel geometry values on the one hand, and cross shore location, along shore location, and distance along channel on the other hand. Cross-shore location and along-shore location was approximated by taking the y-coordinates and x-coordinates of the transects, as the shoreline is almost – yet not completely – east-south orientated.

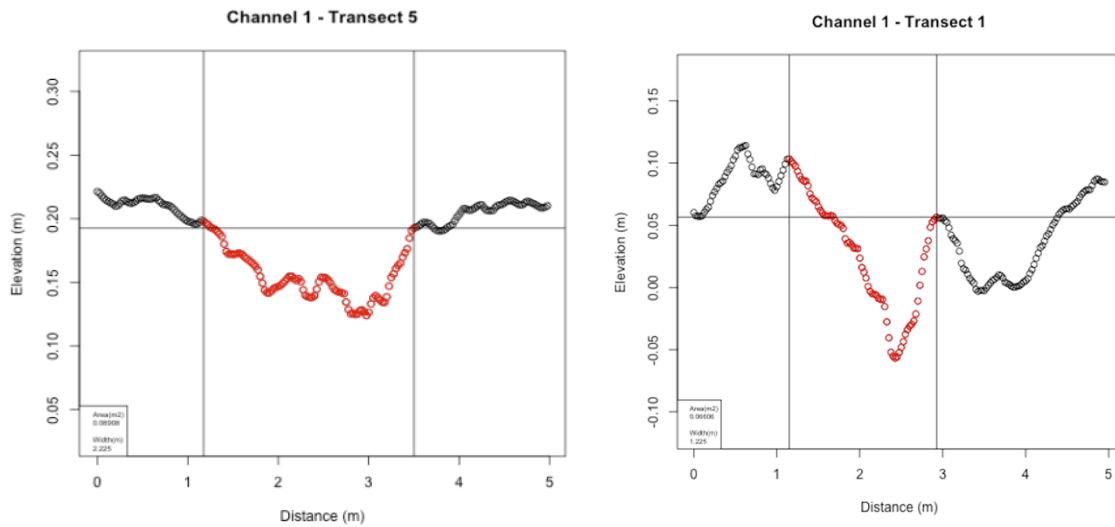


Figure 16. Examples of transects and the identified channel boundaries in RStudio.

3.6 Elevation differences

To quantify sedimentation and erosion between 2019 and 2020, it was first attempted to create an elevation difference map of West-2019 and West-2020. However as doming and local extreme values of 2020 were overshadowing the small actual elevation differences, this was not possible for the whole region. As a supplementary method it was chosen to determine relative sedimentation: in both DEMs, the elevation of objects that were assumed to be of constant elevation was compared to the elevation of the sediment next to it. This was done by creating transects in ArcGIS and retrieving the elevations of the objects and the sediment surface in RStudio. The change in this difference was regarded as the local erosion or sedimentation. The combination of de elevation difference map and the relative sediment measurements was used to formulate an estimate of the amount of erosion and/or accretion between 2019 and 2020.

4. Results

First, the output will be described in section 1. This comprises the accuracy and quality of the orthophotos and DEMs, and a description of the spatial and temporal changes observed from the orthophotos, followed by a description of these changes in the DEMs. Section 2 shows the results of the channel geometries which are found through transect analysis. Lastly, absolute and relative elevation differences are presented in section 5.

4.1 Imagery and map output

Processing the UAV imagery in Agisoft gave the output orthophotos shown in Figure 20a, Figure 21a, and Figure 22a. Visual interpretation of these orthophotos resulted in the classified maps shown below the orthophotos. These maps are distinguishing between human structures, vegetation (green and not green), and bare mud (high, medium and low relief). The output DEM's are shown in Figure 25, 26 and 27. Enlarged displays of the orthophotos and DEMs can be found in Appendix D. As processing the maps for East-2020 did not succeed, these are not included. In the following paragraphs, the quality of the output is examined, and the spatial and temporal differences observed from the orthophotos and DEMs are explained. A summary of the spatial and temporal differences is provided in Table 2 at the end of this paragraph.

4.1.1 Output quality

The statistics of the image acquisition, image processing and outputs are listed in Table 1. For West-2019, 17 GCP markers were used for processing and 7 were used for validation, For West, this was 17 and 11 respectively, and an additional 4 extra markers were added during processing in an attempt to reduce the doming effect. East-2019 was processed using 9 GCPs and validated using 4 GCP's, so this dataset had the lowest number of control points. Based on GCP validation, West-2019 has the best total accuracy of 0.044 m. The vertical accuracy of West-2020 and the horizontal accuracy of East-2019 were relatively high, respectively 0.111 m and 0.146 m. The resolution of the orthophoto's is ± 2 cm/pixel, and the DEM has a coarser resolution of ca. 3.7 cm/pixel (West-2019 and West-2020) and 5.1 cm/pixel (East-2019) (Table 1). These resolutions are high enough compared to planned point interval of the transect analysis, which is 25 cm (see paragraph 3.5).

Figure 17 displays the Image overlaps of all three surveys. In a margin around the edges, anywhere between 1 and 8 photos are available. Apart from that, the majority of the areas have 9 or more images for every location. Estimated camera locations are also given in Figure 17. For West-2019 and East-2019, these show neatly aligned dots, which are in accordance with the UAV flight plans described in paragraph 3.2. However, estimated camera locations West-2020 show disturbance, especially in the middle of the study area, which do not correspond with the flight plan. As camera locations were set to be not adjustable during processing to prevent larger errors, this indicates that the input GPS data from the camera locations often had a significant offset.

These same camera locations are showed in Figure 18, this time with their associated error estimates. As for West-2020 these locations were fixed, no changes were made and no errors can be estimated. The figure shows that East-2019 had much larger vertical errors in camera location, as most values are around 40 m. In Figure 18, also the camera orientations and associated errors are given. For East-2019, these errors are relatively small, and constant, except around the eastern edge. For West-2019, camera orientation errors are more irregular, with some large outliers.

Table 1. Statistics of image acquisition, processing and outputs.

Area	West 2019	West 2020	East 2019	
Extent (m)	North	653,034.900700	653,220.259000	652,202.571700
	South	651,969.018100	651,920.585600	651,288.022600
	East	696,074.801300	696,038.449400	699,365.620600
	West	697,594.112800	697,620.761000	700,731.782900
Coverage area (km²)	0.537	0.638	0.371	
Approximate flight elevation (m)	50	75	50	
Approx. side spacing (%)	75	75	75	
Approx. side overlap (%)	60	60	60	
Nr of flight lines	6	9	7	
Length of flight lines (m)	830 and 550	950	900	
Nr of photos	1102	1456	1215	
Nr of points in sparse point cloud (nr used of total nr)	500,727 (49%) of 1,015,463	600,352 (43%) of 1,407,916	531,509 (43%) of 1,222,282	
Nr of points in dense point cloud	400,805,666	549,933,653	136,623,172	
Nr of GCPs used for processing	17	17 + 4 extra markers	9	
Nr of GCPs used for validation	7	11	4	
Horizontal accuracy (m)*	0.0298	0.0355	0.146	
Vertical accuracy (m)*	0.031	0.111	0.047	
Total accuracy (m)*	0.044	0.116	0.153	
Resolution Orthomosaics (m/pixel)	0.0183	0.0186	0.0200	
Resolution DEM (m/pixel)	0.0367	0.0372	0.0515	
DEM Point Density (points/m²)	744	722	378	

* measured from the validation GCP's

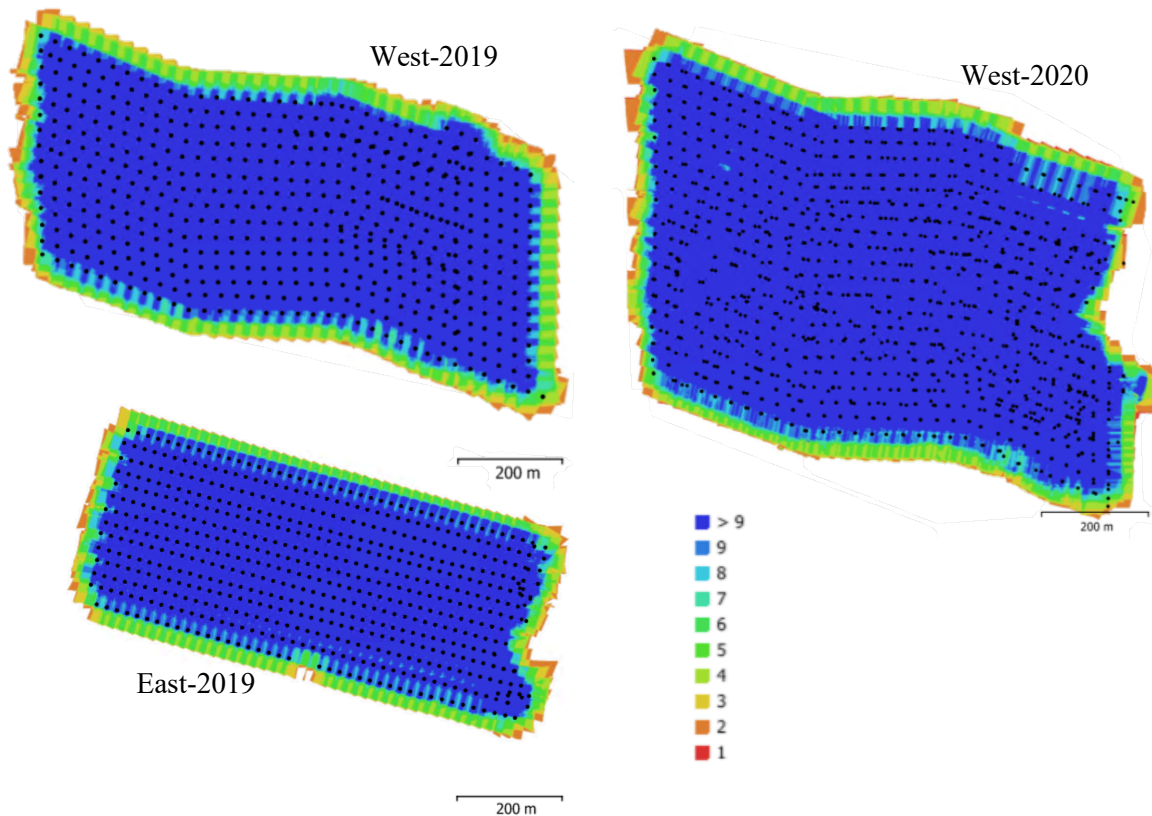


Figure 17. Camera locations (dots) and image overlap (colours) of the image processing in Agisoft.

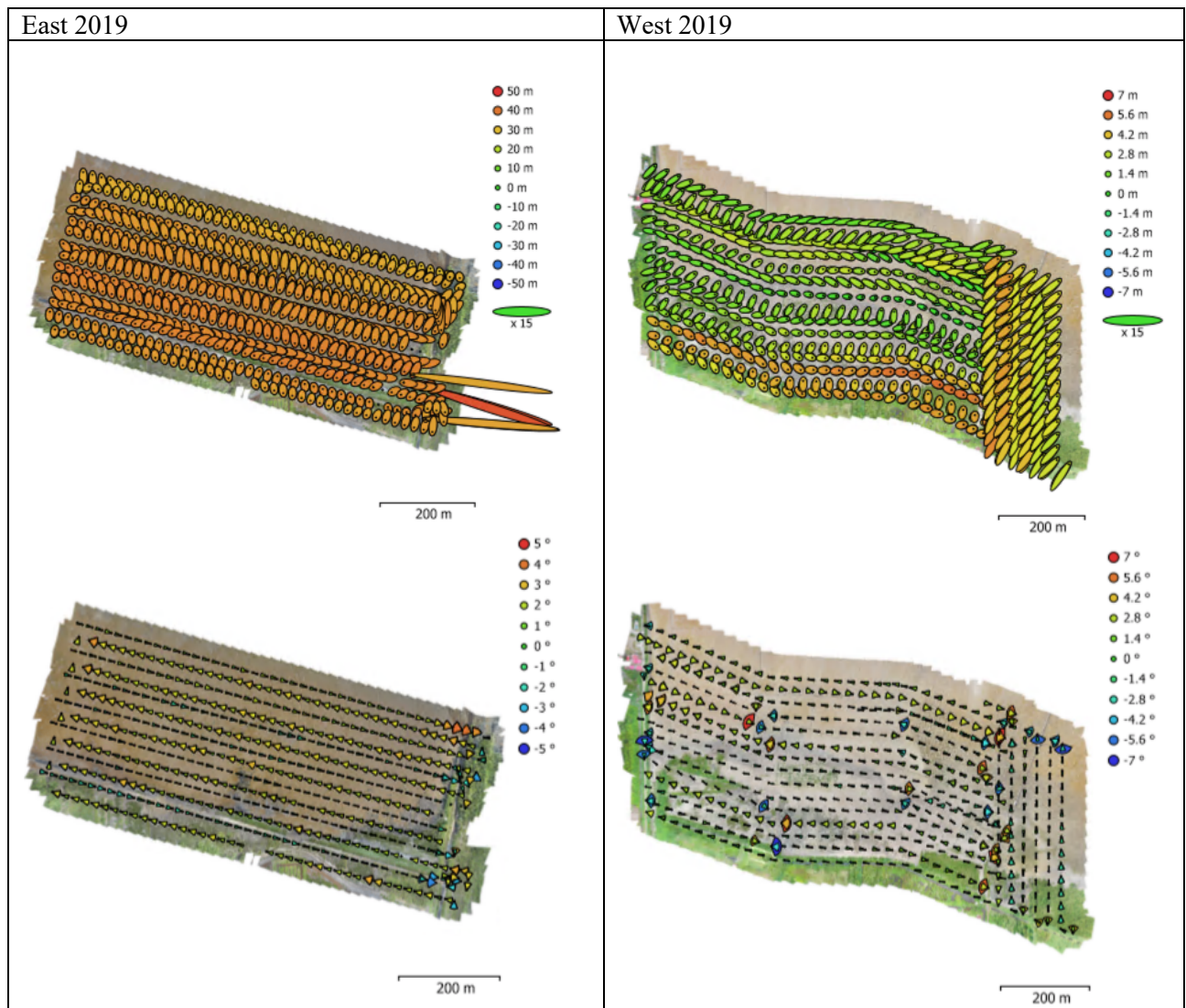


Figure 18. Camera processing data and error estimates, for East-2019 (left column), West-2019 (right). Note the different colour scales. Top: camera locations and associated error estimates (Z error is represented by the ellipse colour, and XY errors by ellipse shape). Bottom: camera orientations and associated error estimates, the arcs represent yaw error estimates. West-2020 has no errors for camera locations and rotations, as these were not adjustable during alignment.

4.1.2 Differences in orthophotos and classified maps

The orthophoto and classified map (Figure 20, Figure 21, and Figure 22) for East-2019 show that this mudflat has a medium relief morphology throughout the area, with homogeneously brown coloured sediment. Channels are parallel and relatively straight, mainly stretching from north to south. Although some channels do show meandering, most channels would be best described linear dendritic and dendritic networks (Figure 19), according to the classification of Hughes et al. (2011), see paragraph 2.3. The channels are characterised by a lighter colour than their surrounding sediment. The mudflat is largely unvegetated. Vegetation is present in the corner between the dike and the dewatering channel levee (sign *i* in Figure 20). This mainly consists of low shrubs, and some higher trees on the outer edges of the mudflat. Also, a group of dead trees is observed more in the centre-south of the study area (sign *ii*). The sediment on the seaside of the living vegetation patch and on the landside of the dead vegetation patch has a darker, grey colour, and shows more heterogeneous patterns. Furthermore, multiple isolated standing dead trees and lying dead wood are spread throughout the area, the latter lying primarily in a north-south direction. Light coloured sediment is surrounding the dead wood and trees, and channels are often coinciding with them. No artificial objects can be identified on the mudflat itself. However on the southern side, a relict from a coastal defence dam can be identified (*iii*), as well as the remains of a dike (*iv*). The dike is still present on the south-east-side, and has an elevation of ± 3 m. On other locations, the dike has been removed, and the erosional footprint is still visible. On locations where the dike is no longer present, elongated pits show signs of erosion on the landward side of the original dike location (*v* and *vi*).

The sediment in West-2019 is more heterogeneous (Figure 21). Largely, three sections can be distinguished. A strip with a width of ± 100 -200 m along the coast (*i*) is grey coloured and has medium, irregular relief. On the east of this section, a green coloured patch is visible, with some areas showing a mud crack pattern (*ii*). A second section is present in the northwest (*iii*), where the sediment is light brown, and it has a medium relief with some channels passing through. The boundary between these sections has higher relief, with a denser channel and pit network. In these first two sections, the channels are meandering more than in East-2019 (Figure 19) and the pattern is closest to the meandering dendritic network according to the classification of Hughes et al. (2010). These channels include third order and fourth order channels (see 2.3). Some channels contain lighter coloured sediment than its surroundings, while others contain darker sediment. The north-west of this study area shows a very high relief area, with dark brown coloured sediment (*iv*). The relief is caused by a regular, continuous pattern of alternating channels and pits, with an orientation that is on average N-NE to S-SW, but which varies more going shoreward. The pattern is unlike all categories in the aforementioned classification but is most similar to the “complex” pattern. The boundary between the landward grey sediment on one hand and the second and third section on the other hand, corresponds to the interpreted mean high water line, and zones of increased relief are present on both sides of this line, caused by increased channel formation. In the area above this line, still signs of occasional inundation are visible, such as channels and accumulated dead wood (*v*). Furthermore, well-developed vegetation is present in large dense rectangular patches in the south-east (*vi*), and in lines in the south-west (*vii*), which contains mostly tall trees and shrubs. Furthermore, a patch with small trees in a grid is present in the middle of the area (*viii*), which is the rehabilitation project. Some isolated patches of low shrubs are located on the landward side of this. All vegetation is above the high-water line, within the area with grey sediment. Multiple artificial structures are present: two cross-shore jetties extend on to the mudflat, and a block pattern is formed by permeable dams, which is part of the sediment trapping project. These dams have some openings, mostly on the along-shore dams and some on the cross-shore dams. Channels are often deflected when intersecting with a dam, and then run along the dam, and a gully is usually present around the dam. Lastly, multiple isolated human objects are lying in the area, primarily on the landward side.

The zonation of the sediment is different in West-2020 (Figure 22). Three sections can be distinguished, which are all parallel to the coast. The landward strip (sign *i*) is still similar to the one in West-2019. It has a grey colour, and medium relief. The green patch on the east of this zone has faded and is no longer present; this is now green sediment, and the mud crack pattern has become more evident (see Figure

23a for a close-up). The second, middle section (ii) is light, beige coloured sediment with very little relief and a uniform colouring. Third, the section on the seaward side has an orange colouring (iii). This section has much relief, which is very irregular. Several channels are visible, and elongated depressions with a cross-shore orientation. Also some large scale patterns have an alongshore direction (iv). However, since the majority of this section is not included in West-2019, it cannot be compared to the previous situation. The high-water line has moved shoreward in some places, with 20 – 40 m. As no other lined can be distinguished on the middle section, it is likely that the high-water line corresponds to the boundary between the shoreward and the middle section. Vegetation is largely similar to West-2020. The rectangular patches in the south-east (v) are still the same. The vegetation in the southwest (vi) is also the same, apart from the northwest end of this patch. There, trees have disappeared and smooth sediment is now present on that location (see Figure 23b). The mangrove patch from the rehabilitation project (vii) has developed heterogeneously. Figure 23c shows a close-up of this patch. On the north-western part, most mangroves have grown, these are mostly the mangroves that were already relatively large in 2019. The southern edge of the western part has mostly disappeared. On the east side of the patch, some mangroves are left, but the majority has disappeared. The jetties are still present, the western one has been renewed in the meantime. Most of the permeable dams are still visible on the same location, apart from some segments of the westernmost dams which have disappeared or are less distinct (Figure 23d). Also, the dams no longer show gullies around them.

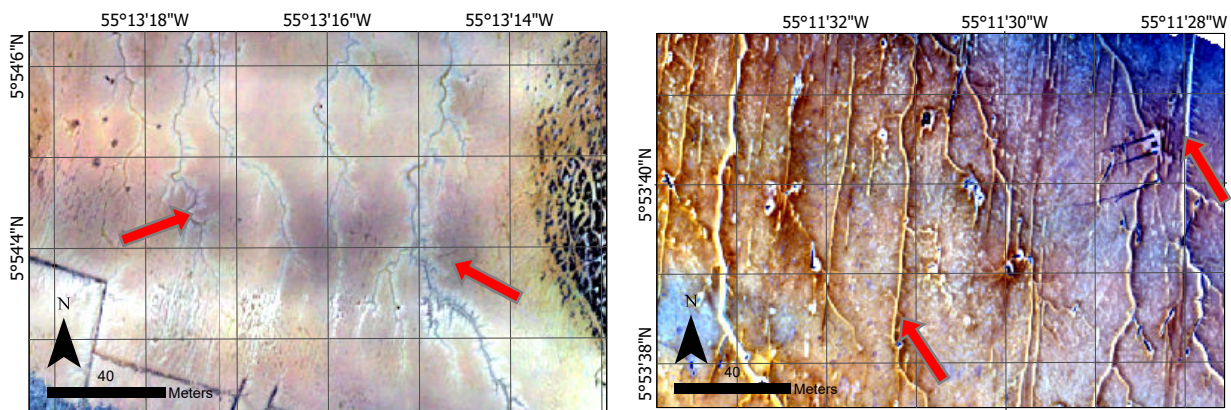


Figure 19. Examples of the typical channel network patterns in West-2019 (left) and East-2019 (right), shown with increased contrast to enhance visibility. Channels in West-2019 have a stronger meandering and are dendritic, whereas East-2019 channels are straight, and parallel rather than dendritic.

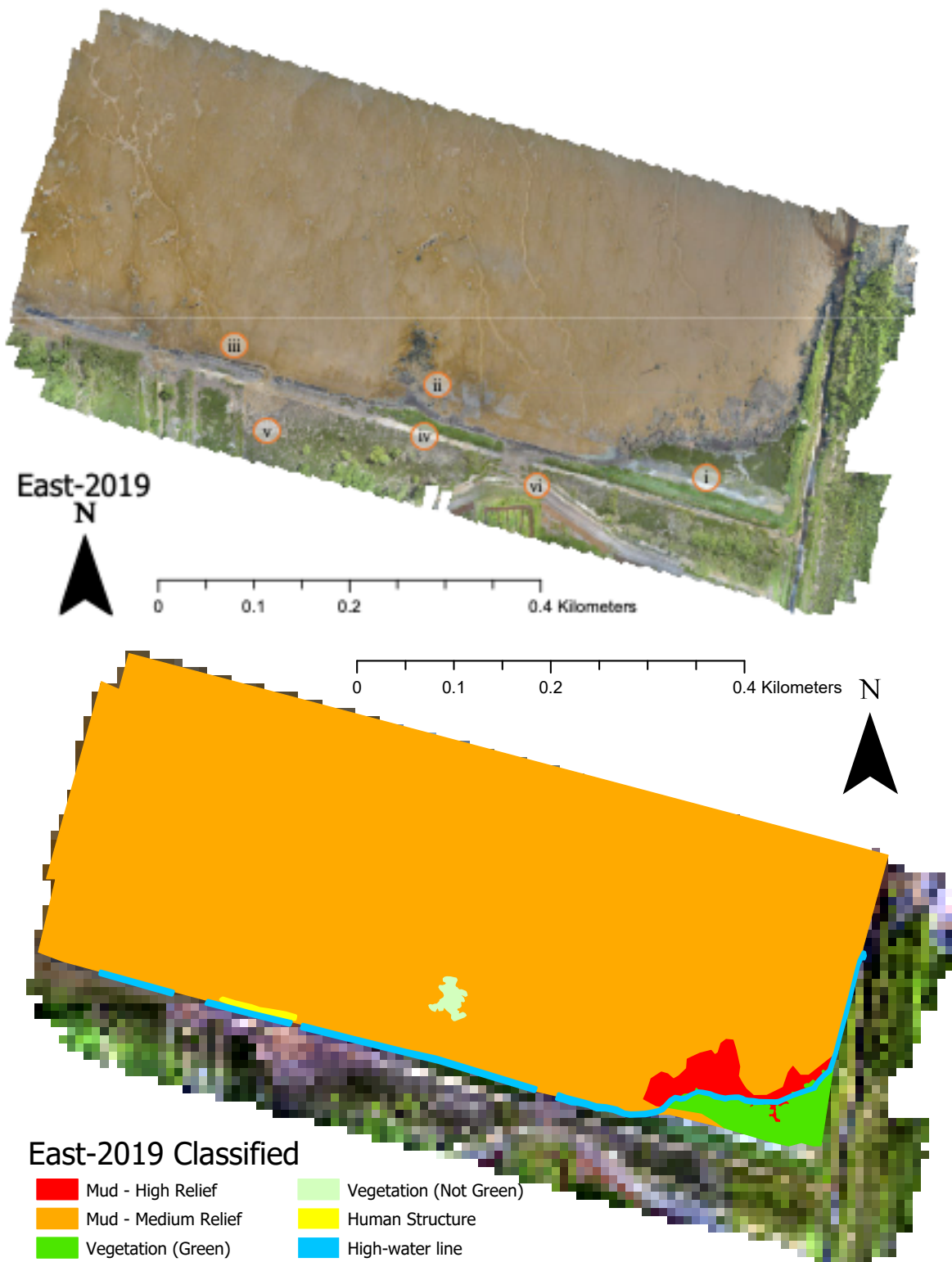


Figure 20. Orthophoto and classified map for East-2019

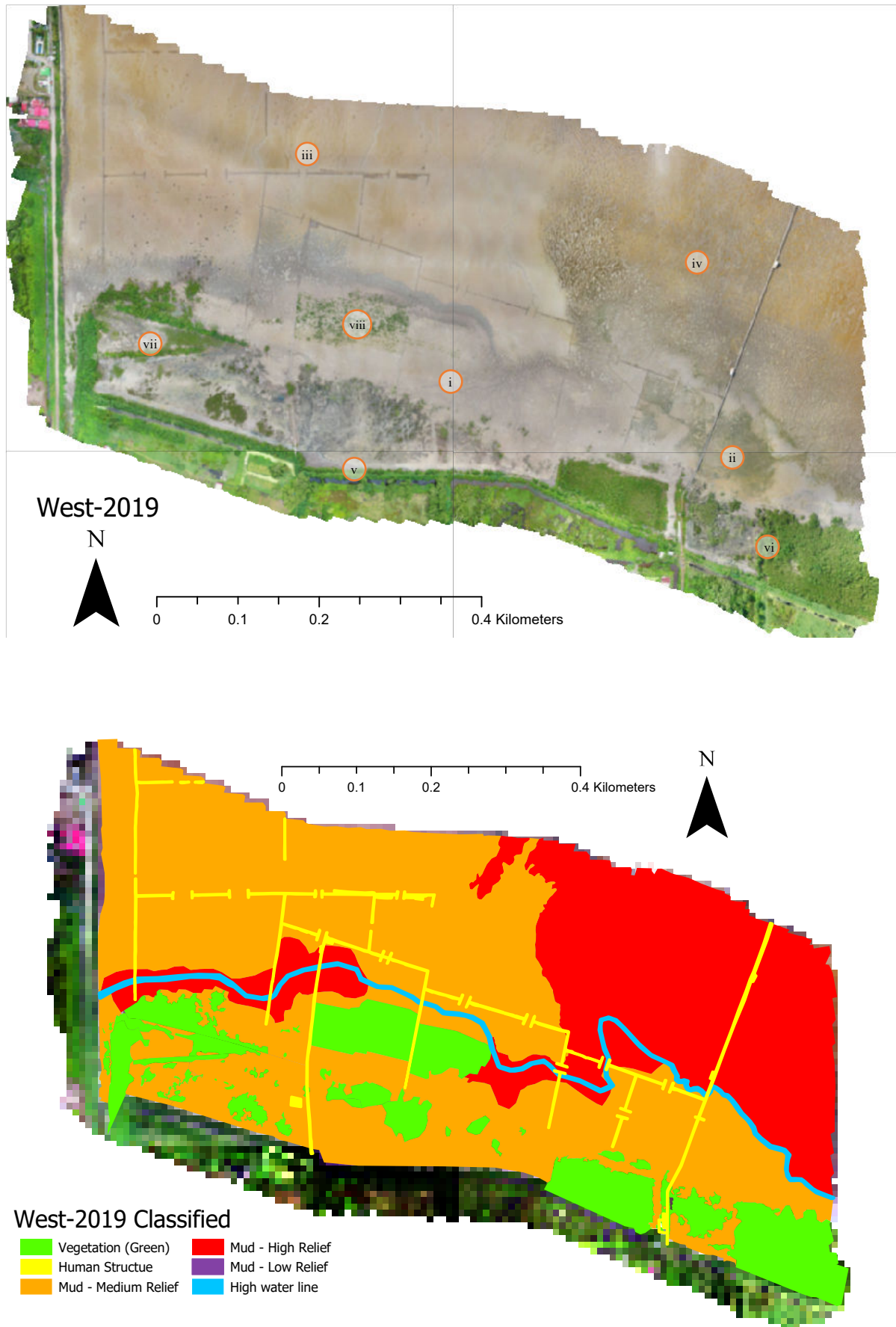


Figure 21. Orthophoto and classified map for West-2019.

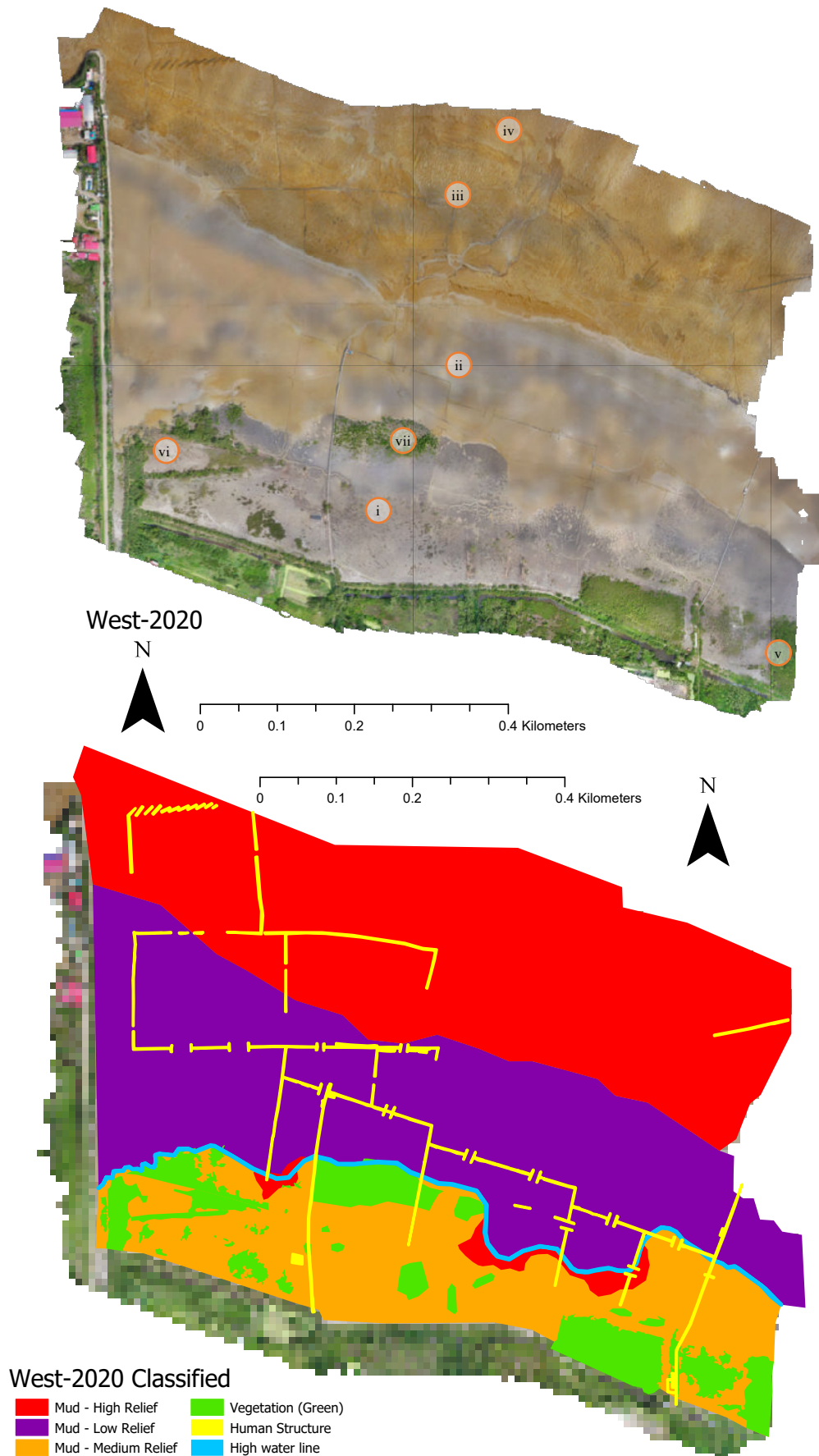


Figure 22. Orthophoto and classified map for West-2020.

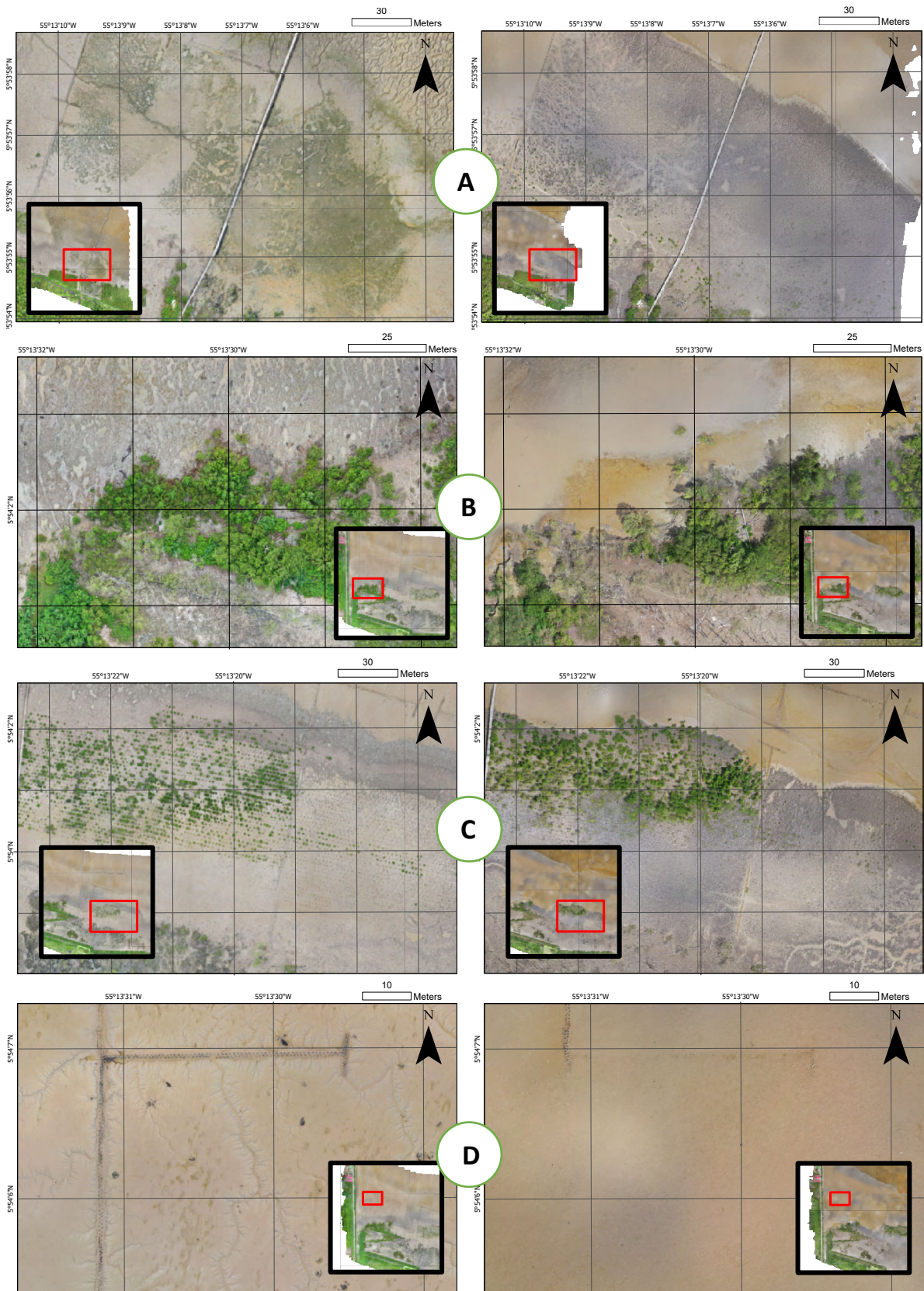


Figure 23. Close-ups of differences between West-2019 and West-2020. A: green coloured patch has disappeared and stronger mud cracking is visible in 2020. B: the northernmost edge of the vegetation has disappeared and smooth sediment is now visible. C: some of the trees on the planted mangrove patch have grown (northwest) and some other areas the trees are gone (east). D: the dams on the west end of the area are not visible anymore

4.1.3 Differences in DEMs

The DEMs are presented in Figure 25, Figure 25, and Figure 26. The mudflat in East-2019 has an elevation range to -0.25 to 0.75 m. It decreases to the north-northeast, but in the north-west corner the elevation increases. At the south-eastern corner, the elevation locally increases to 2-3 meters on the locations where vegetation is present in the orthophotos (sign *i*). Also around the patch of dead trees, the elevation increases to 1.25m (*ii*). Right in front of the coastal defence relict, a depression is visible (*iii*).

In West-2019, mudflat elevations range from -0.25 m to 1.5 m (Figure 25), and decrease in northern direction. A relatively steep edge is visible between the aforementioned grey sediment and light brown sediment sections (*i*), corresponding to the location where the high-water line was specified in the orthophotos. The elevation of the high-water line is approximately 0.8 – 0.9 m. All vegetation clusters are located on the landward side of this line (*ii*, *iii*, and *iv*), where sediment has elevations of at least 1 m, and mostly 1.25 – 1.5 m. The vegetation itself can locally be more than 7 meters high. Around the sediment trapping dams, gullies are visible (*v*). Furthermore, the patterns in the north-eastern area can be recognized (*vi*), where elevation differences between the channels/pits and the adjacent banks are usually 20-40 cm.

During processing of West-2020, doming occurred in the centre and north side of the DEM (Figure 26). In this doming area, values increase to >10 meters of elevation (sign *i*). Furthermore, some zones with large errors are visible in the west and in the far east (*ii*). Neglecting these areas, the rest of the surface elevation also shows higher values than in 2019. Looking north-west of the western jetty (*iii*), values range between 0 m and 1.25 m, and an elevated bar seems to be present with an along shore orientation and an elevation of up to 2 m (*iv*). Despite the doming effect, it is visible that this elevated bar continues eastward, following the landward side of the boundary between the two sediment sections as shown in figure (Figure 22). This bar was not yet present in 2019.

Table 2. Summary of spatial and temporal differences.

	East-2019	West-2019	West-2020
Bare mud elevation range	-0.25 – 0.75 m	-0.25 – 1.5	0 – 1.5 (uncertain)
Sediment	Homogenous brown colour, no zonation	Zonation parallel to coast, Grey sediment is higher elevated, beige sediment is lower, brown sediment has strong relief	Beige and brown sediment of West-2019 is covered in homogenous light sediment. Seaward, high relief sediment zone.
Channels	Linear dendritic / dendritic. Some meandering	Meandering dendritic	Less channels. Those left are meandering
Vegetation	Alive: in corner between 2 dikes. None on mudflat Dead: several single dead trees throughout study area, larger patch on mudflat	Alive: along southern dike, and newly planted patch on mudflat. More vegetation than East-2019 Dead: close to coast	Similar to West-2019. Trees on the north of the western patch are gone. At the planted patch, some have grown, some have died.
Human intervention	No visible intervention on the mudflat. Remnants of dike and dam on the south, levee on the east	Dams, two jetties, planted mangrove forest	Same as 2019, western jetty is renovated

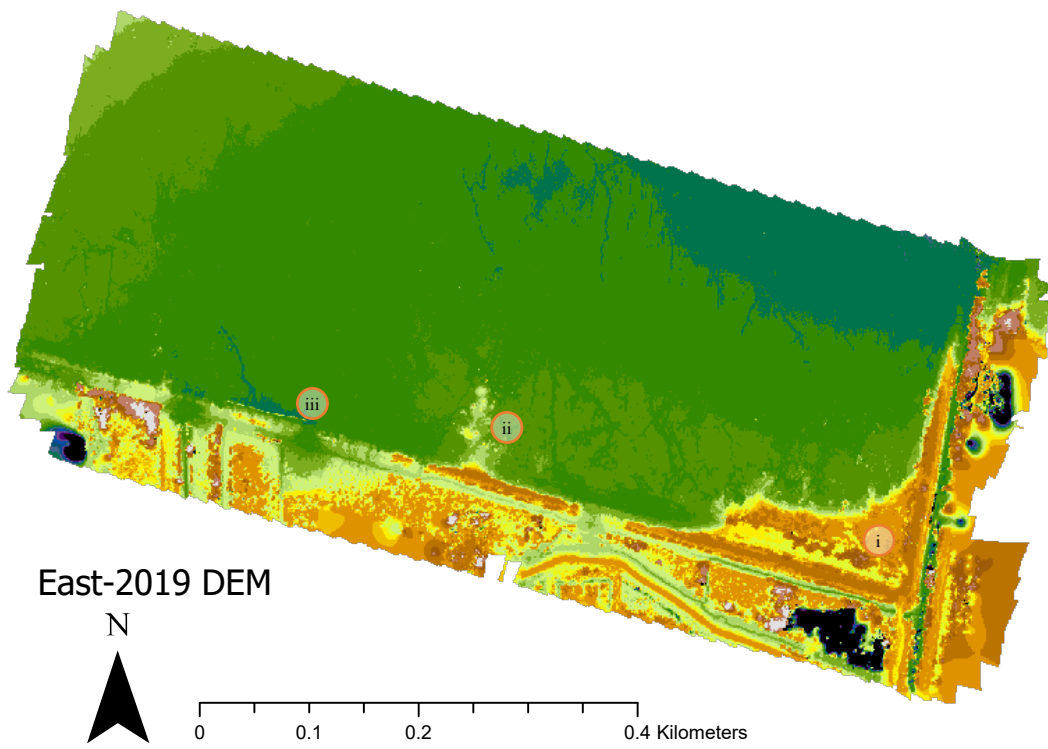


Figure 25. DEM for East-2019

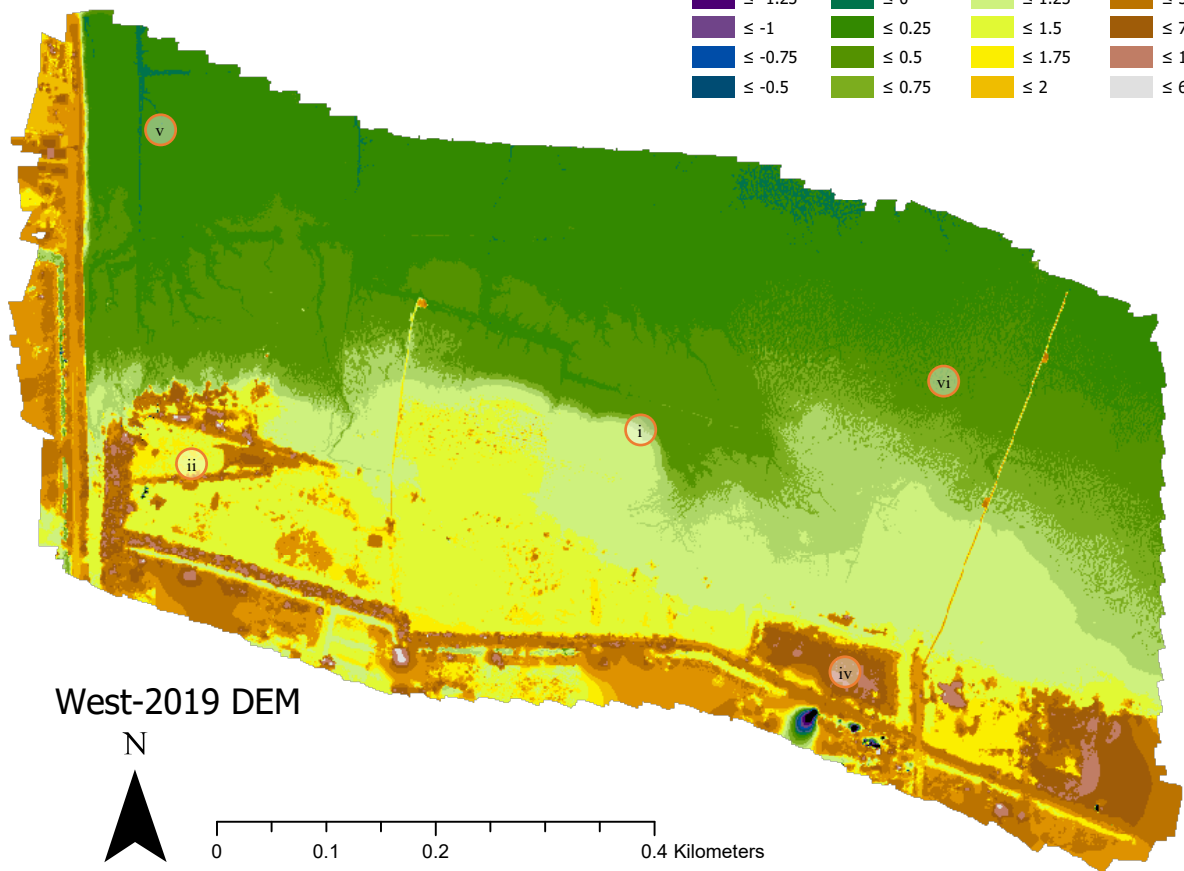


Figure 25. DEM for West-2019

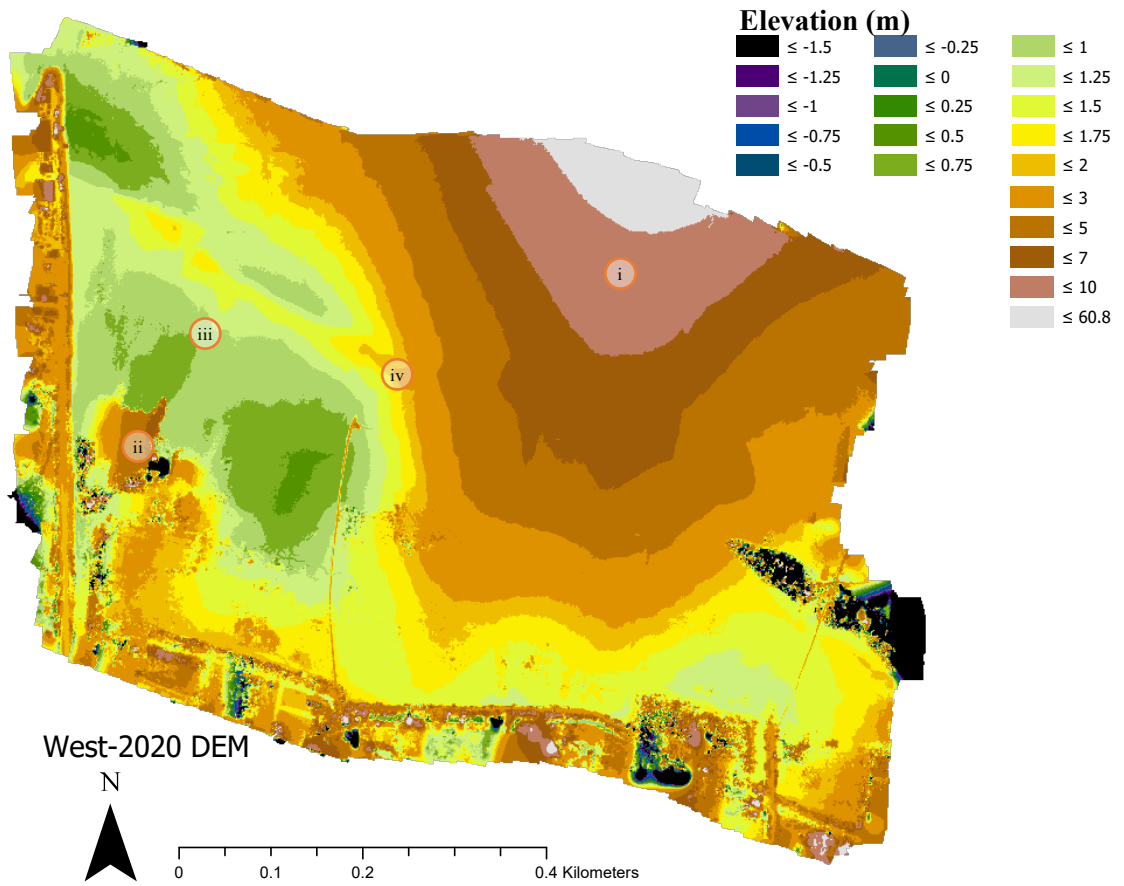


Figure 26. DEM for West-2020

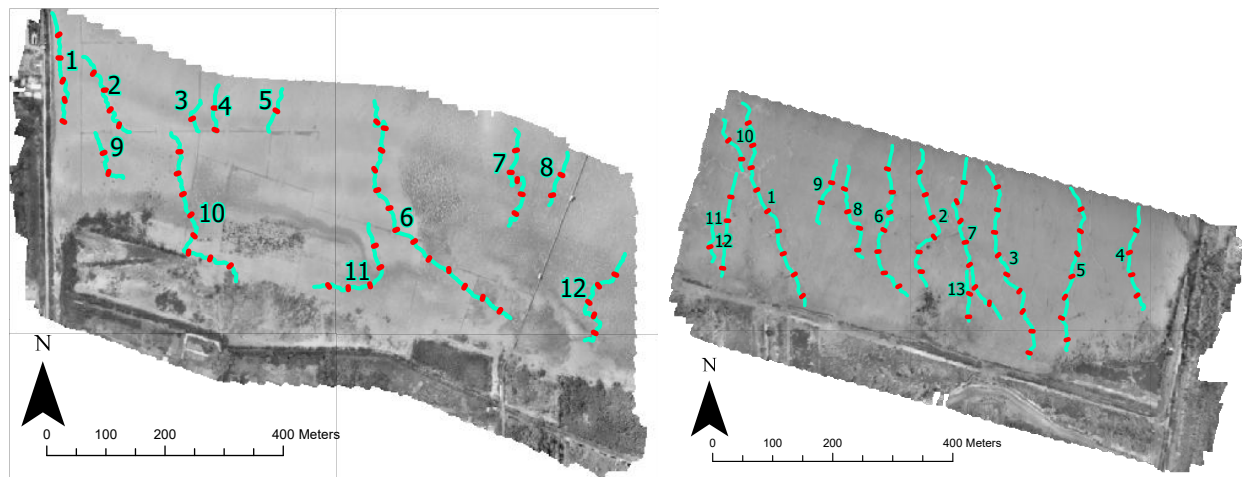


Figure 27. Location of the channels and their transects chosen for geometry analysis in West-2019 and East-2019. For West-2020, the same channels and transects were used as for West-2019.

4.2 Channel Geometry

4.2.1 Channel elevation

The channels and transects that were used for geometry analysis are displayed in Figure 27. A larger version of the channel locations, projected on the DEM can be found in Appendix E. The elevation of the channel bed is plotted over the channel distance from the seaward side ($x=0$) to the landward side, shown in Figure 28. At West-2019, all channels are increasing in bed elevation, and this increase becomes stronger when going landward. In East-2019, most channels are also showing an increasing elevation in landward direction but some channels (1, 10, 11, 12, which are all located on the western side) show an opposite trend. Comparing this to the DEM, it becomes evident that these channel data are influenced by doming from the northwest corner of the study area. Their absolute height data is therefore inaccurate and will not be taken into account for further analysis. However relative elevation differences within the transects seem to be accurate on the DEM, so geometry values can still be derived. The same is true for channels 5, 6, 7 and 11 of West-2020. Furthermore, channels 8 and 12 are located on the edges of the DEM of West-2020, causing both very extreme values and missing data. These channels are therefore excluded from all further analysis for absolute elevation as well as channel geometry. When excluding the channels with doming effects, the average slope of the channel bed can be calculated (Figure 28).

In East-2019, the channels have an average bed gradient of $\pm 0.6\text{m/km}$. In West-2019, this is 1.9m/km . These numbers serve as an indication for the total study areas, but are very dependent on location. Furthermore, starting points and end points, as well as length of the channels, differ strongly between the surveys. Looking more closely at the individual channels, in East-2019 (Figure 28b), the sections of the channels that are included in the analysis are between 8 and 360 m long. They start at a bed elevation of anywhere between -0.5 and 0.17 m, and most end between 0.5 and 1.5 m. The channel sections in West-2019 are 80 to 520 m long and start at an elevation of $-1 - 0.4$ meters, and most of the longer channels end between 0.7 and 1.1 meters. In West-2020, the channels that are not influenced by doming are 80 to 320 m long, start at a height of $0.75 - 1.5$ meters, and they remain in that same range.

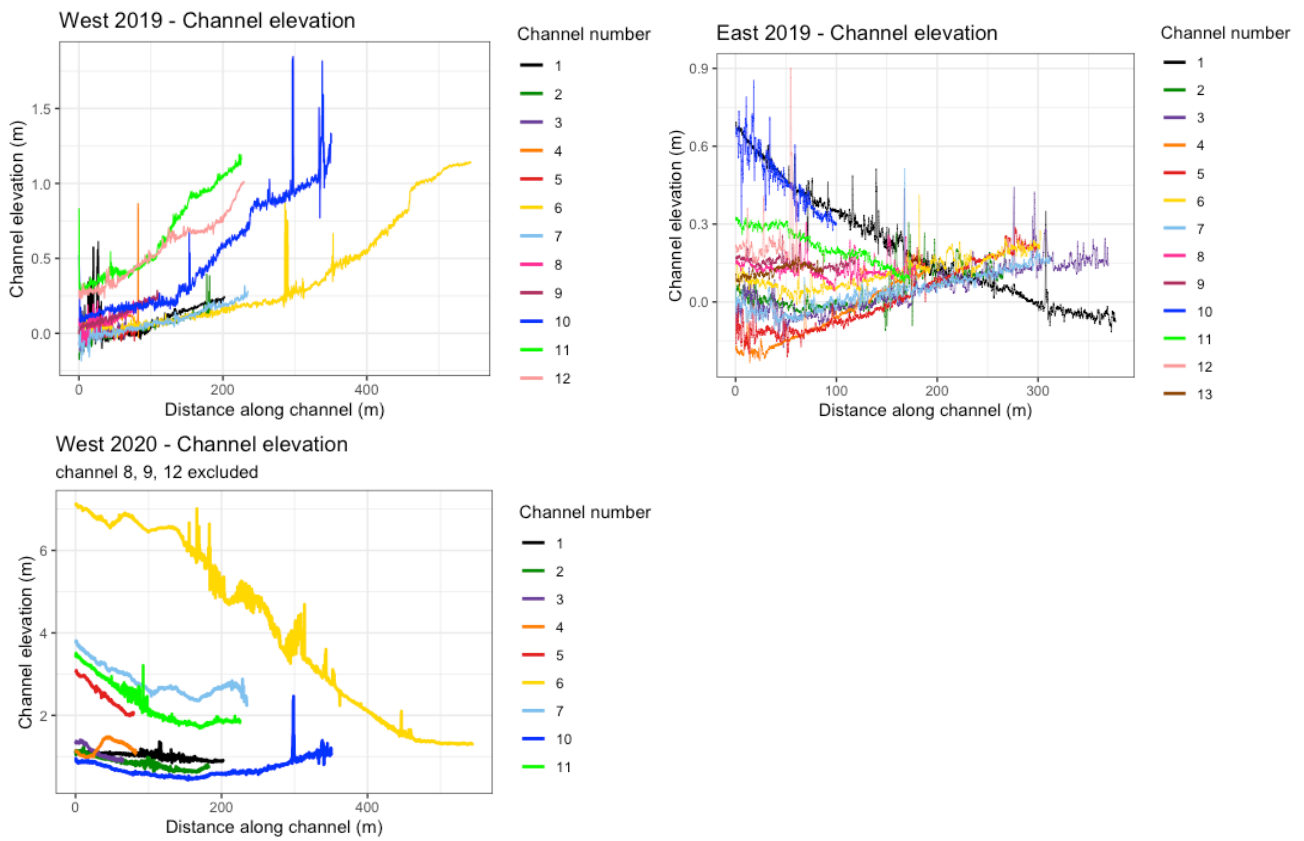


Figure 29. Elevation of the channel-polyline, depicted over the distance along the channel. Left ($x = 0$) is the most seaward end of the channel polyline, and towards the right of the graph is the landward direction along the channel.

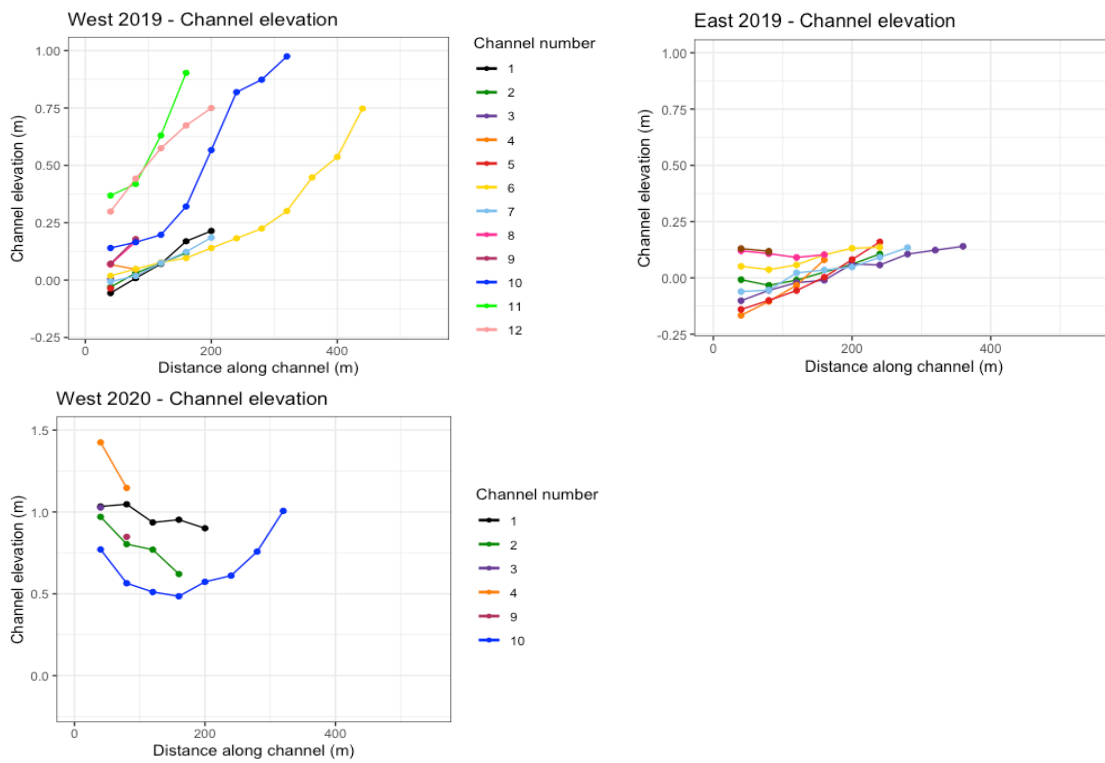


Figure 28. Channel bed elevation over the distance along the channel.

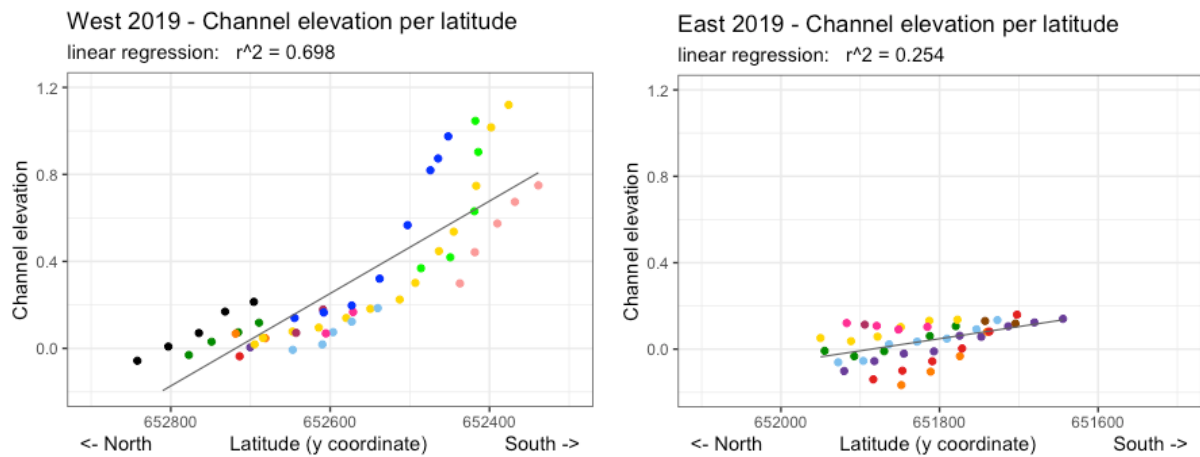


Figure 30. Channel elevation per latitude for West-2019 (left) and East-2019 (right).

4.2.2 Width, depth and area (along the channel and per latitude)

The width, depth, W:D ratio and area of the channels are plotted against the distance along the channel as well as against the latitudinal coordinates (figures 31, 32, 33, 33). Latitude is used to represent the cross-shore location, as the coast is roughly east-west oriented. Since most channels are directed from north to south, the plots give similar patterns as the plots along the channel distance. However, by using latitude, the meandering behaviour and sometimes alongshore direction of the channels is corrected for, and is now representative of the distance from the coastline. The graphs for channel geometry in West-2020 can be consulted in Appendix F. They show that most channels have disappeared, except the landward ends of channels 6, 10 and 11.

The graphs for width along channel and width over latitude (Figure 31) show that West-2019 has a range in width of 0.4 to 2.4 meters with an average of 1.3 m, whereas East-2019 has a larger range with values from 0.3 to 3.8 metres and an average of 1.5 m. In both sites, some channels become wider and some channels become narrower along the channel. Compared to latitude, the linear regression line of the width at West-2019 slightly decreases when going south (landward). For East-2019, this line shows an increasing trend going south. For both sites, the relation between the width and distance is not statistically significant.

For channel depth, East-2019 shows values until 0.14 and mostly below 0.1 m (average 0.06 m), whereas West-2019 has larger depths, with values until 0.3 meters (average 0.13 m). One exception the transect at $x=200$ m of channel 10, which is 0.46 meters deep (Figure 32a). The landward side of this channel is still present in West-2020, but with a reduced width (see Appendix F). For both West-2019 and East-2019, linear regression shows an increase in channel depth in southern direction (Figure 32cd). R^2 values are 0.164 and 0.15 respectively, so the trends are statistically not significant.

Combining the width and depth, their ratio ($\beta = w/d$) shows a decreasing trend at East-2019 and West-2019 (Figure 33cd), meaning they get relatively narrower and deeper going landward. Again, when following each channel separately, some channels increase and some channels decrease in W:D ratio when going landward. The range in values is very different. Values at West-2019 are between 4 and 50, with an average of 16. East-2019 has an average ratio of 30, with values between 13 and 67, and one extreme value of 97.

The channel areas increase with southern (landward) latitudes (Figure 34cd). At both sites, many channels first show an increase in area when going landward, followed by a decrease in area. This decrease can for some channels correspond to the upper end of the channel. At West-2019, the range in area's for the seaward side of the channels ($x = 40$ m) is 0-0.2 m^2 , which is much larger than at East-2019 where this seaward range is 0-0.09 (Figure 34a and b),.

4.2.3 Slope, elevation

The slope is calculated from the difference in channel bed elevation between the transect itself and the transect 40 meters in seaward direction. A positive slope indicates that the inland channel bed elevation is higher than that of the seaward transect (increasing elevation towards the coast). Figure 35 shows that most channels have a steeper slope when moving landward. With a slope range of -0.5 m/km to 2.25 m/km, East-2019 also includes some locations where the elevation becomes lower in landward direction. In total, 6 transects show a negative slope, these are the most seaward transects from channels 2, 6, and 8, and a transect halfway channel 3. In West-2019, slopes range between 0.4 and 5.5 m/km, except for one location with a negative slope of -0.4 m/km. The longest channel, number 6, shows a slope of 0.5 m/km at the seaward side, and this increases to ± 3 m/km at the landward side. Channels 10 and 11 also show a higher slope (and thus steeper elevation increase) on the landward side. On the other hand, channel 12 which is the easternmost channel, has a clear decreasing trend. Comparing the slope to the latitudinal position, both sites show steeper channel bed slopes land inwards (Figure 35c and d).

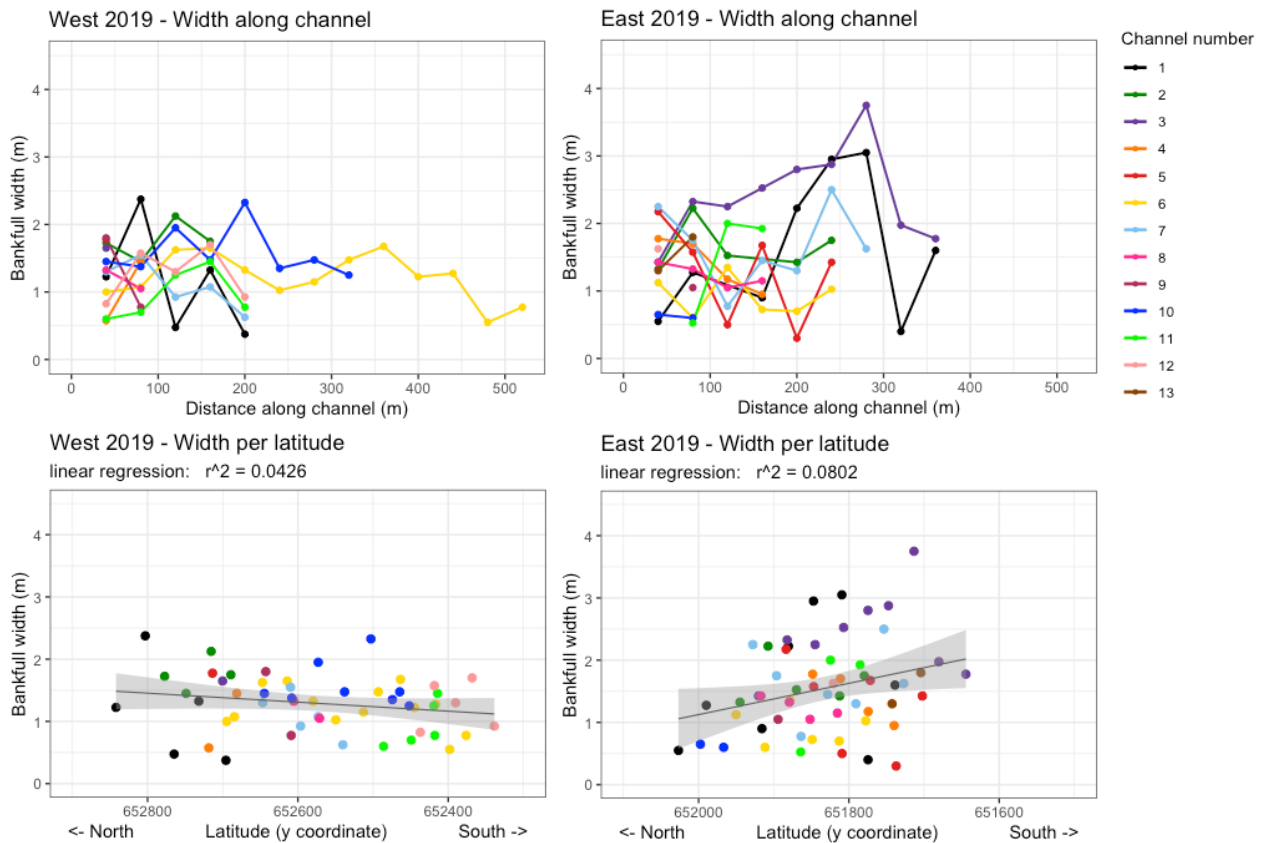


Figure 31. Channel width along channel distance (top) and per latitude (bottom) for West-2019 (left) and East-2019 (right)

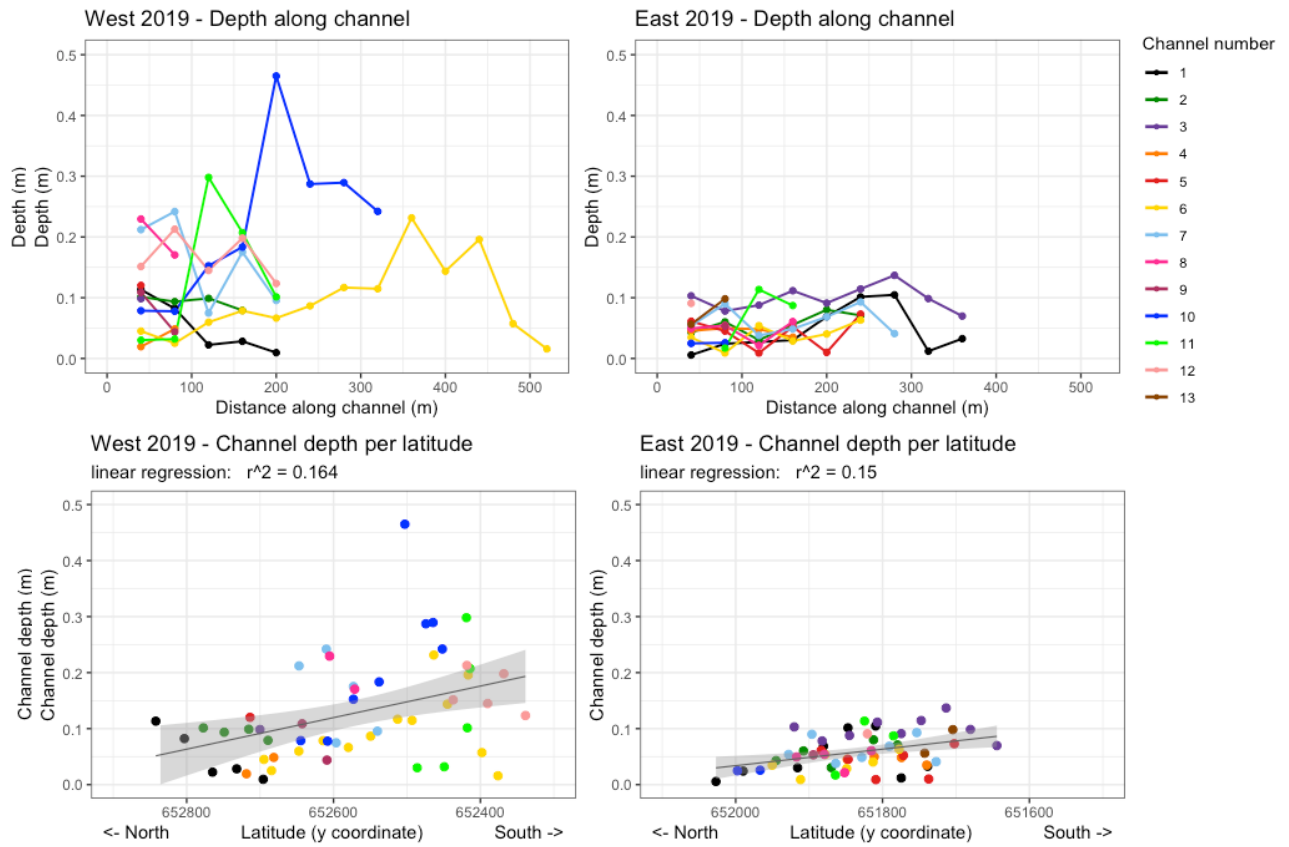


Figure 32. Channel depth along channel distance (top) and per latitude (bottom) for West-2019 (left) and East-2019 (right)

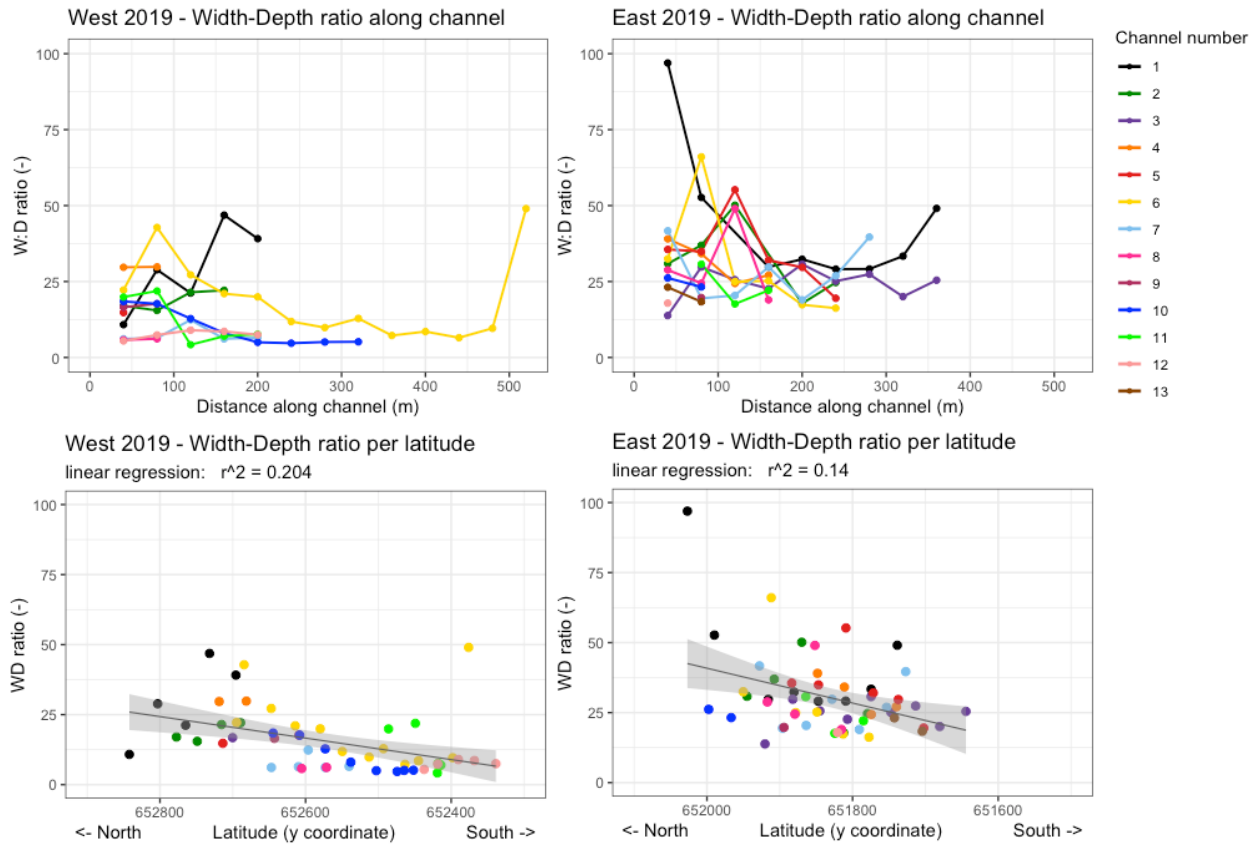


Figure 33. Channel width-to-depth ratio along channel distance (top) and per latitude (bottom) for West-2019 (left) and East-2019 (right)

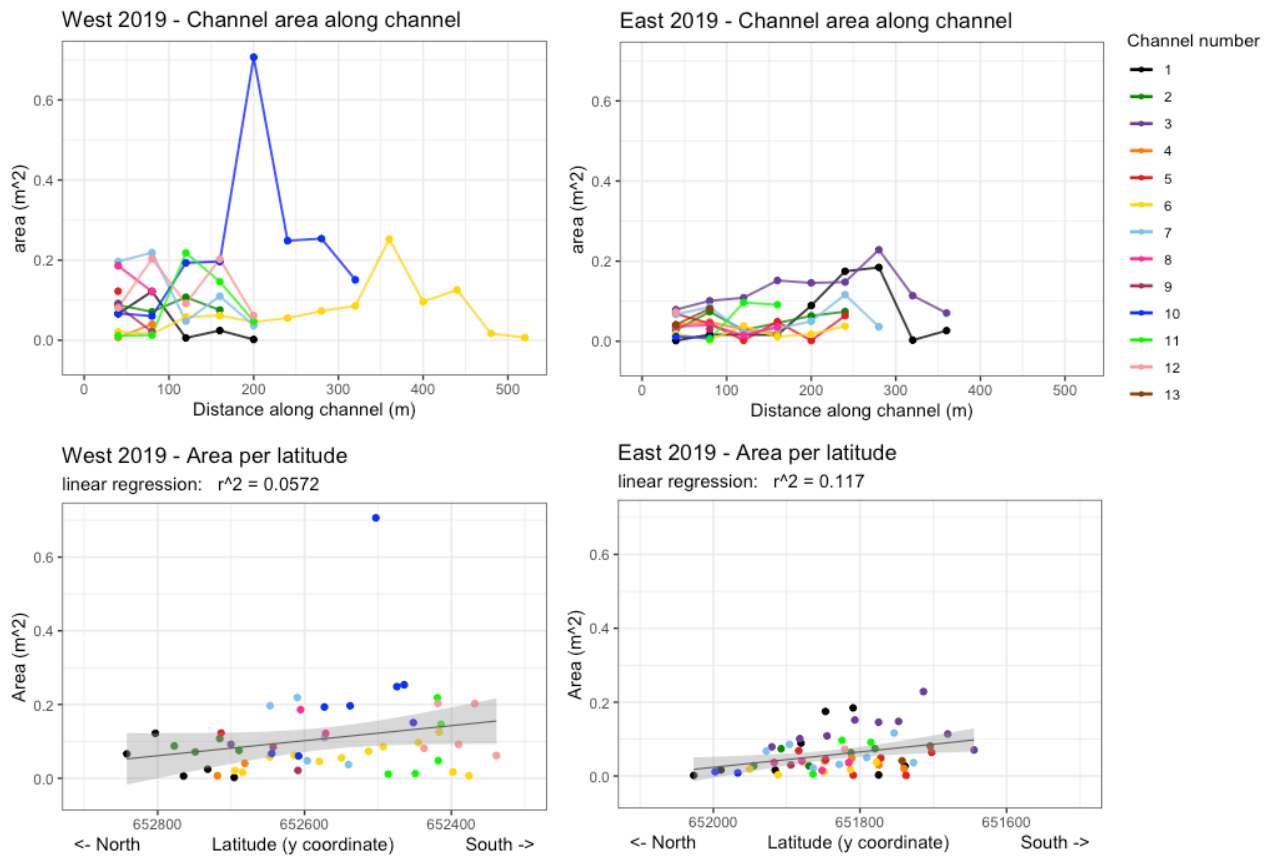


Figure 34. Channel area along channel distance (top) and per latitude (bottom) for West-2019 (left) and East-2019 (right)

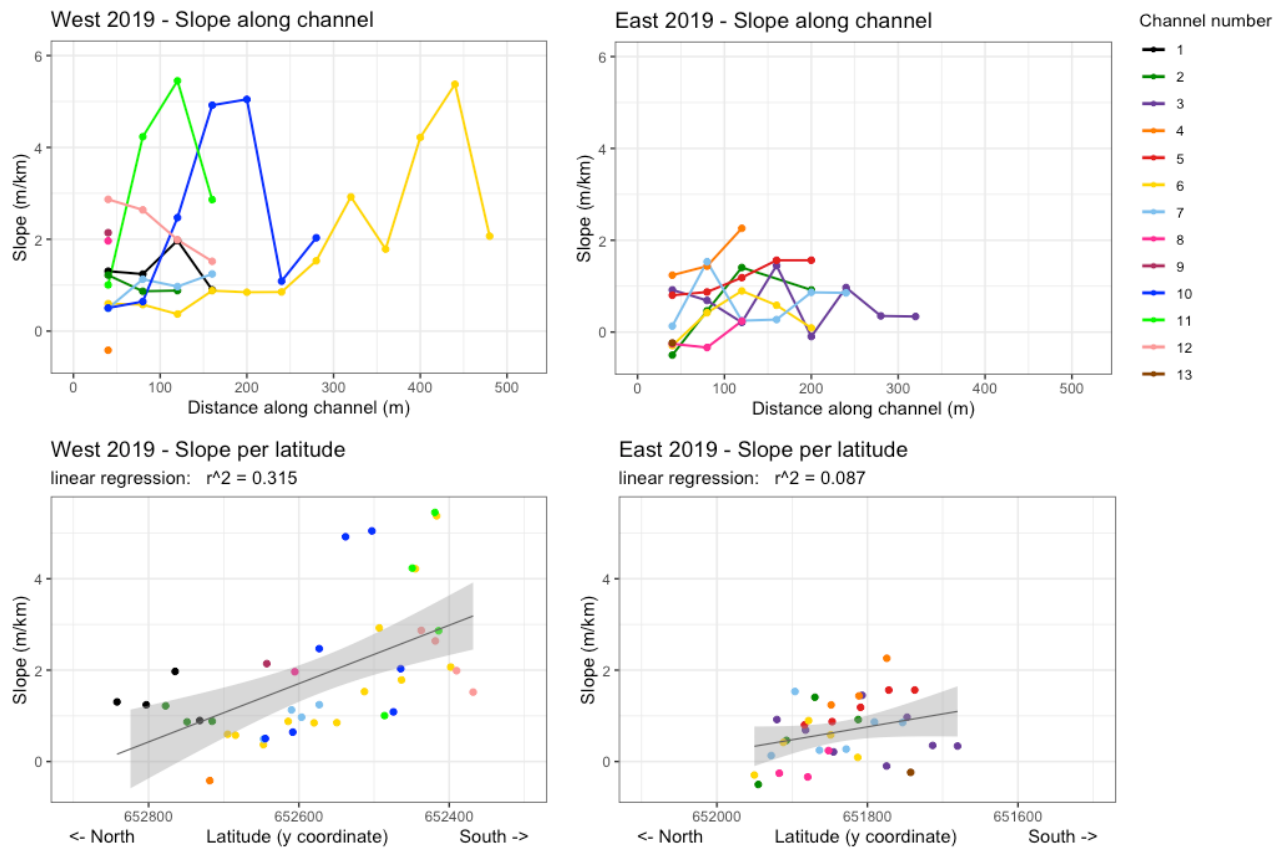


Figure 35. Channel bed slope along the channel distance (top) and per latitude (bottom) for West-2019 (left) and East-2019 (right)

4.3 Elevation differences in West-2019-2020

In Figure 36 it can be seen that the observed relative elevation differences are variable throughout the area. Close to the coast, numbers are small (mostly <0.06 m). Further seaward, numbers are ranging from 1.8 to an occasional observed decrease of -0.69 , however most measurements are between 0.2 and 0.9 meters of assumed sedimentation.

Broadly speaking, this agrees with some areas as shown in Figure 37. Apart from the doming that is clearly visible, the north-western side of this map shows values between 0 and 1.5m. However, on the coastal side, a decrease in elevation is suggested, between -1 and 0 m. On the whole, the map shows a trend in elevation change, ranging from -1 at the coast to $+1.5$ at the seaside (ignoring the doming area).

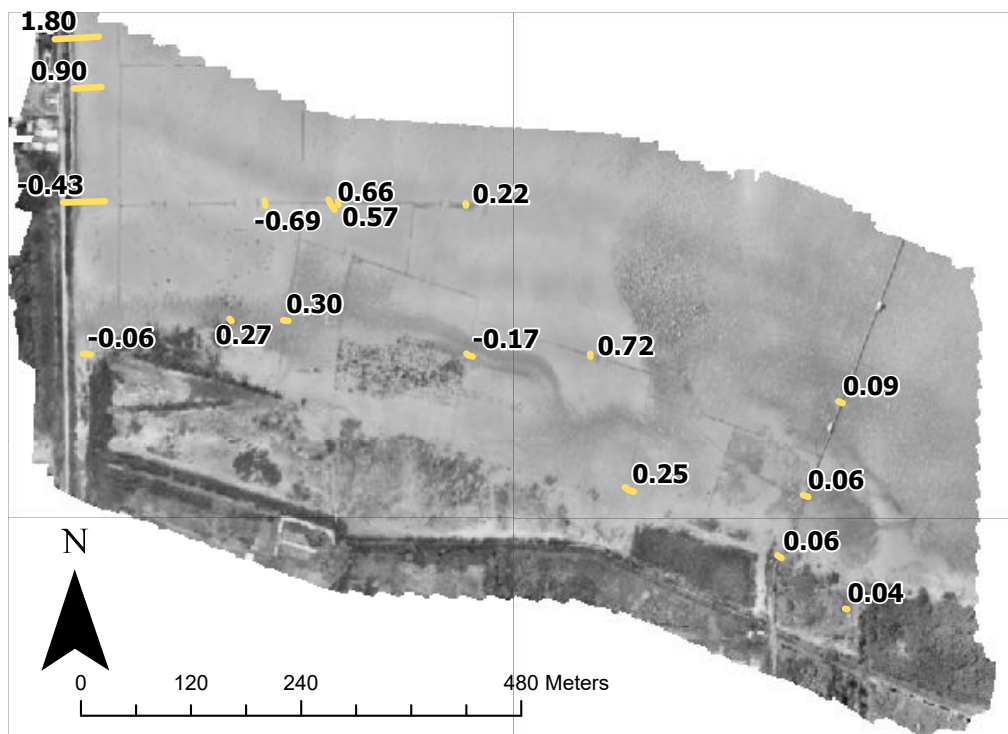


Figure 36. Relative change in sediment elevation between 2019 and 2020, compared to objects (dams, jetties, roads, etc.) that are considered of constant elevation.

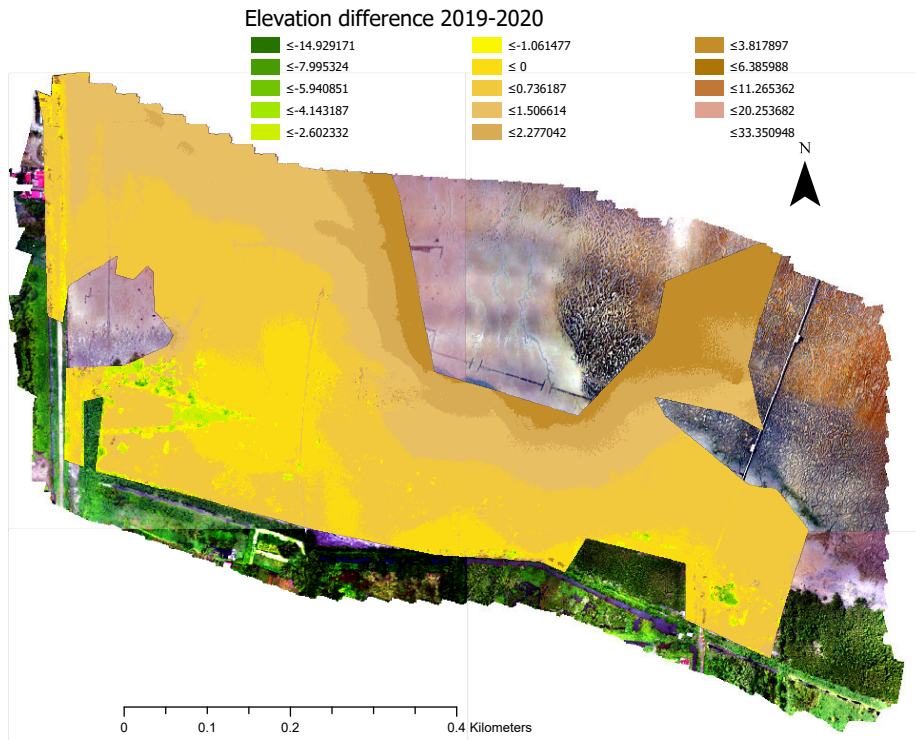


Figure 37. Elevation change between West-2019 and West-2020, derived from the DEMs of the two years. (Mean: 0.67m; Median: 0.55m). Background: orthophoto West-2019

5. Discussion

This thesis aimed at mapping coastal morphology at two selected study sites in Suriname, while at the same time assessing the potential of applying UAV imagery for coastal research. UAV imagery was collected and processed, resulting in orthophotos and DEMs of two study sites on the coast of Paramaribo. From that data, spatial patterns and temporal changes in channel geometry, vegetation cover and mudflat elevation were analysed. The suitability of the method was then examined.

The assessment of spatio-temporal patterns in mudflat elevation and channel geometry was limited by the quality and availability of multi-temporal data. Since UAV camera malfunctioning obstructed the processing of an orthophoto and DEM for East-2019, this study site could not be analysed for temporal changes. This malfunctioning also introduced error zones related to doming in the West-2020 DEM, partially eliminating the possibility of comparing the two DEMs. Despite this, relative changes in height, channel geometry and vegetation could still be assessed. Also, the orthophotos and DEMs of 2019 were of high accuracy and thus provided sufficient data for spatial comparisons.

5.1 Spatial differences

The processed DEMs (Figure 25, Figure 25, and Figure 26) allowed us to look at alongshore difference in elevation by comparing the two study sites in 2019 (East-2019 and West-2019). Simultaneously, the processed orthophotos facilitated the detection of (morphological) features such as channels and vegetation (Figure 20, Figure 21, and Figure 22). By combining these two datasets we could analyse spatial patterns in absolute elevation, channel network patterns, and channel geometries, compared to their cross-shore location and location along the coast.

The range in mud elevation on the tidal flats is $-0.25 - 1.5$ meters, mostly increasing in southern (landward) direction, corresponding to the downward sloping behaviour of intertidal flats. The eastern site has smaller range and lower elevations than the western site. West-2019 has an elevation range of about $-0.25 - 1.5$ meters (Figure 25). The average high-water line lies approximately halfway through the study area, recognized by the abrupt change in sediment colour and the increased slope. The line corresponds to a mudflat elevation of roughly $0.8-0.9$ m. Seaward of this line, mudflat elevations are below 0.8 and decrease when moving further north. Based on the orthophoto, this part of the mudflat is probably inundated during every high tide (\pm twice per day) below this line. Above this line, elevations are between 0.9 and 1.5 . The frequency of inundation in this area is unknown. Flooding is still assumed to occur during high spring tides, as channels continue landward and accumulated wood and dead plants indicate that maximum high water can reach the southern channel that is defining the boundary of the study area. East-2019 is more homogenous in elevation, the range in elevation is $-0.25 - 1$ meter (Figure 25). In general, the elevation decreases from ± 0.4 m in the southeast to ± -0.1 m in the north-east. There is an increase in north-west direction, which is assumed to be related to the observed doming. The average high-water line is at the edges of the mudflat defined by the dikes, and locally even more landward where the dike is no longer present. This becomes clear from morphological signs of regular inundation (channels, sediment colour, erosion pits) throughout the entire mudflat, and from the fact that the mudflat is below 0.9 , which is the height of the average high-water line at West-2019. These differences between east and west indicate that the shoreline is more vulnerable in the east, where it has no buffer zone with high (above high-water level) elevations, and therefore is directly in contact with the sea.

Channel network patterns are different for both locations and are suggesting more erosion in the east than in the west (Figure 19). At east-2019, channel network patterns are similar throughout the area. They are relatively straight, showing little (yet some) sinuous meandering. Most channels are parallel to each other, with a north-south orientation. According to Hughes (2011), this is a sign of an immature drainage pattern, common on tidal flats that are regularly impacted by storms, which “reset” the channels partially or totally. Furthermore they often coincide with lying dead wood. This can be caused by increased turbulence around the wood, creating a local depression which then fixates a passing channel. The other way around, the wood presumably has a north-south direction because it is moved by tidal currents. This direction parallel to the tidal currents creates the least friction and is therefore

the most stable orientation of the wood. At West-2019 site, the channels are more developed on the northeast section, forming a meandering dendritic network. This is the most common pattern on tidal flats (Hughes, 2011). Yet because of the significant dendritic pattern, joined channels form up to fifth order channels, something which is rare on tidal flats, as described in paragraph 2.3 (Hughes, 2011).

Vegetation is scarce at East-2019 (Figure 20), and more existent at the western site (Figure 21). As West-2019 has more areas of increased elevations (above $\pm 1\text{m}$), this provides more opportunities for vegetation to grow. Indeed, more (high) vegetation is present in the elevated areas of West-2019, especially compared to the East-2019 location. Close to the coast there are areas with stable mangrove patches, but even further towards the sea the mangrove rehabilitation patch still seems to get a foothold. East-2019 has only a small corner of vegetation, and this is mostly small shrubs rather than large mangroves or other trees. Vegetation is dying in East-2019: this becomes clear from the abundance of dead trees and dead wood spread throughout the area, which can be caused by relative drowning of the area, for example through sea level rise or local erosion, or loss of vegetation through deterioration of soil characteristics. Furthermore, the edges of the vegetation patch show signs of erosion by calving. A major contrast between East-2019 and West-2019 is therefore the status of the vegetation: in West-2019, vegetation is on the rise, whereas in East-2019, the last vegetation that is still left, might soon be gone.

The differences in channel patterns, elevation and vegetation all indicate stronger erosion in East-2019 than in West-2019. Possible causes for these alongshore differences are either differences in hydrodynamic environments, or recent human interventions. The location of the two study sites is different, which can cause a different hydrodynamic environment. Although the locations only lie 2.2 km apart, their location relative to the Suriname river mouth, Braampunt beach, and the mudbanks in front of the Suriname coast is significantly different (Figure 12). East-2019 is closer to the Suriname river mouth, so the jet flow of the river is assumed to have more impact on that study site. Although the study site is located on the leeward side of the dewatering channel levee, the flow of the river might cause higher flow velocities, hindering sedimentation. This can potentially increase the erosion that is suggested by the immature channel pattern (section 2.3 and Figure 19). The location of the study sites relative to the mudbanks is another optional explanation. The mudbank which is in front of the coast between the Coppename and Suriname rivers, is now located west of the study sites (Figure 13). Therefore, Weg naar Zee is on the trailing edge of this bank, causing increased erosion (Anthony et al., 2010). With East-2019 lying farther from the mudbank, local variation in trailing edge erosion processes might be a cause for increased erosion in East-2019.

Secondly, the difference in erosion between West-2019 and East-2019 might be caused by human interventions. Human interventions at West-2019 comprise the permeable dam pattern, and the planted mangrove trees (Figure 21). Both are aimed at trapping sediment, rather than completely blocking the sea. As the mean high-water line is 100-200 m seaward of the dike, it leaves a buffer zone where sediment can accumulate. East-2019 has no sediment trapping units on the mudflat itself, but the eastern and southern boundaries of the flat are all but pristine. Remnants of an old dam and dike are visible on the southern side, and the dewatering channel levee forms the boundary on the east, all within reach of the high tide (Figure 20). As a depression in elevation is observed in the DEM (Figure 25) in front of the remnants of the dam, it most likely refracts waves thus increasing turbulence and enhancing erosion. Thus, there is a big difference in human interventions. In East-2019, poorly maintained “hard” coastal defence structures have been implemented aiming to block the sea but with the side-effect of increasing erosion by wave refraction, as well as a decrease in functionality by deterioration of the structure. In West-2019, “soft” coastal defence methods are used to trigger accretion by making use of the sea.

Regardless of the processes leading erosion and deposition, the system can reach a tipping point. In a stable situation with little erosion, once steady mangrove vegetation is present sedimentation can potentially be further enhanced, allowing mangroves vegetation to expand. This seems to be the situation at West-2019. On the other hand, at East-2019, once there is no vegetation to break the wave energy and the bare mudflat reaches to the dike, waves are refracted and erosion is increased, which in turn inhibits any pioneer vegetation to settle, further decreasing sediment deposition.

The dataset created in this research suggests multiple relations between location and morphology. To test the representability of these relations for the Amazon coast, the analyses should be repeated on a larger scale. Furthermore, the possible causes for spatial variation in erosion as presented in this thesis, have to be researched individually to gain more understanding of which processes to keep in mind when attempting to tackle problems with coastal erosion. In particular, data should be collected on the local flow velocities in the different locations, to estimate flood, ebb, or wave dominance. Also, as sediment type and thereby erodibility has a large influence on channel morphology, it should be researched if local differences in sediment type along the coast of *Weg naar Zee* can explain the differences in channel network pattern and channel geometry. With this knowledge, we can better predict future coastal development, and determine suitable locations for erosion mitigation strategies.

5.2 Temporal differences

DEM's and orthophotos of the western site (June 2019 and February 2020) were compared to assess changes in morphology that happened in these 8 months. Comparison of the DEM's was done in two ways. For the area that was not impacted by errors, the difference between the DEM's was used. Yet for some areas, doming and additional zones with large errors obstructed the possibility using of simply subtracting the DEM's. Therefore, an additional analysis was done to derive relative elevation differences. The elevation of stable objects was measured as well as the sediment next to it. The difference between the two years was assumed to be sedimentation or erosion (paragraph 3.6). As there were large differences in estimated local elevation differences, the individual measurements are not considered accurate, but rather, an average change in elevation was estimated for different regions in the study area, based on combined measurements.

These integrated results showed that the elevation has increased significantly between 2019 and 2020 (paragraph 4.3). It was estimated that ± 0.3 to 0.5 m of sediment has been deposited on the north-western region of this western study site. This is supported by the observation of filled channels with sediment from the orthomosaics (Figure 21, Figure 22) and transect profiles (Appendix F). The seaside showed channels that were clearly visible in 2019, while no channels are observed in that area in 2020.

The channel network pattern has remained very similar on the landward, higher elevated sections that are visible in both the West-2019 and West-2020 DEM and orthophotos. The other two defined classes (beige sediment with medium relief and meandering dendritic channel pattern, and brown sediment with high relief and complex channel pattern, see Figure 21) are in 2020 covered with a layer of sediment. There, only a few single channels are observed. The outer (orange) section of 2019 has high relief but no clear channel network.

The orthophotos of 2019 and 2020 show several changes in vegetation that happened in the 8-month period. The event or phase of fresh sediment supply has also taken down some of the trees in the west (Figure 23b). At the mangrove regeneration patch, some of the young trees have grown significantly - especially in the middle and seaward part of the western half. Also, some trees in this planted patch have disappeared, those were mainly the trees that were still small in 2019 (Figure 23c). The shoreward patches on the south-east remain stable, as do most of the smaller isolated patches on the landward side (Figure 21, Figure 22). As discussed in section 2.2.1, one of the conceptual models describing mudbanks is one where the mudbank is disconnected from the coast, leaving an intertidal area between the mudbank and the coast (Allison and Lee, 2004). During flood, sediment is driven shoreward over the mudbank, and the intertidal area is filled (Toorman et al., 2018). This could be an explanation for the sediment supply which happened between 2019 and 2020. In that case, it would suggest that a new mudbank is approaching the study area at *Weg naar Zee*. It is likely that the permeable dams have enhanced the settling of this sediment by reducing flow velocities. Although the sediment trapping units are too small-scale to have an impact on the increased supply of the sediment, they do help turning it into deposition.

5.3 Channel geometry

The analysis of channel geometry was limited by a number of factors. Still, relations between the location and geometry of channels could still be observed. It therefore shows that channel geometry patterns are very relevant for future research, and this method should be repeated for longer time scales and multiple alongshore locations at the coast. In the future research, the following improvements can be implemented compared to the method in this thesis. Firstly, the placement of the transects is important. As they were created with a strict interval on a manually drawn channel polyline, some were not exactly perpendicular to the channel, distorting the measurements for channel width. Also, some were located next to dead wood lying in the channel, or at a bifurcation point. These locations are therefore not representative for the channel parameters. Therefore, individual adjustment of the transects is necessary. Furthermore, the alongshore and cross-shore location of the transects was approximated by taking the latitudinal and longitudinal coordinates, however the coastline runs slightly east-south-east to west-northwest, so this was not an optimal representation. For improvement, it should be attempted to plot the channel geometries over their distance either relative to the coastline to show the true cross-shore location, or relative to the average high-tidal elevation to see the relation between geometry and inundation time.

The analysis on channel transects (section 4.2) suggested spatial differences in channel geometry between our two study sites. In both sites, channels are deeper near the coast, although a larger range in depths was observed in West-2019 (0 - 0.3) compared to East-2019 (0 - 0.15) (see Figure 32). The opposite was true for width of the channels, which was 0.4 - 2.3 m in West-2019, compared to 0.3 - 4 m in East-2019. The average width-to-depth ratio (β) is therefore also higher in East-2019 than in West-2019, and decreases towards the coast. According to Hughes et al. (2011) sediment that is easily eroded tends to form wider, shallower channels (paragraph 2.3). This is in line with the imagery observations suggesting stronger erosion in East-2019. As Marani et al. (2002) stated, tidal channels usually have a width-to-depth ratio of $8 < \beta < 50$ (Figure 9). Although their measurements were based on larger tidal channels (depths of 1-10 m and widths of 10 – 300 m) than the channels in this study, the average width-to-depth ratios fall within the expected range. On average, West-2019 had an average of 16, and East-2019 had an average of 30. However not all transects were within this interval. In West-2019, 18 of the 53 transects had β -values below 8, and none above 50. In East, only 4 out of the 58 transects showed values above 50, and none below 8.

When looking at elevation (Figure 30) and slope (Figure 35) of the channels, West-2019 has a concave-up profile. This suggests that wave energy is dominant, and that net sediment transport is directed seaward, causing erosion (Figure 7) (Friedrichs, 2012). However, as has become clear from the DEM-comparison of West-2019 and 2020, this area seems to be increasing in elevation rather than eroding. Multiple explanations are possible for this contradiction. Firstly, the interventions – mangrove regeneration and sediment trapping units – might counter the previous erosive nature of this area. As these are only implemented since 2015, the mudflat profile might not yet be adjusted to the new circumstances. Secondly, the accretion that happened between June 2019 and February 2020 might have been a single deposition event, where the normal conditions favour erosion. To determine which factors can explain the contradiction between the mudflat profile and the deposition visible in the DEM's, a longer time series is necessary.

For East-2019, the trendline for the slope per latitude also suggests an increase in landward direction. Nevertheless, this linear fit is statistically insignificant, and the elevation per latitude (Figure 30) does not show a clear concave pattern. The elevation along the channel (Figure 28) shows some channels with a linear profile, and some channels with a concave profile. To define the coastal profile type, cross-shore transects should be taken from the East-2019-DEM, which can discriminate between profile type. Based on the various properties indicating erosion, a concave-up profile is expected.

5.4 Potential of UAV research for coastal regions

This research assessed the use of UAVs for coastal research by testing the applicability in various ways. Essentially, the technique provides RGB and elevation data with very high resolution, a flexible timing of data collection, and a large spatial extent. Interpreting the orthophotos visually – as was done in this thesis - is a suitable way of gaining a general understanding of an area and to find large-scale patterns in vegetation and channel network patterns. For more objective and scalable analysis of orthophotos, the use of automated pixel or object classifications is needed. UAV derived DEMs also have multiple applications. It provides data on large scale mudflat elevation, and it therefore has the potential to be used in automated erosion and accretion calculation when used in time-series. In combination with orthophoto interpretation, the DEM also gives information on individual units like artificial structures, vegetation and erosion pits. Furthermore, the possibility of performing flow direction analysis could serve as a way to automatically identify channels, with which it would be possible to compute the total channel volume in an area. UAV can also provide data types that were not used in this project such as point clouds. Point clouds can be used to estimate above ground biomass of vegetation (Wallace et al., 2016), so this gives the opportunity to monitor the development of (planted) mangrove vegetation.

The variety in potential of UAV methods is very dependent on the accuracy and resolution of the data. In this study, it became clear that ground control points (GCP's) need to be spread around and throughout the whole study area to get usable DEMs, which is challenging on tidal mudflats. Furthermore, the timing of image acquisition should be aimed to be at the lowest tide possible, to minimize the presence of water bodies on the mudflat which can disturb the processing of the point cloud. In line with this, UAVs should be flown with sufficient daylight, yet with little direct sunlight which can reflect on the water, also disturbing image processing. However, when the quality of the DEM is high, the data is extremely useful for small-scale as well as large-scale observations and measurements.

6. Conclusion

In this research, spatial and temporal patterns in coastal morphology of a large tidal mudflat were mapped, located on the Amazon coast. This is a unique wave dominated system with high mud supplies. Understanding the local and temporal variation in morphology can help us mitigate erosion at locations where it is needed most. Furthermore, the potential of UAV imagery in coastal research is examined.

Using UAV derived orthophotos and DEMs, two study sites were analysed that were located 2.2 km apart on a tidal flat west of the Suriname river mouth. It was found that already this small alongshore distance, a large variation in morphology and elevation is present. The western site - farthest from the river - has a larger elevation range, including a larger area above 1 m of elevation, which explains why more stable vegetation patches are present compared to the eastern site. This also creates a buffer zone between the mainland dike and the average high-water line, whereas this high-water line reaches all the way up to the dike in the eastern site. Other alongshore patterns that were found are straighter channels and reduced channel bed slopes towards the east. In general, more signs of erosion were seen in the eastern study site than in the western site. Considering human interventions, the two sites differ greatly. In the eastern area it has been attempted to develop hard coastal defence structures in the form of a dike and an adjacent dam, however these have largely deteriorated, and increased erosion is observed around the dam remnants due to the exposure to high tidal water. In the west, permeable dams are built to increase sedimentation, and a mangrove rehabilitation project is in place for which new mangrove trees are planted.

By deriving channel geometry from the DEMs, cross-shore trends in channel geometry were found, showing an increased channel depth and decreased width-to-depth ratio towards the coast for both study sites. The western has a concave-up profile, which suggests wave dominance and flood dominance, and thus an eroding coast, yet the morphological analysis shows signs of accretion. Oppositely, an erosive, concave-up profile was expected for the eastern site, yet this site showed a profile that was more linear.

For temporal changes, the data was compared over an 8-month period. This showed that significant sedimentation has occurred in the seaward side of the western study area, which is estimated to have caused a 0.5 meter increase in mudflat elevation. Future research aimed at pairing the local hydrodynamics to presence of mud banks and sediment trapping units could explain the processes evoking this accretion phase.

This thesis has shown that UAV research has the potential to provide detailed data on coastal morphology. Provided the data is of high resolution and high accuracy, UAV's can create datasets with a large spatial extent, with high flexibility of timing, for areas that are otherwise inaccessible. From the imagery used in this research, orthophotos and DEM's were created. Orthophotos have demonstrated to be suitable for visual interpretation of different morphological data such as recognizing vegetation, channel patterns, sediment colouring and artificial objects. In further research, they have the potential to be classified and analysed automatically based on pixel value or through object-based image analysis. UAV derived DEMs have proven to be a useful tool for assessment of large-scale mudflat elevation as well as for detailed measurements of channel geometry. They provide possibilities for automated monitoring of coastal erosion and sedimentation.

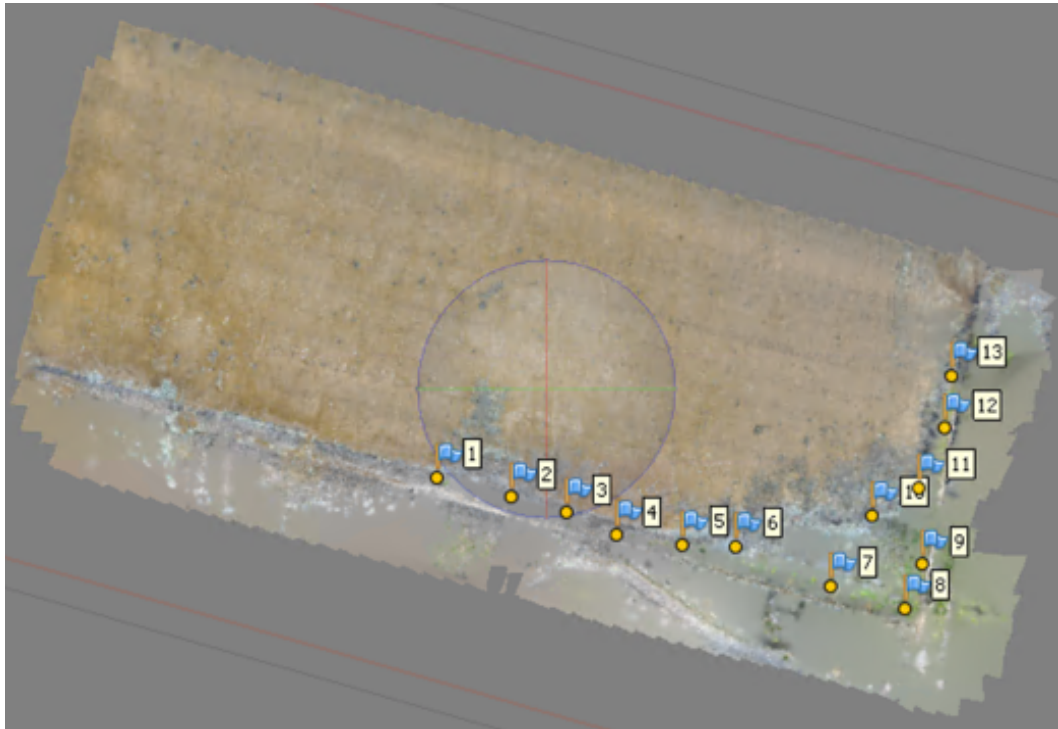
References

- Adam, E., Mutanga, O., & Rugege, D. (2010). Multispectral and hyperspectral remote sensing for identification and mapping of wetland vegetation: A review. *Wetlands Ecology and Management*, 18(3), 281–296. <https://doi.org/10.1007/s11273-009-9169-z>
- Alesheikh, A. A., Ghorbanali, A., & Nouri, N. (2007). Coastline change detection using remote sensing. *International Journal of Environmental Science and Technology*, 4(1), 61–66. <https://doi.org/10.1007/BF03325962>
- Allison, M. A., & Lee, M. T. (2004). Sediment exchange between Amazon mudbanks and shore-fringing mangroves in French Guiana. *Marine Geology*, 208(2–4), 169–190. <https://doi.org/10.1016/j.margeo.2004.04.026>
- Allison, M. A., Lee, M. T., Ogston, A. S., & Aller, R. C. (2000). Origin of Amazon mudbanks along the northeastern coast of South America. *Marine Geology*, 163(1–4), 241–256. [https://doi.org/10.1016/S0025-3227\(99\)00120-6](https://doi.org/10.1016/S0025-3227(99)00120-6)
- Alongi, D. M. (2002). Present state and future of the world's mangrove forests. *Environmental Conservation*, 29(3), 331–349. <https://doi.org/10.1017/S0376892902000231>
- Anthony, E. J. (2016). *Impacts of sand mining on beaches in Suriname. February*.
- Anthony, E. J., Brunier, G., Gardel, A., & Hiwat, M. (2019). Chenier morphodynamics on the amazon-influenced coast of suriname, South America: Implications for beach ecosystem services. *Frontiers in Earth Science*, 7(March), 1–20. <https://doi.org/10.3389/feart.2019.00035>
- Anthony, E. J., Gardel, A., & Gratiot, N. (2014). Fluvial sediment supply, mud banks, cheniers and the morphodynamics of the coast of South America between the Amazon and Orinoco river mouths. *Geological Society Special Publication*, 388(1), 533–560. <https://doi.org/10.1144/SP388.8>
- Anthony, E. J., Gardel, A., Gratiot, N., Proisy, C., Allison, M. A., Dolique, F., & Fromard, F. (2010). The Amazon-influenced muddy coast of South America: A review of mud-bank-shoreline interactions. *Earth-Science Reviews*, 103(3–4), 99–121. <https://doi.org/10.1016/j.earscirev.2010.09.008>
- Augustinus, P. G. E. F. (2004). The influence of the trade winds on the coastal development of the Guianas at various scale levels: A synthesis. *Marine Geology*, 208(2–4), 145–151. <https://doi.org/10.1016/j.margeo.2004.04.007>
- Berrenstein, H. J. (2010). *Coastal changes along the Suriname coast with emphasis on the changing coastline of Coronie from 1914 to 2007 and its influence on Avicennia germinans L. (Avicenniaceae)*. 580535(1), 86–95.
- Besset, M., Anthony, E. J., & Bouchette, F. (2019). Multi-decadal variations in delta shorelines and their relationship to river sediment supply: An assessment and review. In *Earth-Science Reviews* (Vol. 193, pp. 199–219). Elsevier B.V. <https://doi.org/10.1016/j.earscirev.2019.04.018>
- Bourret, A., Devenon, J. L., & Chevalier, C. (2008). Tidal influence on the hydrodynamics of the French Guiana continental shelf. *Continental Shelf Research*, 28(7), 951–961. <https://doi.org/10.1016/j.csr.2008.01.008>
- Cao, J., Leng, W., Liu, K., Liu, L., He, Z., & Zhu, Y. (2018). Object-Based mangrove species classification using unmanned aerial vehicle hyperspectral images and digital surface models. *Remote Sensing*, 10(1). <https://doi.org/10.3390/rs10010089>
- Casella, E., Rovere, A., Pedroncini, A., Stark, C. P., Casella, M., Ferrari, M., & Firpo, M. (2016). Drones as tools for monitoring beach topography changes in the Ligurian Sea (NW Mediterranean). *Geo-Marine Letters*, 36(2), 151–163. <https://doi.org/10.1007/s00367-016-0435-9>
- Cete., C., Haage, S., Hardwarsing, V., Kalloe, S., & Ma-ajong, A. (2018). *Mangrove Project Suriname (Master's thesis)*. Delft University of Technology, Netherlands.
- Chevalier, C., Baklouti, M., & Ramamonjjarisoa, A. (2004). Modeling the influence of wind and rivers on current, salinity and temperature over the French Guiana continental shelf during the rainy season. *Journal of Coastal Research*, 20(4), 1183–1197. <https://doi.org/10.2112/03-0059r.1>
- Dalrymple, R. W., & Choi, K. (1978). Sediment transport by tides. In *Middleton G.V., Church M.J.*,

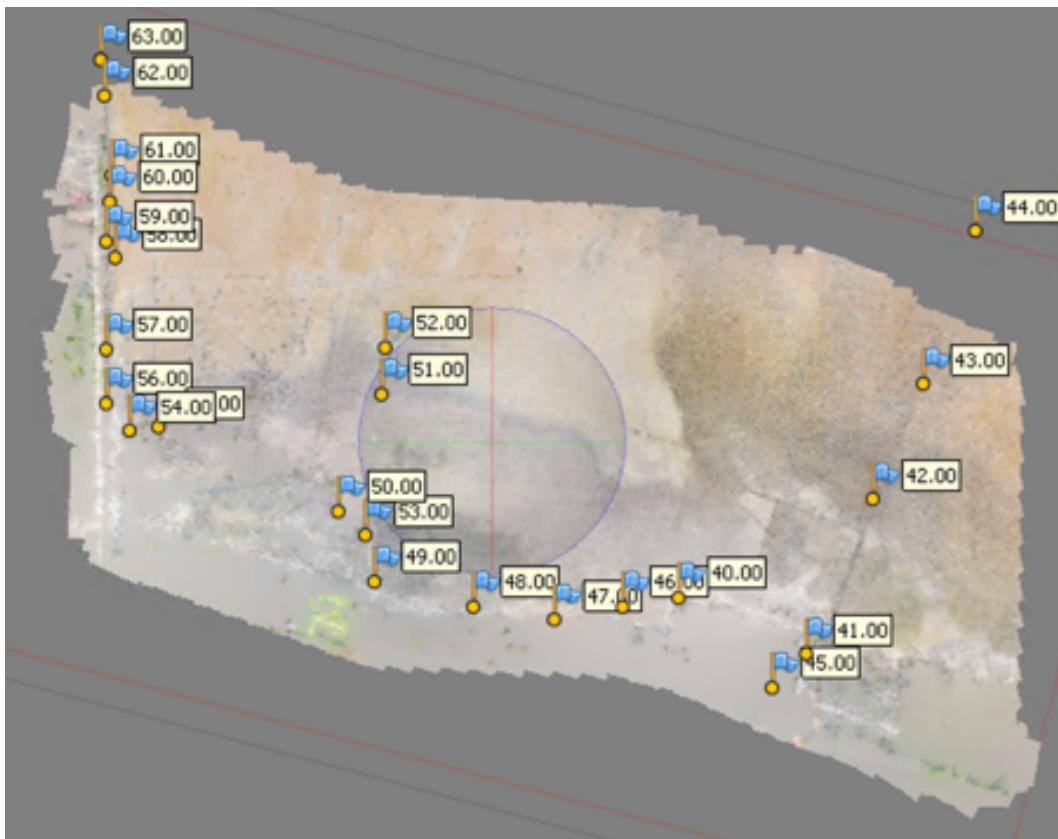
- Coniglio M., Hardie L.A., Longstaffe F.J. (eds) *Encyclopedia of Sediments and Sedimentary Rocks*. (pp. 606–609). Springer, Dordrecht. https://doi.org/10.1007/978-1-4020-3609-5_232
- De Jong, S. M., Shen, Y., De Vries, J., Bijnaar, G., Maanen, B. van, Augustinus, P., & Verweij, P. (2021). Mapping mangrove dynamics and colonization patterns at the Suriname coast using historic satellite data and the LandTrendr algorithm. *International Journal of Applied Earth Observation and Geoinformation*, 97(November 2020), 102293. <https://doi.org/10.1016/j.jag.2020.102293>
- de Vries, J., van Maanen, B., Ruessink, G., Verweij, P. A., & de Jong, S. M. (2021). Unmixing water and mud: Characterizing diffuse boundaries of subtidal mud banks from individual satellite observations. *International Journal of Applied Earth Observation and Geoinformation*, 95(October 2020), 102252. <https://doi.org/10.1016/j.jag.2020.102252>
- Deppe, F. (1999). *Intertidal Mudflats Worldwide Practical Course*. September, 99.
- Doughty, C. L., & Cavanaugh, K. C. (2019). Mapping coastal wetland biomass from high resolution unmanned aerial vehicle (UAV) imagery. *Remote Sensing*, 11(5). <https://doi.org/10.3390/rs11050540>
- Eisma. (1998). Intertidal deposits: river mouths tidal flats & coastal lagoons. *CRC Press, New York*. [https://books.google.nl/books?hl=nl&lr=&id=KurON0CEzPAC&oi=fnd&pg=PP15&dq=Eisma+D+\(1998\)+Intertidal+deposits:+river+mouths+tidal+fl+ats+%26+coastal+lagoons.+CRC+Pres+s,+New+York+Escoffi&ots=ii8JfihDsJ&sig=3kJXRrn73XK8fIPvtkW8IUTdI5c&redir_esc=y#v=onepage&q](https://books.google.nl/books?hl=nl&lr=&id=KurON0CEzPAC&oi=fnd&pg=PP15&dq=Eisma+D+(1998)+Intertidal+deposits:+river+mouths+tidal+fl+ats+%26+coastal+lagoons.+CRC+Pres+s,+New+York+Escoffi&ots=ii8JfihDsJ&sig=3kJXRrn73XK8fIPvtkW8IUTdI5c&redir_esc=y#v=onepage&q)
- Fagherazzi, S., & Furbish, D. J. (2001). On the shape and widening of salt marsh creeks. *Journal of Geophysical Research: Oceans*, 106(C1), 991–1003. <https://doi.org/10.1029/1999JC000115>
- Friedrichs, C. T. (2012). Tidal Flat Morphodynamics: A Synthesis. In *Treatise on Estuarine and Coastal Science* (Vol. 3, Issue January 2011). Elsevier Inc. <https://doi.org/10.1016/B978-0-12-374711-2.00307-7>
- Gratiot, N., Gardel, A., & Anthony, E. J. (2007). Trade-wind waves and mud dynamics on the French Guiana coast, South America: Input from ERA-40 wave data and field investigations. *Marine Geology*, 236(1–2), 15–26. <https://doi.org/10.1016/j.margeo.2006.09.013>
- Hibma, A., Stive, M. J. F., & Wang, Z. B. (2004). Estuarine morphodynamics. *Coastal Engineering*, 51(8–9), 765–778. <https://doi.org/10.1016/j.coastaleng.2004.07.008>
- Hughes, Z. (2011). Tidal Channels on Tidal Flats and Marshes. In *Principles of Tidal Sedimentology* (pp. 269–300). <https://doi.org/10.1007/978-94-007-0123-6>
- IPCC. (2014). Climate Change 2014: Synthesis Report. Contribution of Working Groups I, II and III to the Fifth Assessment Report of the Intergovernmental Panel on Climate Change. In Core Writing Team, R. K. Pachauri, & L. A. Meyer (Eds.), *IPCC*.
- Lovelock, C. E., Cahoon, D. R., Friess, D. A., Guntenspergen, G. R., Krauss, K. W., Reef, R., Rogers, K., Saunders, M. L., Sidik, F., Swales, A., Saintilan, N., Thuyen, L. X., & Triet, T. (2015). The vulnerability of Indo-Pacific mangrove forests to sea-level rise. *Nature*, 526(7574), 559–563. <https://doi.org/10.1038/nature15538>
- Marani, M., Lanzoni, S., Zandolin, D., Seminara, G., & Rinaldo, A. (2002). Tidal meanders. *Water Resources Research*, 38(11), 7-1-7–14. <https://doi.org/10.1029/2001wr000404>
- Marshak, S. (2015). Restless Realm: Oceans and Coasts. In Eric Svendsen (Ed.), *Earth: Portrait of a planet* (5th ed., pp. 655–693). W. W. Norton & Company, Inc.
- Navarro, A., Young, M., Allan, B., Carnell, P., Macreadie, P., & Ierodiaconou, D. (2020). The application of Unmanned Aerial Vehicles (UAVs) to estimate above-ground biomass of mangrove ecosystems. *Remote Sensing of Environment*, 242(November 2019), 111747. <https://doi.org/10.1016/j.rse.2020.111747>
- Neumann, B., Vafeidis, A. T., Zimmermann, J., & Nicholls, R. J. (2015). Future coastal population growth and exposure to sea-level rise and coastal flooding - A global assessment. *PLoS ONE*, 10(3). <https://doi.org/10.1371/journal.pone.0118571>
- Proisy, C., Gratiot, N., Anthony, E. J., Gardel, A., Fromard, F., & Heuret, P. (2009). Mud bank colonization by opportunistic mangroves: A case study from French Guiana using lidar data. *Continental Shelf Research*, 29(3), 632–641. <https://doi.org/10.1016/j.csr.2008.09.017>
- Pye, K., & French, P. (1993). *Erosion and accretion processes on British Salt Marshes. Vol 1 Intr*(Cambridge Environmental Research Consultants, Cambridge).

- Roberts, A. M. 2017. "Effect of Heinrich Events on Ocean Circulation and Sediment Input on the Nordeste Brazilian Continental Margin." University of Southampton.
- Seyler, P., Guyot, J.-L., Elbaz-Poulichet, F., Filizola Jr., N. P., & Boaventura, G. (1998). Hydrological control on the temporal variability of trace element concentrations in the Amazon River. *Mineralogical Magazine*, 62A(1–3), 423–424.
- Toorman, E. A., Anthony, E., Augustinus, P. G. E. F., Gardel, A., Gratiot, N., Homenauth, O., Huybrechts, N., Monbaliu, J., Moseley, K., & Naipal, S. (2018). Interaction of mangroves, coastal hydrodynamics, and morphodynamics along the coastal fringes of the Guianas. In *Coastal Research Library* (Vol. 25). https://doi.org/10.1007/978-3-319-73016-5_20
- United Nations. (2017). The Ocean Conference. Fact sheet: People and Oceans. In *UN Conference, New York, 5-9 June 2017* (Vol. 6, Issue 1). <https://www.un.org/sustainabledevelopment/wp-content/uploads/2017/05/Ocean-fact-sheet-package.pdf>
- Van Veen, J., Van Der Spek, A. J. F., Stive, M. J. F., & Zitman, T. (2005). Ebb and flood channel systems in the Netherlands Tidal Waters. *Journal of Coastal Research*, 21(6), 1107–1120. <https://doi.org/10.2112/04-0394.1>
- Walcker, R., Anthony, E. J., Cassou, C., Aller, R. C., Gardel, A., Proisy, C., Martinez, J. M., & Fromard, F. (2015). Fluctuations in the extent of mangroves driven by multi-decadal changes in North Atlantic waves. *Journal of Biogeography*, 42(11), 2209–2219. <https://doi.org/10.1111/jbi.12580>
- Wallace, Luke et al. 2016. "Assessment of Forest Structure Using Two UAV Techniques: A Comparison of Airborne Laser Scanning and Structure from Motion (SfM) Point Clouds." *Forests* 7(3): 1–16.
- Wetlands International. (2016, June 14). *Building with Nature concept successfully introduced in Suriname* (E. Van Lavieren (ed.)). Wetlands International. <https://www.wetlands.org/blog/building-with-nature-concept-successfully-introduced-in-suriname/>
- Woodroffe, C. D., Lovelock, C. E., & Rogers, K. (2014). Mangrove Shorelines. In G. Masselink & R. Gehrels (Eds.), *Coastal environments and global change*. John Wiley & Sons, Ltd.
- Wright, L. D., & Nittrouer, C. A. (1995). Dispersal of river sediments in coastal seas: Six contrasting cases. *Estuaries*, 18(3), 494–508. <https://doi.org/10.2307/1352367>
- Yallop, M. L., De Winder, B., Paterson, D. M., & Stal, L. J. (1994). Comparative structure, primary production and biogenic stabilization of cohesive and non-cohesive marine sediments inhabited by microphytobenthos. *Estuarine, Coastal and Shelf Science*, 39(6), 565–582. [https://doi.org/10.1016/S0272-7714\(06\)80010-7](https://doi.org/10.1016/S0272-7714(06)80010-7)
- Yin, D., & Wang, L. (2019). Individual mangrove tree measurement using UAV-based LiDAR data: Possibilities and challenges. *Remote Sensing of Environment*, 223(January), 34–49. <https://doi.org/10.1016/j.rse.2018.12.034>
- Zhu, X., Hou, Y., Weng, Q., & Chen, L. (2019). Integrating UAV optical imagery and LiDAR data for assessing the spatial relationship between mangrove and inundation across a subtropical estuarine wetland. *ISPRS Journal of Photogrammetry and Remote Sensing*, 149(January), 146–156. <https://doi.org/10.1016/j.isprsjprs.2019.01.021>

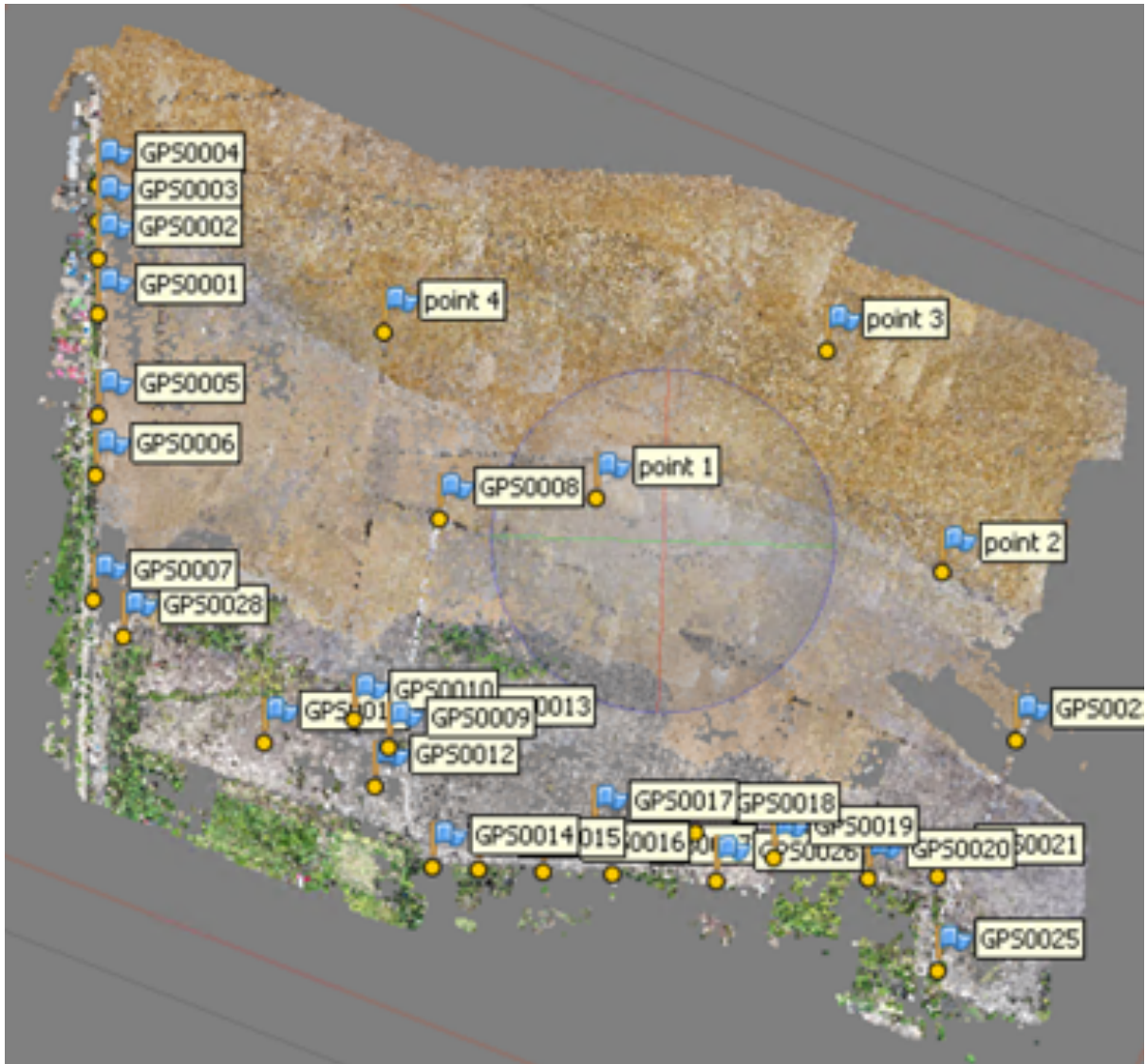
Appendix A - Location of ground control points



East-2019

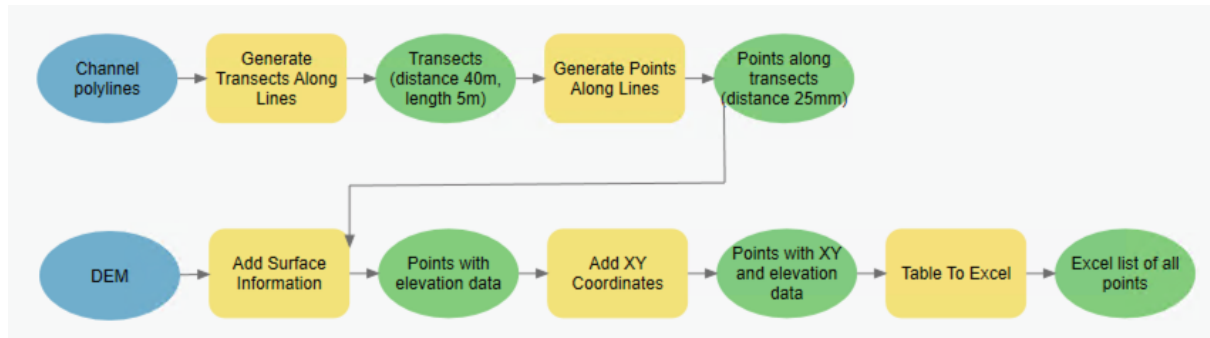


West-2019

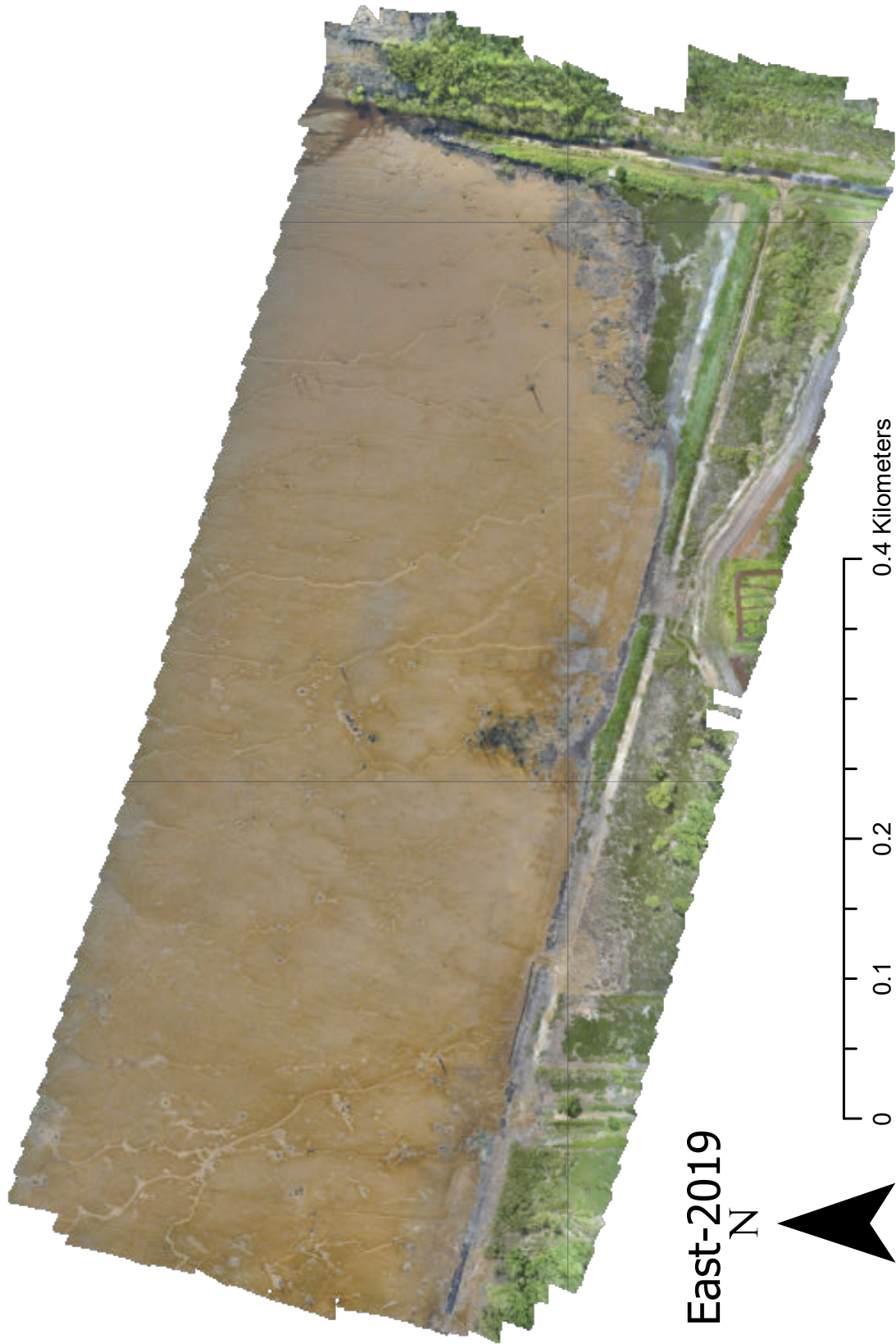


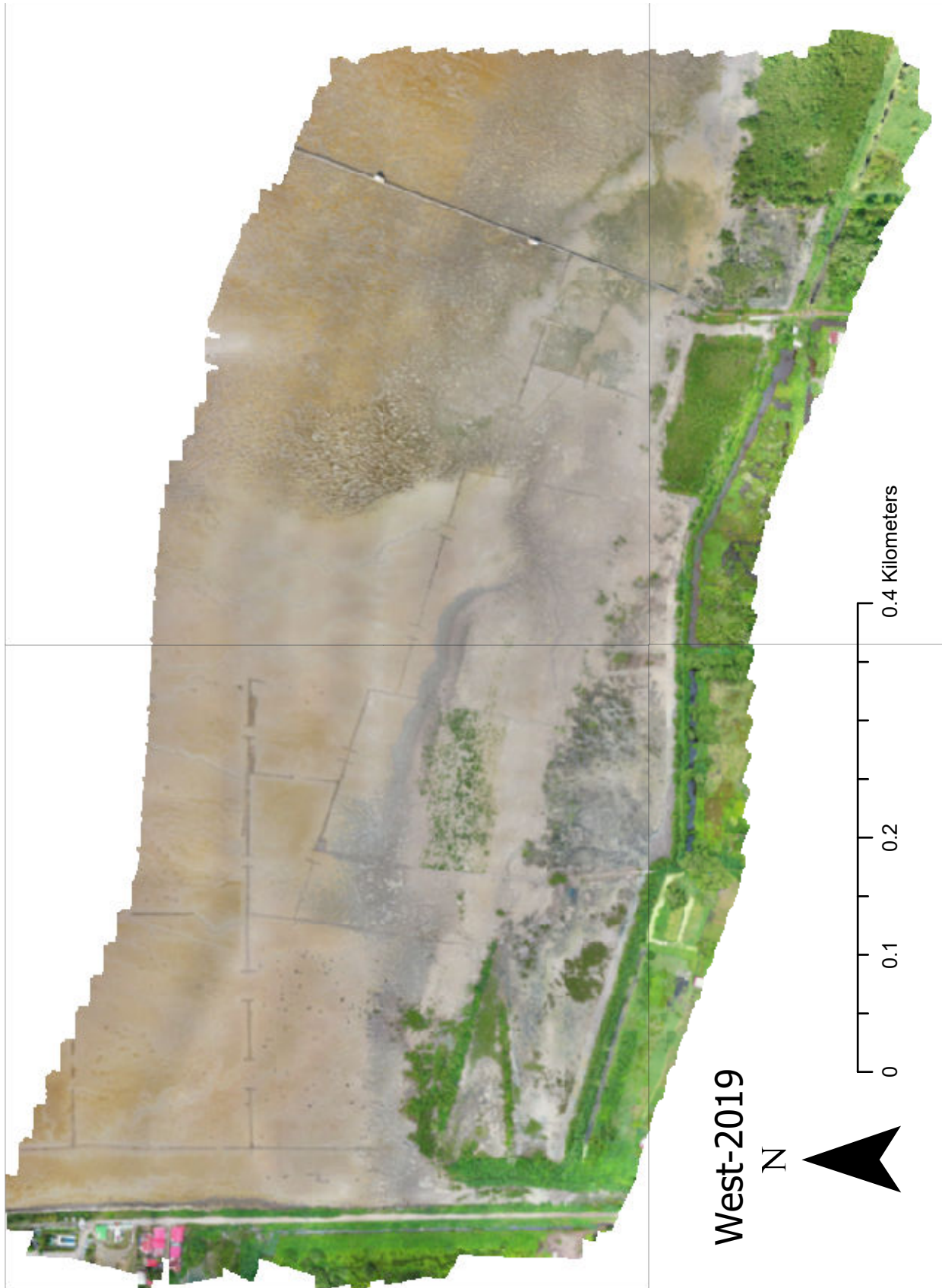
West-2020

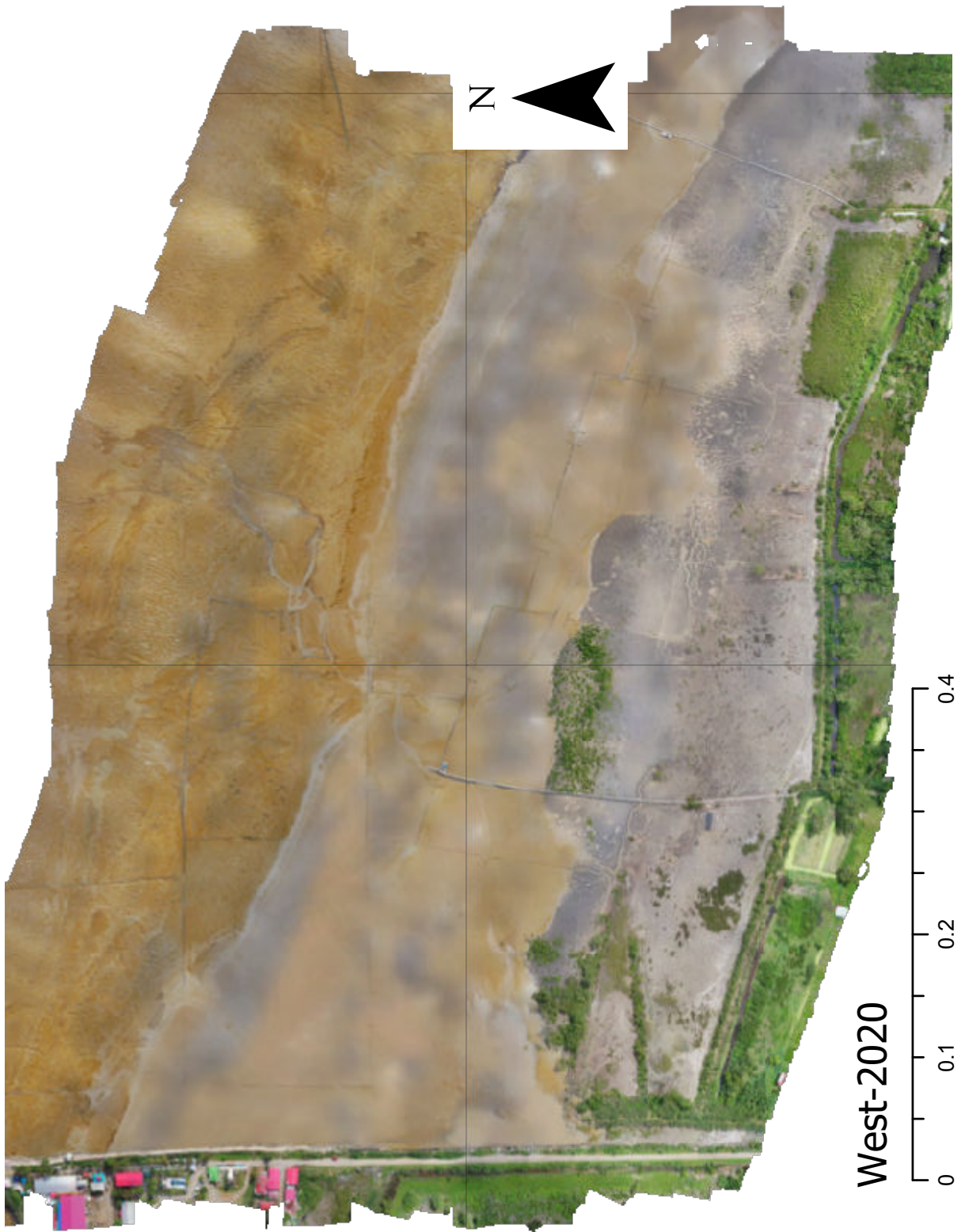
Appendix B - ArcGIS model for transects



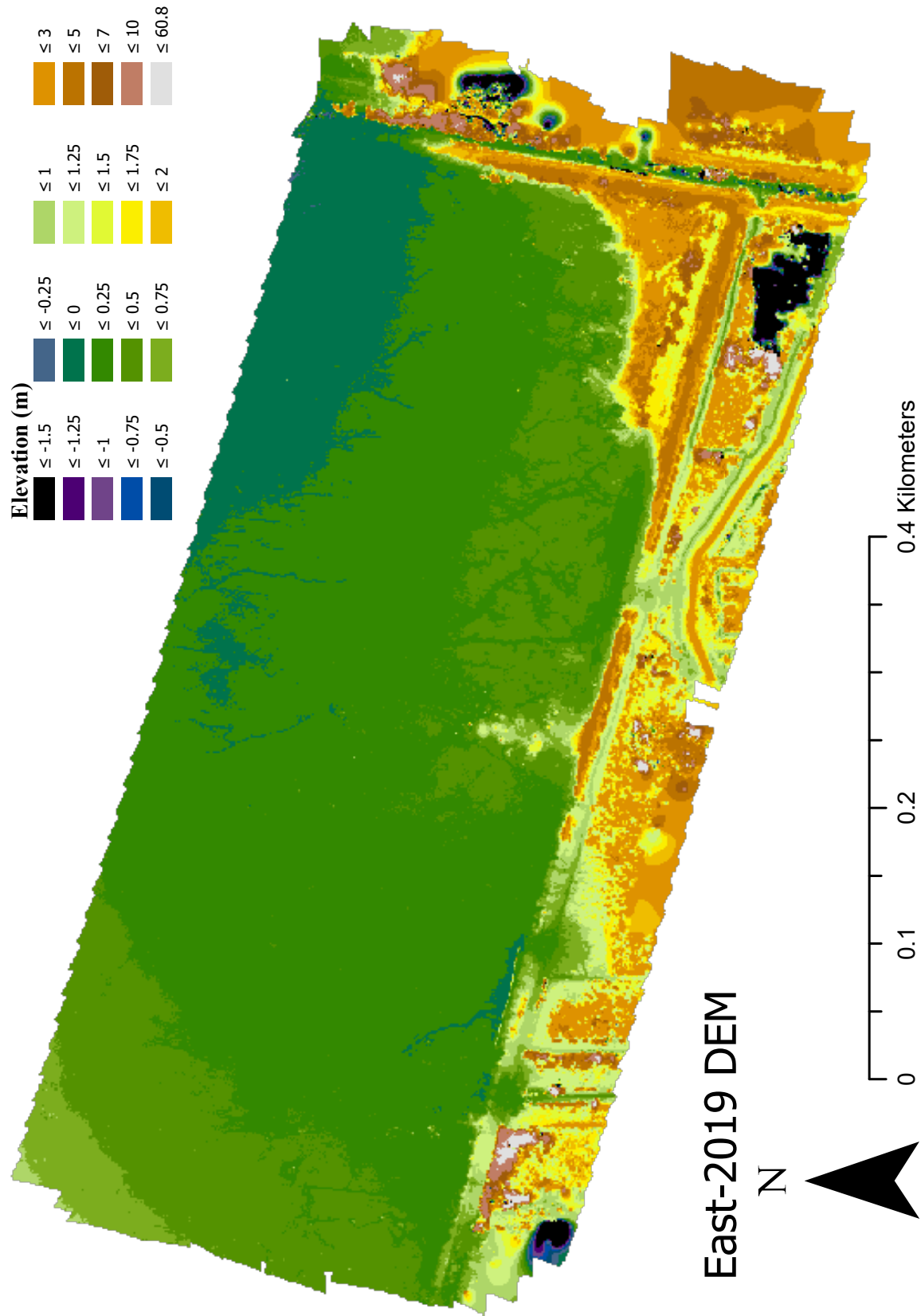
Appendix C - Orthophoto's

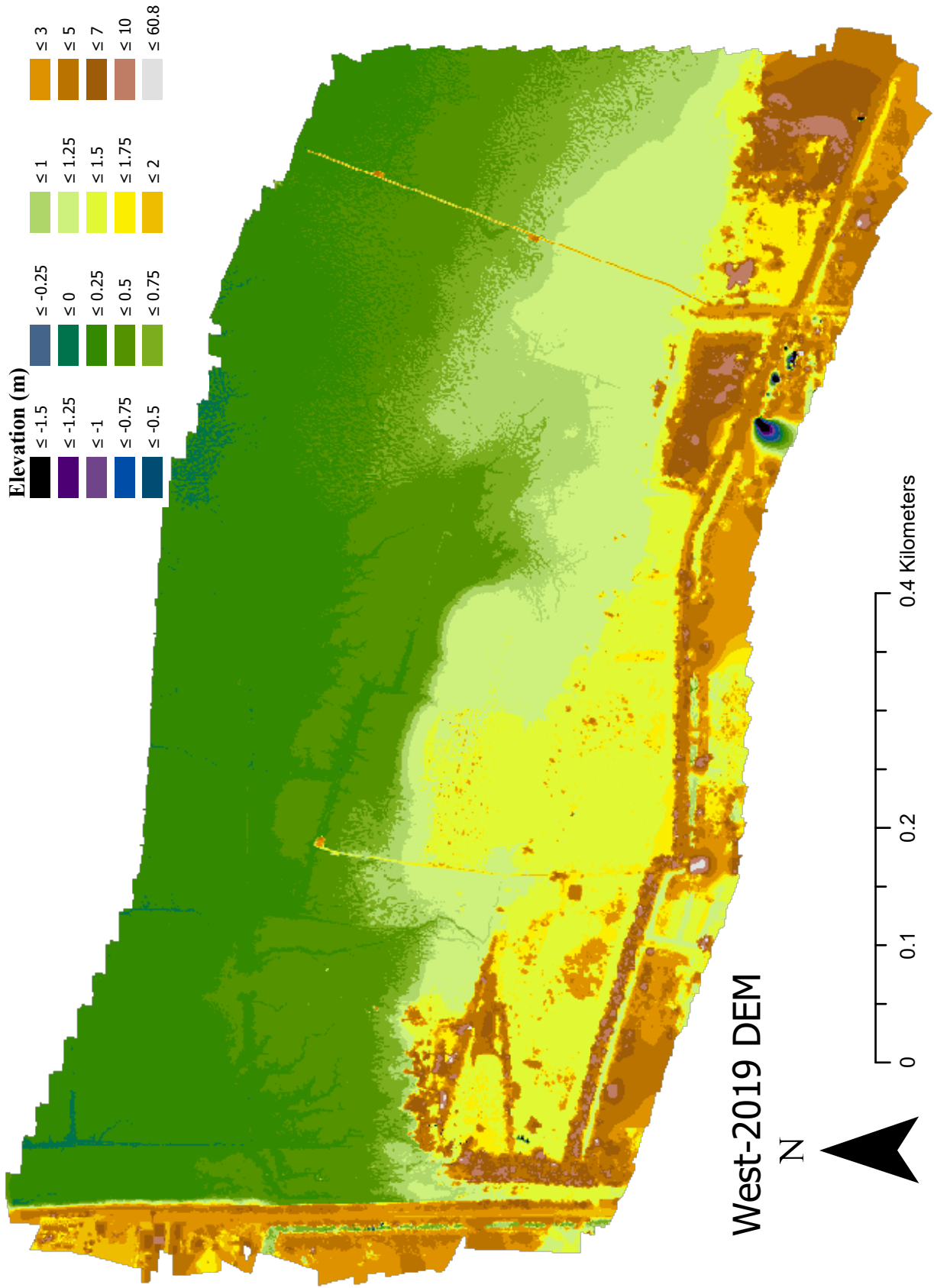


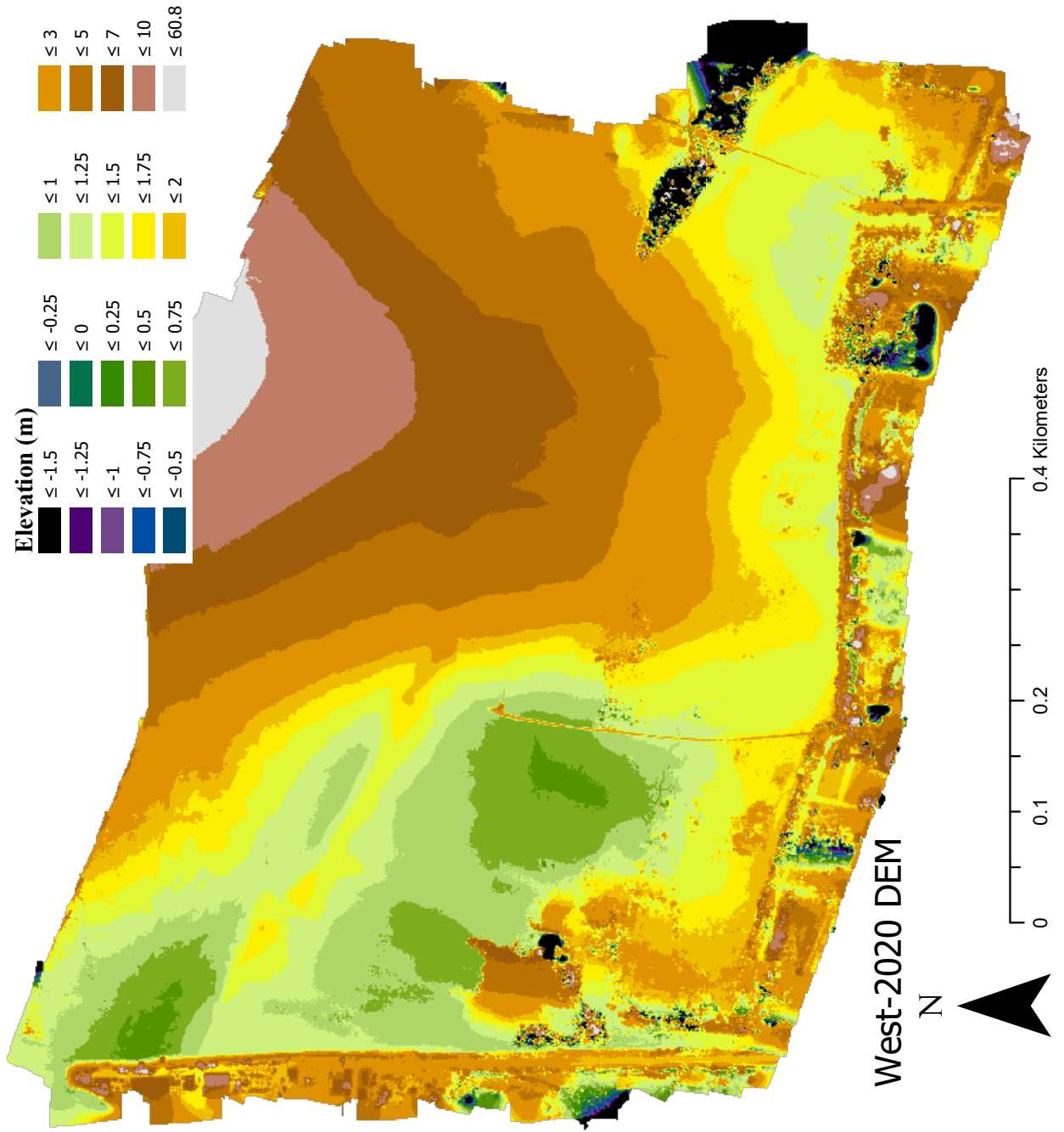




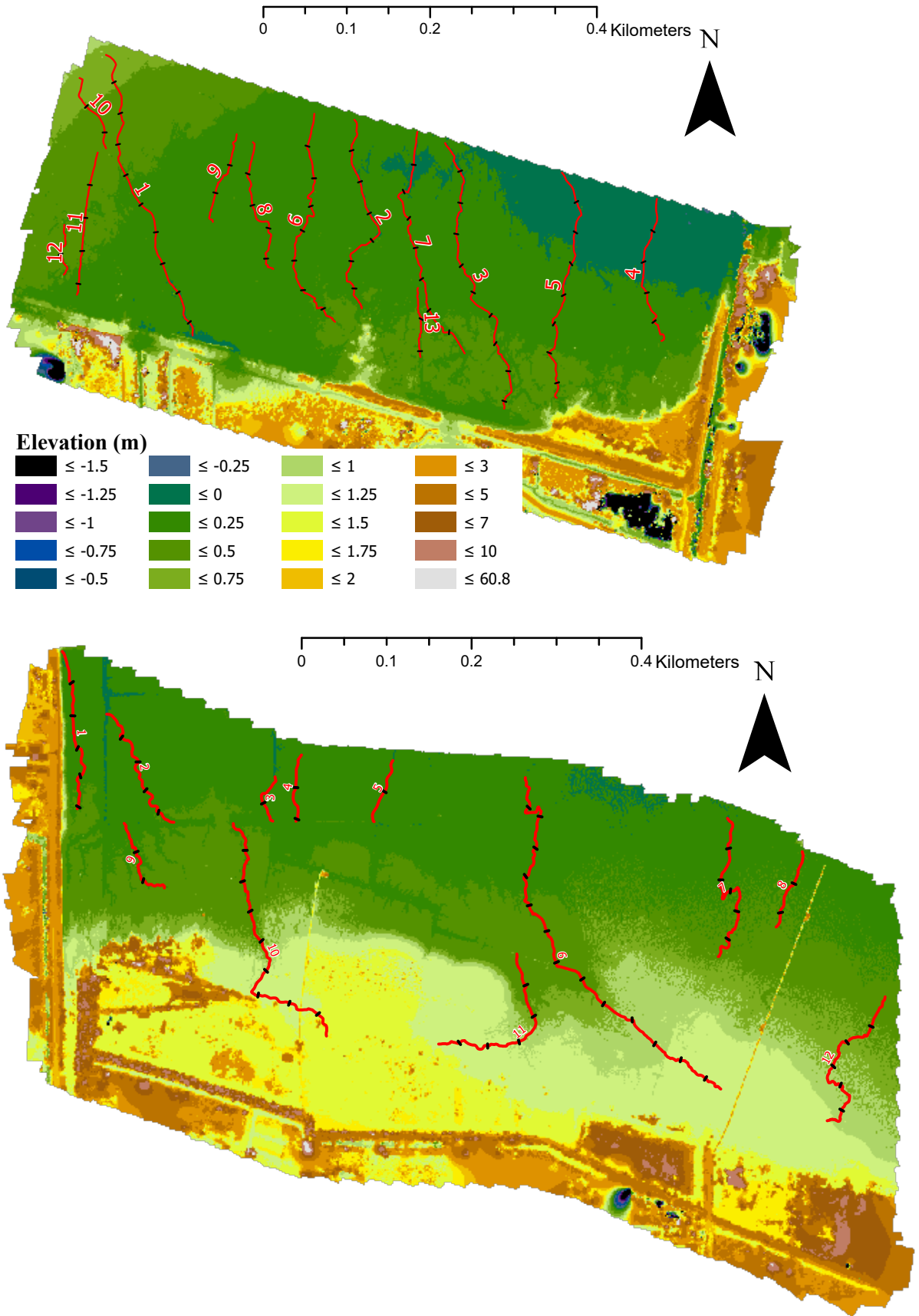
Appendix D - DEM's

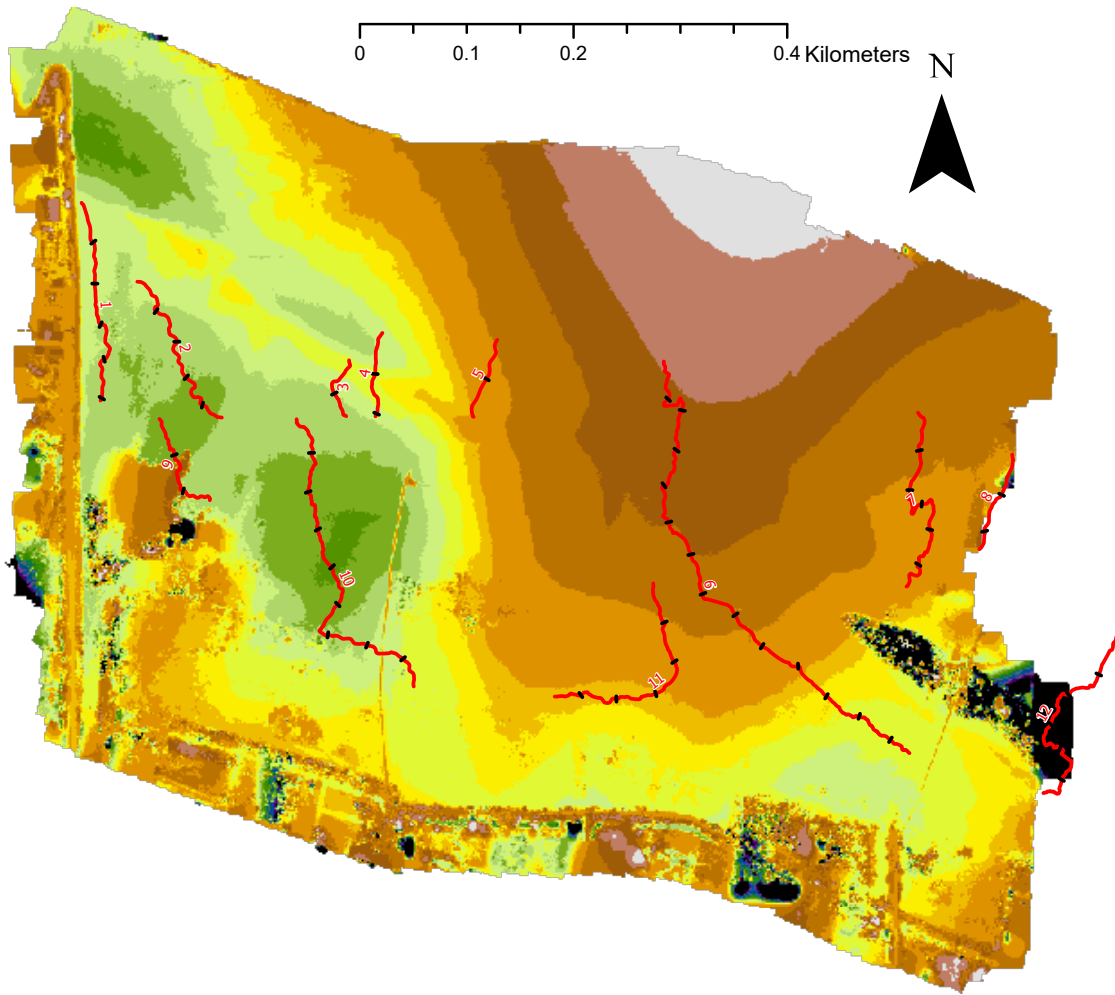




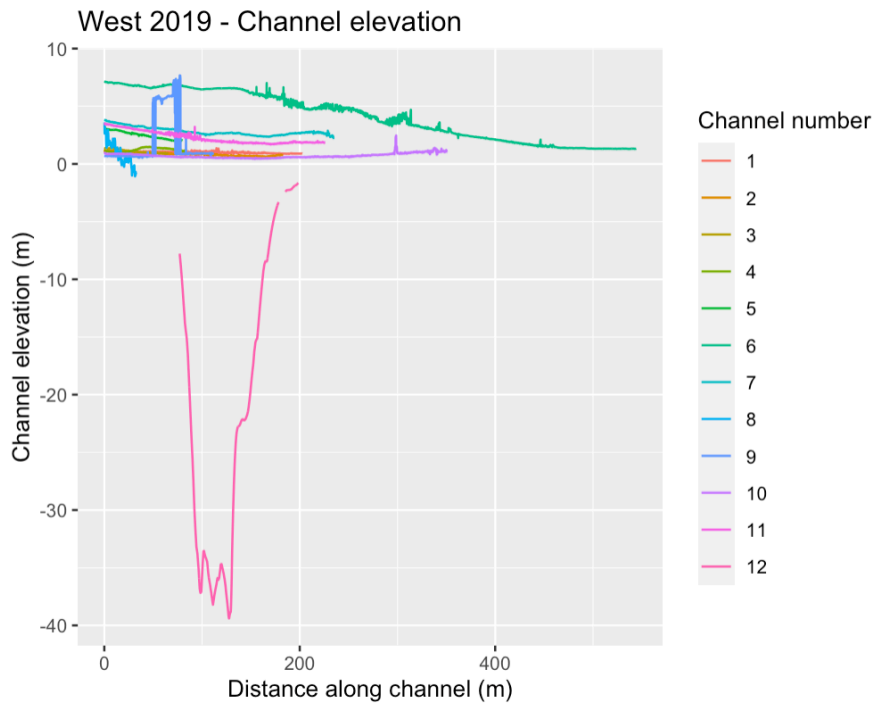


Appendix E - Location of channels on DEM

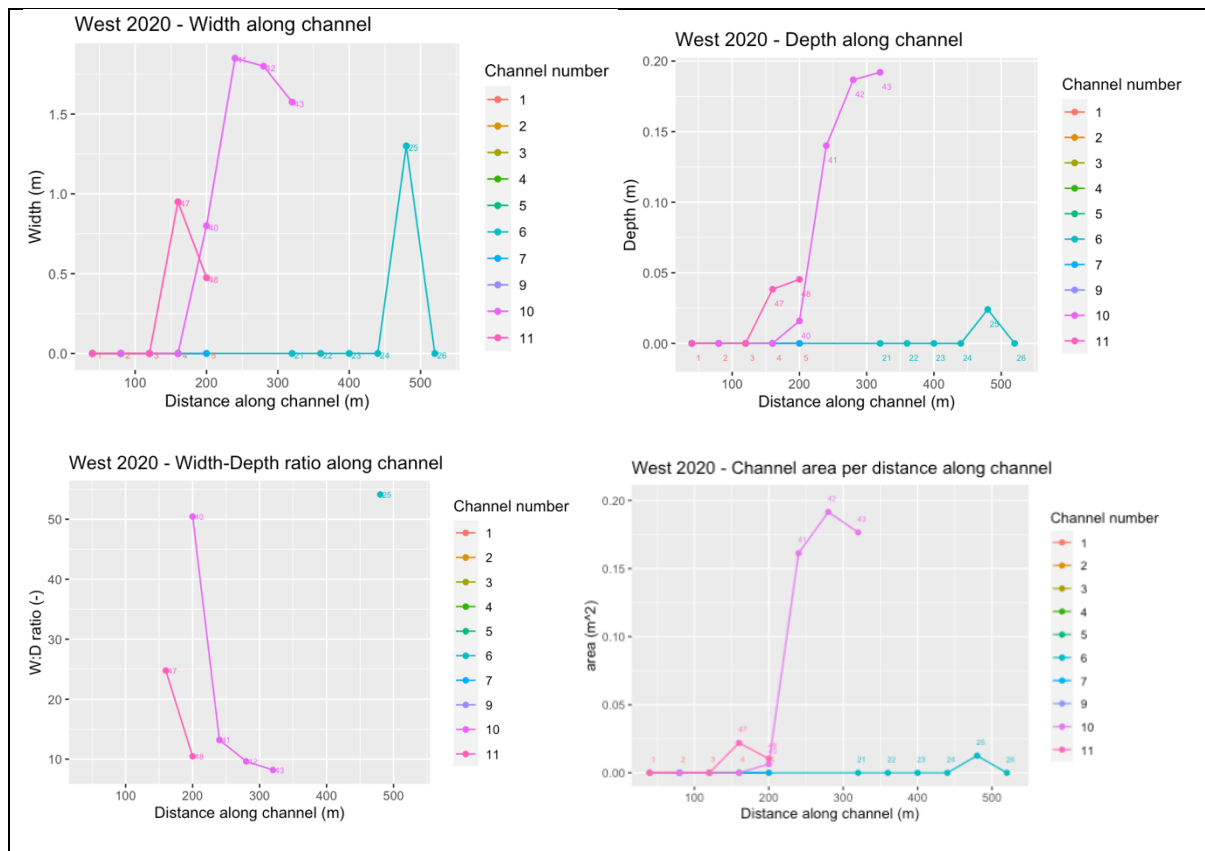




Appendix F - Channel geometry West-2020



Geometry along channel



Geometry over latitude

